

POLITECNICO DI TORINO

Master's Degree in Energy and Nuclear Engineering



**Performance analysis and
optimization of an integral collector
storage (ICS) prototype with PCM**

Dissertation submitted by

Matteo Bilardo

Supervisors: Prof. Enrico Fabrizio^a

Prof. Gilles Fraisse^b

23 JULY 2018

^a Dipartimento Energia (DENERG), Politecnico di Torino

^b Laboratoire Optimisation de la Conception et Ingénierie de l'Environnement (LOCIE), Université Savoie Mont Blanc

To my grandparents †

Declaration

I hereby declare that except where specific reference is made to the work of others, the contents of this dissertation are original and have not been submitted in whole or in part for consideration for any other degree or qualification in this, or any other university. This dissertation is my own work and contains nothing which is the outcome of work done in collaboration with others, except as specified in the text and Acknowledgements. This dissertation contains fewer than 35,500 words including appendices, bibliography, footnotes, tables and equations and has fewer than 100 figures.

Matteo Bilardo

Date

Acknowledgements

This work was carried out during the years 2017-2018 at the Laboratoire Optimisation de la Conception et Ingénierie de l'Environnement (LOCIE), part of the Université Savoie Mont Blanc campus in Bourget-du-Lac and at the Department of Energy (DENERG) of Politecnico di Torino.

I owe my deepest gratitude to my two supervisors Enrico Fabrizio (DENERG) and Gilles Fraisse (LOCIE) for their continuous and meticulous support throughout the work. Without their precious advices, achieving this result would not have been possible. I also want to express my warmest gratitude to all LOCIE professors who guided me and advised me day by day with their rich professional experience in scientific research, and in particular Mickael Pailha, David Cloet and Anne-Cécile Grillet.

I am deeply grateful to all the people with whom I have had the good fortune to cross my university path in the past five years. I would like to thank all the professors who have been the inspiration for my development both as a student and as a person and all the friends and colleagues with whom I shared my educational experiences in Turin, Stockholm and Chambéry.

Ringraziamenti

Questo lavoro è stato svolto durante gli anni 2017-2018 presso il Laboratoire Optimisation de la Conception et Ingénierie de l'Environnement (LOCIE), parte del campus Université Savoie Mont Blanc a Bourget-du-Lac e presso il Dipartimento di Energia (DENERG) del Politecnico di Torino.

Devo la mia più profonda gratitudine ai miei due relatori Enrico Fabrizio (DENERG) e Gilles Fraisse (LOCIE) per il loro continuo e meticoloso supporto durante tutto il lavoro. Senza i loro preziosi consigli, raggiungere questo risultato non sarebbe stato possibile. Voglio anche esprimere la mia più sentita gratitudine a tutti i professori del LOCIE che mi hanno guidato e arricchito ogni giorno con la loro esperienza professionale nella ricerca scientifica, in particolare Mickael Pailha, David Cloet e Anne-Cécile Grillet.

Sono profondamente grato a tutte le persone con cui ho avuto la fortuna di condividere il mio percorso universitario negli ultimi cinque anni. Vorrei ringraziare tutti i professori che sono stati d'ispirazione per la mia crescita sia come studente che come persona e tutti gli amici e colleghi con cui ho condiviso le mie esperienze formative a Torino, Stoccolma e Chambéry.

Abstract

Standard solar systems for DHW production in residential buildings usually consist of a solar collector coupled with a water storage tank. Most of these systems also include auxiliary elements such as circulation pumps, sensors, controllers and safety equipment, giving a sort of complexity to the final installation. Furthermore, maintenance costs as well as space consumption represent some of the main drawbacks of this technology. For these reasons, even though conventional systems are currently well established on the market, “passive” solar systems are slowly gaining attention from both the practical and theoretical point of view, especially for their easy installation, smaller sizes and maintenance-free approach. Against this background, the topic of this thesis is an experimental and numerical study a new concept of integral collector storage (ICS) with heat pipes and phase change material (PCM) storage.

An experimental analysis was carried out in Chambéry, France, studying the energy performances of a prototype that encloses in an aluminium casing a solar absorber, a thermosiphon heat pipes section and a storage cavity filled up with PCM. Solar radiation is transferred from the absorber to the PCM by means of the heat pipes, using methanol as heat transfer fluid. Thanks to a slight inclination, heat pipes act as thermal diode, limiting thermal losses during night-time. PCM storage cavity is made up by a honeycomb structure, improving heat transfer across it. A copper pipe wraps up the storage cavity allowing water flowing inside it and extracting stored heat for the user. A first experimental set was carried out under summer conditions, showing good results in terms of thermal stresses and global functioning. However, consistent thermal losses occur over night, discharging the storage. After a thermographic analysis thermal bridges in the casing were spotted and structural improvements were performed to avoid undesired losses. A new experimental set was then performed in winter conditions, giving better results in terms of productivity and storage efficiency.

Simultaneously with the experimental study, a numerical model was developed, able to simulate the physical behaviour of the prototype. After having validated the model through experimental data, an

annual simulation was performed, giving as result a solar fraction around 56%, comparable with traditional systems.

Overall, the studied ICS represents a DHW source totally in line with other products on the market. However, numerous rooms for improvements are possible, especially regarding the absorber efficiency. Also, further optimization is definitely required by the heat exchanger between the storage cavity and the DHW coil. Possible future scenarios might include several ICSs grouped together in the same system, providing DHW with a real water withdrawal profile.

Keywords: Integral Collector Storage, ICS, Phase Change Material, PCM, Solar Thermal, EES

Résumé

Les systèmes solaires standards pour la production d'eau chaude sanitaire (ECS) comportent habituellement un panneau solaire thermique couplé à un réservoir d'eau. La plupart incluent aussi des éléments auxiliaires tels que des pompes, des capteurs, des contrôleurs, et des équipements de sécurité, ce qui rend ces systèmes relativement complexes. Qui plus est, les coûts de maintenance et l'espace nécessaire sont les principaux inconvénients de cette technologie. Pour ces raisons, bien que les systèmes conventionnels soient bien établis sur le marché, les systèmes solaires "passifs" gagnent progressivement de l'attention, autant sur le plan théorique que pratique, surtout du fait de leur facilité d'installation, de leurs plus petites tailles, et du peu de maintenance nécessaire. Dans ce contexte, le sujet de ce mémoire est l'étude expérimentale et numérique d'un nouveau concept de capteur solaire intégrant le stockage (CSIS), comportant des caloducs et un stockage dans des matériaux à changement de phase (MCP).

Une analyse expérimentale a été réalisée à Chambéry, en France, par l'étude des performances énergétiques d'un prototype comprenant une enveloppe aluminium contenant un capteur solaire thermique, un thermosiphon, et une cavité de stockage remplie de MCP. Les radiations solaires sont transférées du capteur au MCP à l'aide des caloducs, le méthanol étant le fluide caloporteur. Grâce à une faible inclinaison, les caloducs agissent comme une diode thermique, ce qui limite les pertes thermiques pendant la nuit. La cavité de stockage du MCP est en forme de nid d'abeille, ce qui améliore le transfert thermique à travers celle-ci. Le nid d'abeille est entouré d'un tuyau de cuivre où circule l'eau qui extrait pour l'utilisateur la chaleur stockée. Une première série d'expériences a été réalisée pour des conditions estivales, et a donné de bons résultats en termes de contraintes thermiques et de fonctionnement global. Cependant, des pertes thermiques nocturnes constantes dissipent la chaleur stockée. Après une analyse thermographique, des ponts thermiques ont été identifiés

dans l'enveloppe, et des améliorations structurelles ont été mises en place. Une nouvelle série d'expériences a été menée pour des conditions hivernales, et a donné de meilleurs résultats en termes de productivité et d'efficacité de stockage.

Simultanément avec l'étude expérimentale, un modèle numérique a été développé, capable de simuler le comportement physique du prototype. Après avoir validé le modèle avec les données expérimentales, une simulation d'une année de fonctionnement a été lancée, et a abouti à une fraction solaire d'environ 56%, ce qui est comparable aux systèmes traditionnels.

Dans l'ensemble, le CSIS étudié représente une source d'ECS tout à fait comparable aux autres produits sur le marché. Cependant, de nombreuses améliorations peuvent être réalisées, surtout en ce qui concerne l'efficacité du capteur solaire thermique. De même, il ne fait pas de doute qu'une optimisation plus poussée de l'échange de chaleur entre la cavité de stockage et le tour où circule l'ECS gagnerait à être réalisée. Les scénarios futurs pourraient inclure plusieurs CSIS regroupés dans le même système, ce qui donnerait de l'ECS avec un vrai profil de soutirage.

Mots-clés: Capteur Solaire Intégrant le Stockage, CSIS, Matériau à Changement de Phase, MCP, Solaire Thermique, EES

Riassunto

I sistemi solari standard per la produzione di ACS negli edifici residenziali sono solitamente costituiti da un collettore solare accoppiato con un serbatoio di stoccaggio dell'acqua. La maggior parte di questi sistemi include anche elementi ausiliari come pompe di circolazione, sensori, dispositivi di controllo e sicurezza, conferendo una sorta di complessità al sistema finale. Inoltre, i costi di manutenzione ed il consumo ingente di spazio rappresentano alcuni dei principali inconvenienti di queste installazioni tecnologiche. Per questi motivi, anche se i sistemi convenzionali sono attualmente ben consolidati sul mercato, i sistemi solari "passivi" stanno lentamente catturando l'attenzione sia da un punto di vista pratico che teorico, soprattutto per la loro facile installazione, per le dimensioni più ridotte e poiché si basano su un approccio privo di manutenzione.

In questo contesto, l'argomento di questa tesi è uno studio sperimentale e numerico di una nuova idea di collettore con accumulo integrato (ICS) realizzato con tubi di calore e materiale a cambiamento di fase (PCM). Un'analisi sperimentale è stata condotta a Chambéry, in Francia, per studiare le prestazioni energetiche di un prototipo che racchiude all'interno di un singolo involucro di alluminio un assorbitore solare, una sezione di tubi di calore e una cavità di accumulo riempita con PCM. La radiazione solare viene trasferita dall'assorbitore al PCM per mezzo dei tubi di calore, usando metanolo come fluido termovettore. Grazie ad una leggera inclinazione, i tubi di calore agiscono da diodo termico, limitando le perdite termiche durante la notte. La cavità di stoccaggio del PCM è costituita da una struttura a nido d'ape, che migliora il trasferimento di calore all'interno di essa. Una serpentina di rame avvolge la cavità di accumulo e consente all'acqua di scorrere al suo interno per estrarre il calore immagazzinato dal PCM. Una prima fase sperimentale è stata realizzata in condizioni estive, mostrando buoni risultati in termini di stress termici e funzionamento globale del sistema. Tuttavia, perdite di calore non trascurabili si verificano durante la notte, scaricando termicamente l'accumulo. Dopo un'analisi termografica sono stati individuati ponti termici nell'involucro e sono stati apportati miglioramenti strutturali

per evitare perdite indesiderate. Una nuova fase sperimentale è stata quindi eseguita in condizioni invernali, dando migliori risultati in termini di produttività ed efficienza di stoccaggio.

Contemporaneamente allo studio sperimentale è stato sviluppato un modello numerico in grado di simulare il comportamento fisico del prototipo. Dopo aver convalidato il modello attraverso dati sperimentali, è stata eseguita una simulazione annuale, dando come risultato una frazione solare intorno al 56%, paragonabile ai sistemi tradizionali.

Nel complesso, il collettore studiato rappresenta una fonte di ACS totalmente in linea con altri prodotti sul mercato. Tuttavia, esistono ampi margini di miglioramento, in particolare per quanto riguarda l'efficienza dell'assorbitore. Inoltre, è necessaria un'ulteriore ottimizzazione dallo scambiatore di calore tra la cavità di accumulo e la serpentina di acqua calda sanitaria. Possibili scenari futuri potrebbero includere diversi collettori raggruppati nello stesso sistema, studiandone il comportamento con un profilo realistico di prelievo ACS.

Parole chiave: Collettore solare con accumulo integrato, ICS, Materiale a cambiamento di fase, PCM, Solare termico, EES

Contents

Acknowledgements	vii
Ringraziamenti	ix
Abstract	xi
Résumé	xiii
Riassunto	xv
Contents	xvii
List of Figures	xix
List of Tables	xxiii
List of Abbreviations	xxv
1 Introduction	1
1.1 Solar collectors	3
1.2 Solar thermal energy storages	5
1.3 Project presentation and research context	6
1.3.1 Purpose of the project	6
1.3.2 Study phases	7
1.3.3 Project credits	7
1.4 State of the art	7
1.4.1 Research projects	8
1.4.2 The new concept	13
1.5 Performance indicators	14
2 Prototype description	17
2.1 System presentation	17
2.1.1 Principle of operation	18
2.2 Manufacturing	21
2.2.1 Honeycomb storage cavity	21
2.2.2 Heat pipes	23
2.2.3 Domestic hot water (DHW) exchanger	25
2.2.4 Phase change material (PCM)	27
2.3 Possible advanced installations	29
2.4 Bench test	31
2.4.1 Thermocouples	33
2.4.2 Acquisition unit	35
2.4.3 Extra experimental tools	36

3	Early stage performance analysis	37
3.1	Energy evaluation parameters	40
3.2	Charge study	40
3.3	No withdrawal studies	44
3.3.1	Thermal diode effect	45
3.3.2	Heat pipe heat transfer coefficient	46
3.3.3	System efficiency evaluation	48
3.3.4	Power loss study	50
3.4	Withdrawal study	52
4	Prototype thermal improvement and advanced analysis	56
4.1	Prototype thermal improvement	56
4.1.1	Casing improvements	59
4.2	DHW exchanger performances	67
4.3	PCM performance: DSC analysis	71
4.3.1	DSC procedure	71
4.3.2	Data elaboration and analysis	75
4.3.3	Model building	78
4.3.4	Thermographic analysis	79
4.4	Winter performances (February)	83
4.5	Key performance indicators (KPIs)	85
5	Numerical modelling	87
5.1	Components models	87
5.1.1	Solar thermal absorber	89
5.1.2	Heat pipes	92
5.1.3	Insulation layer	94
5.1.4	Plates and cavity	95
5.1.5	PCM modelling	101
5.1.6	DHW heat exchanger	106
5.1.7	Input and boundary conditions	107
5.2	Model validation	108
5.3	Model energy performance	114
5.3.1	Evaluation parameters	115
5.4	Annual performance of the prototype	117
5.4.1	Annual boundary conditions	117
5.4.2	Annual simulation results	118
6	Conclusion	124
6.1	Possible implementations	125
6.2	Future improvements of the ICS	126
	References	128
	Appendix A Thermocouples calibration	130

List of Figures

Figure 1-1. OECD total final consumption trends 1971-2016 (IEA, 2018)	1
Figure 1-2. Solar Water Heating Collectors Global Capacity, 2000-2013 (REN21, 2014)	2
Figure 1-3. 2D schematic of unit studied by (Robinson, et al., 2013)	9
Figure 1-4. Experimental set-up of thermosyphon two-phase solar collector studied by (Esen, et al., 2005)	10
Figure 1-5. Examples of PCM integration into solar thermal systems (Serale, et al., 2015)	11
Figure 1-6. Schematics of the prototype studied by (Serale, et al., 2015)	11
Figure 1-7. ICS-CENG/PCM design (Hailot, et al., 2012)	12
Figure 2-1. Prototype main components	18
Figure 2-2. Heat pipe energy loop	19
Figure 2-3. Principe of operation and main heat fluxes	20
Figure 2-4. Prototype main dimensions (mm)	21
Figure 2-5. Honeycomb cell (detail)	22
Figure 2-6. Honeycomb structure	22
Figure 2-7. HP section (detail)	24
Figure 2-8. Heat pipes and DHW exchanger design	26
Figure 2-9. PCM cavity section with dimensions in m (detail from Figure 2-1)	28
Figure 2-10. Bench test scheme	30
Figure 2-11. ICS implementation for a building	30
Figure 2-12 - Metal supports	32
Figure 2-13. Bench test outside installation during summer period	33
Figure 2-14. Thermocouples sensors scheme	34
Figure 2-15. Thermocouples position in the casing	35
Figure 2-16. Acquisition unit	35
Figure 2-17. Acquisition unit connections	36
Figure 3-1. Experiments timeline graph (Gantt diagram)	39
Figure 3-2. Main temperatures trend in May 2017	41
Figure 3-3. Hourly T_{pi} rise during cavity charging phase	43
Figure 3-4. Main temperatures trends in August 2017	45
Figure 3-5. Evaporator and condenser temperatures highlighting the thermal diode effect	46
Figure 3-6. Heat fluxes in HP evaporator section	47
Figure 3-7. Heat pipe heat transfer coefficient evaluation	48
Figure 3-8. Daily average useful gains versus daily average solar input from 9 a.m. to 5 p.m.	49
Figure 3-9. System efficiency versus loss potential/insolation ratio	50
Figure 3-10. Energy stored and energy lost in August 2017	51
Figure 3-11. Thermal power loss in August 2017	52

Figure 3-12. Main temperature trends in September 2017	53
Figure 3-13. Water withdrawals in September 2017	54
Figure 3-14. Extracted power from water withdrawal	55
Figure 4-1. Laboratory experimental setup with external heater	56
Figure 4-2. T_{pe} and T_{pi} temperature trends during natural cooling	57
Figure 4-3. Exponential fitting for T_{pe} and T_{pi} temperature trends	58
Figure 4-4. Thermal (left) and real (right) picture. Side view	59
Figure 4-5. Thermal (left) and real (right) picture. Bottom view	59
Figure 4-6. Thermal (left) and real (right) picture. Top view	60
Figure 4-7. Metallic support bars on the back of the cavity	60
Figure 4-8. Cavity back plate with thermocouples	61
Figure 4-9. Metallic joints supporting the cavity on its sides	61
Figure 4-10. Old metal bar (top) versus new wooden bar (bottom)	62
Figure 4-11. New wooden joints supporting the cavity sides	62
Figure 4-12. Wooden support parts installation	63
Figure 4-13. Different thermographic comparisons between old support structure (left column) and new wooden structure (right column)	64
Figure 4-14. T_{pe} and T_{pi} temperature trends during natural cooling (improved prototype)	65
Figure 4-15. Exponential fitting for T_{pe} and T_{pi} temperature trends (improved prototype)	66
Figure 4-16. Comparison between old and new cooling trend	67
Figure 4-17. Laboratory charging phase (temperatures trends)	68
Figure 4-18. Stored, available and lost energy during charging process	69
Figure 4-19. Experimental effectiveness, heat transfer coefficient and efficiency for the DHW heat exchanger	70
Figure 4-20. DSC Cell Cross-Section (TA Instruments)	72
Figure 4-21. Heat flow vs. Temperature for a sapphire sample (DSC method)	74
Figure 4-22. Heat flow vs. Temperature for a PEG 6000 sample (DSC method)	74
Figure 4-23. Sapphire specific heat by (Ditmars, et al., 1982)	76
Figure 4-24. Experimental PEG 6000 specific heat for melting (red) and crystallization (blue) process	76
Figure 4-25. Experimental PEG 6000 specific enthalpy for melting (red) and crystallization (blue) process	78
Figure 4-26. Experimental PEG 6000 specific heat fitting from literature	79
Figure 4-27. PEG 6000 microscopic view ($T = 30.5 \text{ }^\circ\text{C}$). Solid phase	80
Figure 4-28. PEG 6000 microscopic view ($T = 62 \text{ }^\circ\text{C}$). Melting phase	81
Figure 4-29. PEG 6000 microscopic view ($T = 65 \text{ }^\circ\text{C}$). Liquid phase	81
Figure 4-30. PEG 6000 microscopic view ($T = 43 \text{ }^\circ\text{C}$). Crystallization phase	82
Figure 4-31. PEG 6000 microscopic view ($T = 42 \text{ }^\circ\text{C}$). Solid phase	82
Figure 4-32. Main temperatures trends (February)	83

Figure 4-33. Water withdrawal temperatures detail during February 2018	84
Figure 4-34. Extracted power from water withdrawal in February 2018	85
Figure 5-1. ICS 3D view with main components	88
Figure 5-2. ICS model scheme with sections and temperature nodes (black dots)	89
Figure 5-3. Solar fluxes on the collector	91
Figure 5-4. Collector electrical scheme	91
Figure 5-5. Heat pipes section: 2D scheme	93
Figure 5-6. Metal bars holding the cavity: not modelled	94
Figure 5-7. PCM cavity mash	95
Figure 5-8. Electrical analogy of T_{pe} and T_{pi} nodes	97
Figure 5-9. Radii, surfaces, volumes and main thermal resistances adopted in the cavity model	99
Figure 5-10. Cavity: electrical analogy model	100
Figure 5-11. Temperature nodes (red dots) corresponding to the energy balances in Table 5-7	101
Figure 5-12. Interrupted heating: assumption implemented in the model	104
Figure 5-13. Interrupted cooling: assumption implemented in the model	105
Figure 5-14. Hydraulic scheme with 3-way mixing valve	107
Figure 5-15. Absorber (T_{abs}) and inferior cavity plate (T_{pi}) temperature simulation in August 2017	109
Figure 5-16. Cavity temperature simulation (T_{pi}): sub-cooling detail	110
Figure 5-17. Absorber (T_{abs}) and cavity (T_{pi}) temperature during water withdrawal	111
Figure 5-18. Water temperature at the outlet	112
Figure 5-19. Absorber (T_{abs}) and inferior cavity plate (T_{pi}) temperature simulation in February 2018	113
Figure 5-20. Water withdrawal simulation detail during February 2018	114
Figure 5-21. Daily water withdrawal for the annual simulation	118
Figure 5-22. Yearly energy production	119
Figure 5-23. Monthly energy values	120
Figure 5-24. Solar fraction	120
Figure 5-25. Stored fraction	121
Figure 5-26. <i>Tpe</i> trend on June 4 th (model simulation)	122
Figure 5-27. <i>Tpe</i> trend on January 13 th (model simulation)	123

List of Tables

Table 1-1. Types of solar collectors (Kalogirou, 2006)	4
Table 2-1 - PEG 6000 specifications	27
Table 2-2. Thermocouples installed	34
Table 4-1. Microscopic analysis	80
Table 4-2. KPIs values for ICS prototype (IEA, 2018)	86
Table 5-1. Glass, air and absorber properties	90
Table 5-2. Temperature nodes balances (part 1)	92
Table 5-3. Heat pipe properties	94
Table 5-4. Insulation properties	94
Table 5-5. Cavity plate, metal fins and honeycomb structure properties	96
Table 5-6. Temperature node balances (part 2)	97
Table 5-7. Temperature node balances (part 3)	100
Table 5-8. PCM properties	101
Table 5-9. DHW pipeline and water properties	107
Table 5-10. Cold water monthly temperatures from the network	115
Table 5-11. Climatic annual input data	117

List of Abbreviations

IEA	I nternational E nergy A gency
OECD	O rganisation for E conomic C o-operation and D evelopment
HTF	H eat T ransfer F luid
PCM	P hase C hange M aterial
ICS	I ntegral C ollector S torage
HVAC	H eating V entilation A ir C onditioning
CENG	C ompressed E xpanded N atural G raphite
DHW	D omestic H ot W ater
KPI	K ey P erformance I ndicators
HP	H eat P ipe
PEG	P olyethylene G lycol
DSC	D ifferential S canning C alorimetry
EES	E ngineering E quation S olver
ADEME	A gence de l' E nvironnement et de la M aitrise de l' E nergie
LOCIE	L aboratoire O ptimisation de la C onception et I ngénierie de l' E nvironnement

Chapter 1

1 Introduction

The increase in CO₂ in the atmosphere, global warming and the consequent melting of the glaciers are major problems with which the human population will have to relate in the coming years. Many efforts have already been made, especially in the field of energy efficiency and rational use of resources. However, the world population is constantly increasing, and will most probably reach 11.2 billion in 2100 (United Nations, Department of Economics and Social Affairs, Population Division, 2017). Together with it, global energy consumption will tend to increase, affecting all sectors, from transport, to heating and cooling and water consumption. In this future perspective, the rational use of energy resources will be one of the fundamental elements for the development of future generations. In addition to the use of energy, even the production of it will have to be able to maximize the renewable potential by putting aside the fossil resources, destined to become extinct.

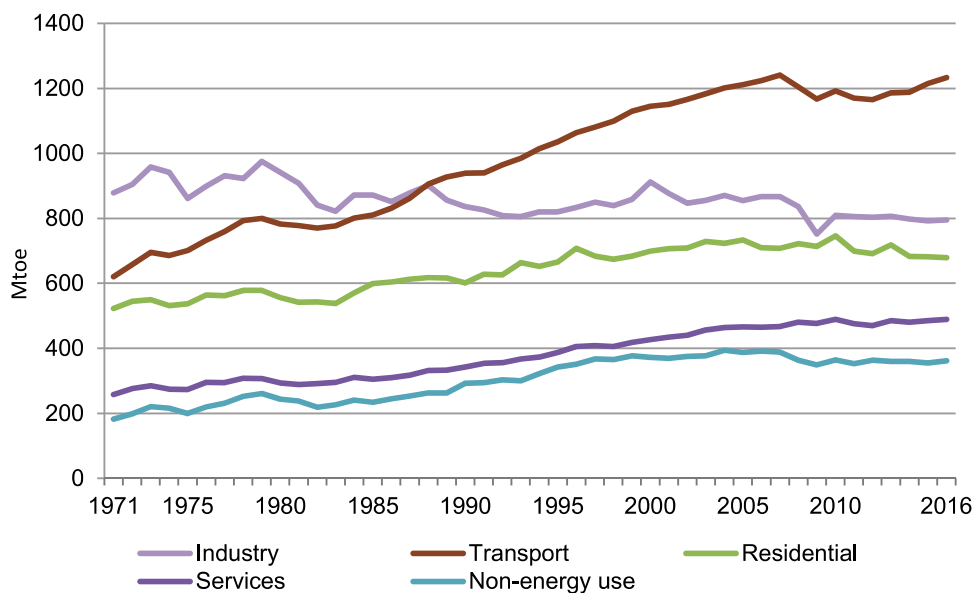


Figure 1-1. OECD total final consumption trends 1971-2016 (IEA, 2018)

Among the renewable resources that our planet offers, solar energy is certainly the one we can receive in the simplest way possible and in a preponderant quantity compared to different renewable resources. The sun is in fact able to invest the globe with a power of about 174 PW before entering the atmosphere (Tian, et al., 2013). Considering the energy balance of energy from the sun, only 51% of the previous data actually reaches the Earth's surface and the oceans of the planet (Smil, 1991). Even though these mitigations affect the usable energy, the solar power made available is a huge resource, which alone

would be able to meet the global energy needs. For this reason, it must be collected in the most efficient way possible and at the same time stored in order to be used at a later time.

Another advantage of solar energy is its presence in a rather uniform distribution on the terrestrial globe. In fact, even if it depends on the latitude of the planet, it can be exploited in most industrialized countries, benefiting also a large part of the developing countries, most of which are located at very favourable latitudes to exploit solar potential.

The solar resource can both be intensively exploited, through large production plants, and at the domestic level, through installations aimed to be used by small group of people. This feature allows solar energy to acquire added value, i.e. to be used both on the large and small scale. This argument applies to both the main types of use of solar power: photovoltaic and solar thermal. Considering solar thermal power, that represents the topic on which the study carried out in this work will be focused, it has grown steadily since 2000, when the total installed power did not reach 50GW, up to the 326 GW installed in 2013 (REN21, 2014).

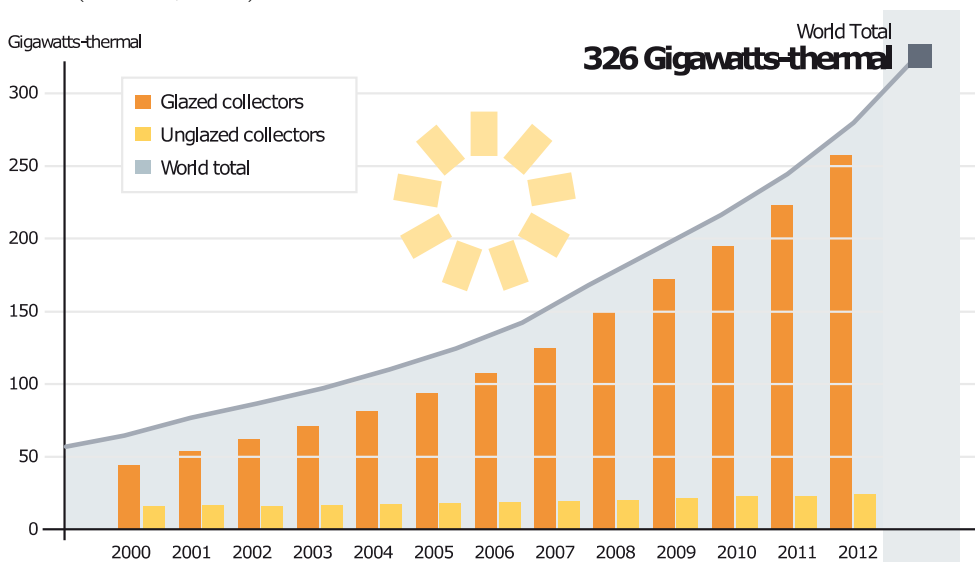


Figure 1-2. Solar Water Heating Collectors Global Capacity, 2000-2013 (REN21, 2014)

The use of solar energy for thermal purposes, which cover both domestic hot water production and space heating, was one of the first methods of integrating renewable sources alongside traditional energy systems. Most of the national European regulations expect that a percentage of the energy needs of buildings is produced from renewable sources. The technologies of solar thermal production are now widespread in the most varied applications, both industrial and residential and are an integral part in almost all new buildings' energy systems.

As a constantly evolving sector, applications in the field of solar thermal energy are constantly being studied and researched. The purpose of this work is precisely to investigate the energy performances of a new innovative solar

collector, able to enclose in a single casing both the solar energy capture elements and the energy storage section. However, before entering into the specifics of this work, some clarifications regarding the elements that make up a solar thermal collector and a brief description of the current solutions on the market are necessary.

1.1 Solar collectors

In a solar thermal system, the collector is the element capable of collecting solar radiation and transforming it into useful thermal energy. The energy collected by the collector is then transported by a heat carrier fluid, which has the task of moving the energy to other parts of the system. The absorbed heat can be directly used by a user with immediate access to the source, or it can be stored in a thermal storage and then used at a later time.

The fundamental quantity that distinguishes a collector is its absorbing surface, or the effective area that is hit by solar radiation. Depending on how the absorbent surface is designed, we can divide the solar collectors into two broad categories:

- Non-concentrating collectors
- Concentrating collectors

For the former, the solar interception area is equal to the absorbing area. For the latter, however, the solar radiation is concentrated towards a smaller area. The parameter that distinguishes these types of applications is the geometric concentration ratio, defined as the open area of the collector (A_a) divided by the surface area of the receiver (A_r). Concentrating collectors are able to reach higher temperatures, increasing the efficiency of a subsequent thermal cycle. Their application is widespread in large solar power plants, which are intended to produce both electricity and heat. On the other hand, non-concentrating collectors are more widespread in small-scale systems or where the user does not require high temperatures of the heat-transfer fluid (De Winter, 1991).

Table 1-1 summarizes the main types of solar collectors, associated with their working temperature range. A more in-depth review of the individual categories is contained in (Tian, et al., 2013).

Table 1-1. Types of solar collectors (Kalogirou, 2006)

<i>Motion</i>	<i>Collector type</i>	<i>Absorber type</i>	<i>Concentration ratio</i>	<i>Temperature range [°C]</i>	
<i>Non-concentrating</i>	<i>Stationary</i>	Flat plate collector (FPC)	Flat	1	30-80
		Evacuated tube collector (ETC)	Flat	1	50-200
		Compound parabolic collector (CPC)	Tubular	1-5	60-240
<i>Concentrating</i>	<i>Single-axis tracking</i>	Compound parabolic collector (CPC)	Tubular	5-15	60-300
		Linear Fresnel reflector (LFR)	Tubular	10-40	60-250
		Parabolic trough collector (PTC)	Tubular	15-45	60-300
		Cylindrical trough collector (CTC)	Tubular	10-50	60-300
	<i>Two-axes tracking</i>	Parabolic dish reflector (PDR)	Point	100-1000	100-500
	Heliostat field collector (HFC)	Point	100-1500	150-2000	

1.2 Solar thermal energy storages

After solar energy has been collected from the collector and transferred to the heat transfer fluid (HTF), it must be efficiently stored for later use. The thermal storage systems related to solar thermal energy are of primary importance, since solar activity is not continuous over time but follows the alternation of day and night. To ensure energy continuity, different storage systems can be associated with a solar collector. A series of aspects must be considered when designing the type of thermal storage to be installed (Tian, et al., 2013). The main parameter to be considered is certainly the specific thermal capacity of the material, which determines the amount of heat that the material is able to accumulate. High energy density is also important to ensure a small storage volume with a consequent limited impact on the environment. Secondly, also the thermal exchange performances of the material must be as high as possible, in order to maximize the heat exchange rate between the storage and the HTF. Thirdly, mechanical and chemical stability must be tested, in order to avoid degradation of the material, especially when it is subjected to numerous discharge and thermal loading cycles. Finally, all these technical criteria are flanked by environmental and economic ones, which must be considered to ensure the use of a material that is sustainable and not harmful to the environment, and that can also be commercialized at the economic level.

Possible accumulation systems can be grouped into three main categories, which depend on the mechanism by which the energy is stored (Tian, et al., 2013):

- Sensitive heat storage materials
This type of material is the most widespread in the various applications and exploits the sensible heat through the rise or drop of the material temperature, which can be in solid or liquid phase. The advantage of this solution is a relatively low cost, to the detriment of the thermal capacity, which is usually lower than the other types adopted. Water, which is one of the most used storage means, falls into this category.
- Latent heat storage materials
This category includes the phase change materials (PCM), able to exploit phase transitions, solid to liquid or liquid to gas, in order to increase the capacity of thermal storage. PCM storages have a higher energy density, since large amounts of energy are involved in the passage of state. Furthermore, their advantage is that they can accumulate/provide energy in a smaller thermal rise/drop, exploiting the isothermal phase change mechanism. The weak point of this category is usually the low thermal conductivity, which therefore requires high efficiency heat exchange systems.
- Chemical heat storage materials
The latter category exploits the energy contained in chemical bonds as a form of storage. The heat absorbed by the collector is used to carry out reversible chemical transformations capable of releasing energy at a later

time. This type of storage is able to deal with large quantities of heat and represents the solution with the highest potential from the thermal point of view. However, large-scale commercial solutions are not yet available on the market, due to the restrictions to be met, which involve the use of specific chemical reactors and long-term chemical stability.

1.3 Project presentation and research context

The object of the study contained in this document is a new concept of an integrated collector storage (ICS). The peculiarity of this study is to combine within a single prototype a classic flat-plate collector with a storage system integrated in the same casing. Moreover, as regards the storage section, a cavity containing phase change material (PCM) has been designed. Among various possibilities, the polyethylene glycol 6000 (PEG 6000) has been chosen. What makes this case study even more unique is the mechanism by which the absorber section and the storage cavity have been put into communication: between them six heat pipes filled with methanol have been designed, used as heat transfer fluid with the task of removing the heat absorbed by the collector and transferring it towards the accumulation section, positioned on the back. The heat pipes, designed to work with natural convection due to gravity, have been installed with a slight inclination (5°). All the elements just described have subsequently been isolated and enclosed within a single casing.

After a preliminary phase of theoretical studies, the single functional elements just described were produced and assembled to create a first operating prototype. All the experimental studies, which will be presented later, will refer to this prototype.

1.3.1 Purpose of the project

The purpose of this project was to investigate an innovative system for the production of domestic hot water. The studied prototype is designed for a typical domestic user, given the rather small dimensions. However, this does not exclude possible implementations aimed at different types of users. The objective of the following study is to validate the functioning and competitiveness of the prototype with respect to traditional solutions. The basic idea is to propose an innovative system with the following advantages over most of the systems available on the market:

- Easy installation
The prototype presents itself as an integrated system that does not need auxiliaries, enclosing inside it the storage section, usually detached from the absorber section in traditional systems. Being completely insulated from the external environment, the whole system is designed to be installed outdoors, without requiring special structural alteration.
- Passive functioning

An advantage of the proposed system is that of being able to operate in a “passive” way, reducing maintenance operations to a minimum. The system is designed to be able to work autonomously without manual control operations, providing, when requested by the user, a source of renewable hot water that can operate either alone or integrated with a traditional system.

- Energy efficiency
What we expect from this study is to obtain results that can confirm efficiency from an energy point of view, especially for installations aimed at harsh climates.

1.3.2 Study phases

The study process, which starts from the design of the prototype to the study of its properties, can be divided into 4 main phases:

- 1) Design of the prototype and its various sections. Consequent assembly and preparation of a test bench equipped with sensors useful for monitoring the system.
- 2) Commissioning of the test bench, experimental tests for system charging and discharging cycles and subsequent analysis of the data.
- 3) Structural and functional improvements to the prototype, based on what emerged from phase 2.
- 4) Development of a numerical model and validation of it through experimental data.

1.3.3 Project credits

The prototype construction project was led by ADEME (Agence de l'Environnement et de la Maîtrise de l'Énergie), in collaboration with several companies including S.M.C.I. (Sainte Marie Constructions Isothermes) for the materials supply, DATE for graphic design of the prototype and INSULA FRANCE.

The experimental study and data analysis phase was instead entrusted to the Université Savoie Mont Blanc, in particular to the LOCIE research group (Laboratoire optimisation de la conception et ingénierie de l'environnement). The prototype was installed and studied at INES (Institut national de l'énergie solaire) based in Le Bourget-du-Lac, France.

1.4 State of the art

The continuous updates of European regulations, which are reflected in the individual member states, require a constantly increasing percentage of renewable energy needs. For this reason, the solar thermal market is constantly evolving, following what experimental research offers. Both the French and Italian governments (D.Lgs. 28/2011) require that the percentage of domestic hot water

needs be 50% covered by renewable sources. The growing prospects in this sector are therefore advantageous and the proposal for new high-efficiency systems is increasingly encouraging.

The current solar thermal systems are composed of an absorber, a storage tank (usually located inside the building) and a series of auxiliary components that ensure correct and safe operation (circulation pumps, expansion tanks, systems control and regulation, etc.). This makes the current systems complicated, in need of continuous maintenance and space-consuming. Research in this field is aimed at solving these main problems in order to provide end users with more efficient, reliable and less expensive systems.

In this context the so-called Integral Collector Storages (ICS) represent a possible solution. The advantages of this category of solar collectors, already analysed in the previous paragraphs, allow to solve most of the problems related to traditional systems. In recent decades, ICS have received many attentions from researchers and several projects have been objects of study, each offering different technical solutions. A careful review of the fundamental principles underlying the functioning of ICS was conducted by (Smyth, et al., 2006). However, the last few years have seen further progress in the experimental field.

In the following paragraphs some experiments concerning ICS systems will be considered, which have been taken into account for the realization of the studied prototype.

1.4.1 Research projects

The use of heat pipes and phase change materials as integral elements of a solar collector is not entirely new. In the past few decades several experimental studies have been conducted all over the world trying to implement these technologies in the field of solar thermal.

Already in 2001 a study conducted by (Susheela, et al., 2001) demonstrated the effectiveness of the use of heat pipes integrated into the walls of a building, connecting an absorber surface installed on the external wall facing south with a water storage tank (Figure 1-3).

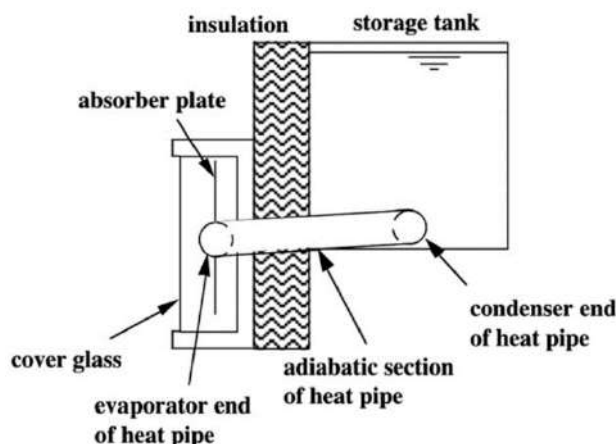


Figure 1-3. 2D schematic of unit studied by (Robinson, et al., 2013)

The solar heat, removed from the heat pipes, is transferred to the water storage, positioned in an internal environment. Through a natural convection exchange mechanism, the storage tank is free to release heat to the internal environment, shifting the peak of solar energy. This solution belongs to passive heating systems and sees the implementation of heat pipes that perform the function of “thermal diodes”, allowing the heat to flow only in one direction, thanks to the slight inclination upwards.

The same system was subsequently verified by (Robinson, et al., 2013), which demonstrated an average daily thermal efficiency of 61.4% during an entire heating season. The same author has also identified the possible drawbacks that such a system can cause. The effect of thermal diode played by heat pipes, although generating a positive effect in terms of thermal gains during the winter period, causes a sharp increase in cooling loads during the summer, negatively affecting the HVAC plant.

To counteract this negative effect, (Robinson, et al., 2015) has experimented with several possible solutions, testing both design modifications and control strategies and achieving the desired results to limit the cooling loads due to the heat pipe walls. However, the use of heat pipes in solar systems remains an advantageous method with great potential from an energy point of view. Furthermore, several energy evaluation parameters defined by Robinson have been subsequently applied to this study, having the two systems studied particular similarities.

Another study concerning heat pipes application, conducted by (Esen, et al., 2005), has tested the thermal performance of a two-phase thermosyphon solar collector. The aforementioned collector takes advantage of the use of heat pipes to transport solar energy to a water storage tank located in the upper part of the system (Figure 1-4).

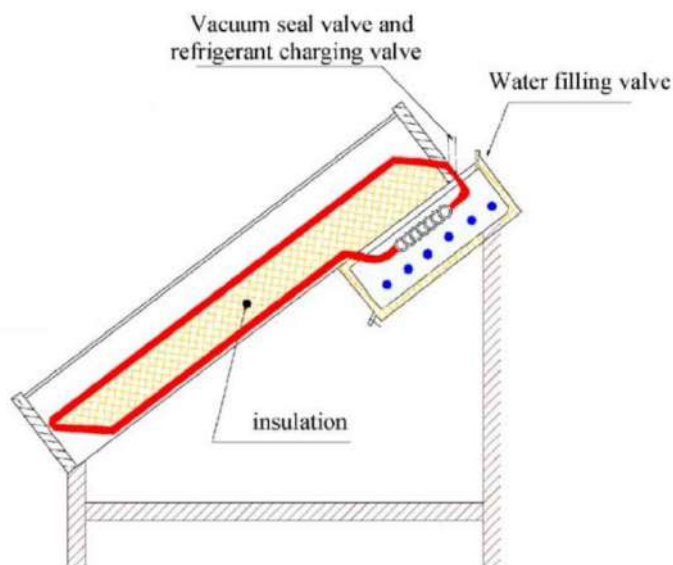


Figure 1-4. Experimental set-up of thermosyphon two-phase solar collector studied by (Esen, et al., 2005)

Also, in this experiment the heat pipes work thanks to the effect of gravity with the condenser installed in a higher position with respect to the evaporator. This solution generates a two-phase thermosiphon system that does not require the intervention of auxiliary elements. In particular, Esen has studied how different refrigerant fluids used as heat transfer fluids inside the heat pipes affect the heat capacity of the collector. The results produced, in addition to providing some guidelines in the selection of a specific fluid for the heat pipe, have again demonstrated the reliability of an integrated storage system obtaining efficiencies comparable with other solutions on the market.

Putting aside the use of heat pipes in solar thermal systems, another technological feature that has recently gained the upper hand in solar thermal installations needs some considerations, namely, the adoption of phase change materials (PCM). The use of PCMs is becoming increasingly common in energy applications related to solar energy, mainly for two reasons. Firstly, a PCM, exploiting the latent heat of phase change, is able to accumulate large amounts of energy without involving high temperature rises. Secondly, PCMs have a higher energy density than traditional materials, thus leading to savings in terms of volume occupied. A valid review of the state of the art regarding the applications of PCMs in solar thermal is provided by (Sadhishkumar, et al., 2014). In this review, several possible implementations of PCMs are underlined. (Vikram, et al., 2006) demonstrate how PCMs are reliable to make solar thermal energy available at night and (Anant, et al., 2009) indicate how they can be involved in systems that include a traditional water storage section, concluding that latent heat storage is a commercially viable option.

The various application possibilities of PCMs have been summarized by (Kousksou, et al., 2011), which indicates three main scenarios involving PCMs within a solar thermal system

- Integrated PCM inside a storage tank that separates a primary circuit (solar loop) from a secondary (user loop) (Figure 1-5a);
- PCM included in the primary circuit as an additional storage system (Figure 1-5b);
- Integrated PCM inside the collector (ICS with PCM) (Figure 1-5c).

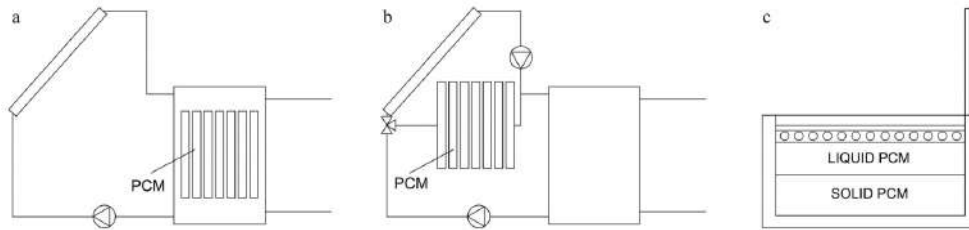


Figure 1-5. Examples of PCM integration into solar thermal systems (Serale, et al., 2015)

A further technical solution has been realized and studied by (Serale, et al., 2015), proposing a system composed of an open primary loop where microencapsulated phase change slurry (mPCS) has been adopted. The solution, that is a mixture of microencapsulated phase change material, water and surfactants, was used as heat transfer fluid (HTF). The open primary loop also integrates the storage tank. In this particular experiment, the HTF matches with the energy storage material. A closed secondary loop was in charge of extracting heat from the storage section to distribute it towards a possible user.

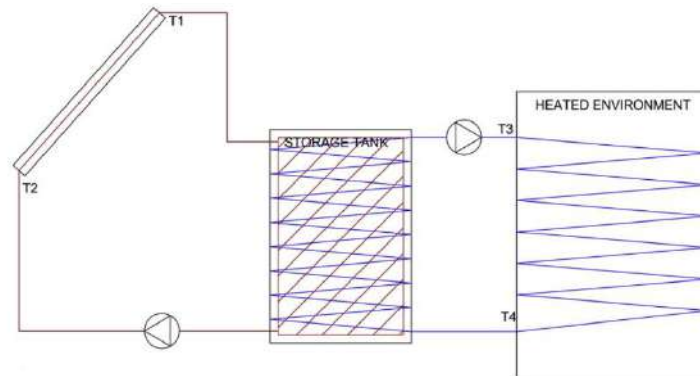


Figure 1-6. Schematics of the prototype studied by (Serale, et al., 2015)

The results produced by this experiment showed that the use of mPCS as HTF is promising, especially for low temperature applications (about 40°C). However, the system presents some technical issues related to the stratification of the HTF in the storage tank, which if not subjected to continuous mixing risks to incur into the separation between the mPCS and the other components of the slurry solution.

Another innovative solution was proposed by (Hailot, et al., 2011), who, after studying the properties of different composites made of compressed expanded natural graphite (CENG) and various PCMs (paraffins, sodium acetate, ...), designed an ICS composed of a flat plate collector with a CENG/PCM storage section in direct contact on its backside. The collector was then placed inside a casing made from a polymer.

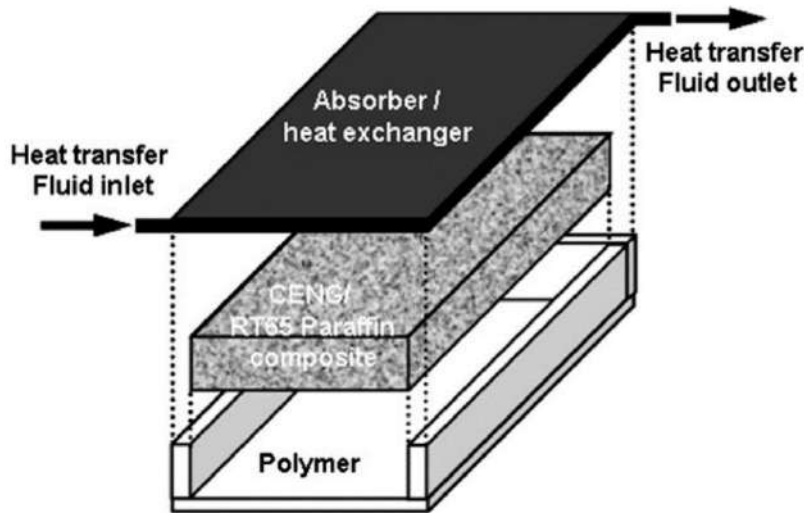


Figure 1-7. ICS-CENG/PCM design (Hailot, et al., 2012)

The originality of this experiment consists in the fact that the traditional storage tank, typical of almost all solar domestic hot water (SDHW) systems, is totally removed. In its place, the PCM compound has been placed directly on the back of the absorber, making available both the solar collection and the storage section in a single element.

The experimental phase of this project was followed by the development of a mathematical model, which was validated with experimental data. In the development of this latter the author has simplified the simulation of the PCM section by dividing it into 5 different temperature nodes between which the respective energy balances have been established (Hailot, et al., 2012). A similar approach will then be applied to the development of a numerical model to describe the prototype studied in this work.

Further experimental studies on ICS, although not directly involving the use of PCM or heat pipes, have been carried out by (Souza, et al., 2014). The authors have in fact studied in depth the behaviour of a thermal storage cavity positioned on the back of an absorber. By simulating solar activity through a heating plate, with the same thermal properties as solar radiation, it was possible to study the energy responses of the storage section, particularly focusing on thermal stratification and convective thermal exchange. In the experiment conducted, the storage medium used was distilled water. The results obtained showed unsatisfactory thermal stratification, with a limited temperature difference between the upper and the lower part of the cavity, demonstrating the need for

an additional element capable of promoting the stratification process. The experiment therefore showed how the use of ICS often requires implementations that are slightly different from the traditional ones. The positioning and design of the storage section, which in an ICS must be an integral part of the collector require particular attention and must take into account not only an efficient mechanism of energy transfer, but also problems related to the spatial placement of the internal elements.

1.4.2 The new concept

Starting from the considerations made in the previous paragraph, in which the state of the art regarding integrated solar collectors (ICS) has been exposed, it has been possible to define the development of a new collector concept. Taking into account the positive and negative aspects of previous experiments, it was decided to develop an ICS prototype for DHW production that could meet the following requirements:

- High energetic performance in cold climates
- Prevention of freezing risk
- Simplicity of operation
- Architectural integration
- Comparable cost with traditional systems

In order to achieve these goals, a classic flat-plate collector has been integrated with three other main design elements:

- 1) **Heat pipes** filled with methanol, used as a means of transferring heat from the absorber surface to the storage section. The use of the heat pipes, being installed with a slight inclination, foresees the operation with a thermosiphon mechanism. The expected result is a high thermal heat exchange, as well as the effect of a thermal diode.
- 2) Storage section by means of a cavity containing **PCM**. In order to achieve better both energy and structural performance, the cavity has been designed as an aluminium structure made of honeycomb cells, inside which the phase change material will be arranged. This also made it possible to reduce the storage thickness to contain the overall dimensions of the ICS.
- 3) Total **thermal insulation** of all elements within the same casing. This choice, combined with the installation of the heat pipes, allows to obtain a storage section completely isolated on all its sides, possibly reaching the thermal capacities of a classic storage with an insulated water tank.

From the analysis of the state of the art, it has not been possible to identify a similar ICS system that integrates within the same casing the use of heat pipes coupled with a PCM. This makes the project studied unique from an experimental point of view. The principle of operation of the prototype, as well as the other elements of which it is composed, will be analysed in detail in the following chapter.

1.5 Performance indicators

Because of the uniqueness of this study, it was necessary to adopt specific evaluation measures to evaluate energy performance. Moreover, in a rather complex system such as the one in question, which involves various design elements, it is certainly not straightforward to define the correct quantities to evaluate the system's storage potential or its efficiency. The set of these quantities, also known as key performance indicators (KPIs), is essential to evaluate the quality and effectiveness of an energy system, especially when it involves a thermal storage, which therefore must be comparable with other similar technologies.

Among the most used KPIs in the literature, we certainly have storage capacity, efficiency and cost. For storage capacity we indicate the energy that can be accumulated in certain reference conditions. Efficiency, secondly, is usually expressed as the ratio between the energy that the storage can supply and the energy provided to the system by an external source (Komarnicki, et al., 2017).

However, the use of only the standard KPIs is very reductive to describe in a comprehensive way the performance of an energy system with thermal storage. For this reason, referring to the work proposed by Annex 31 from (IEA, 2018), additional KPIs were introduced, with the aim of providing, through a group of parameters, a complete and exhaustive description of this type of systems. Among the KPIs proposed by the IEA we have:

- 1a. Total capacity (C_t) [Wh]: the energy that can be accumulated in reference conditions.
- 1b. Maximum useful capacity ($C_{us,max}$) [Wh]: the maximum energy that can be provided without negatively affecting the storage.
2. Recharging energy (C_r) [Wh]: the amount of energy that must be supplied to the accumulation in such a way that it reaches the total capacity (C_t).
- 3a. Maximum charge power ($P_{c,max}$) [kW].
- 3b. Maximum discharge power ($P_{d,max}$) [kW].
4. Depth of discharge (DOD) [%]: indicates the percentage of storage that can actually be used. A 100% DOD means that the storage can be completely discharged.
5. Durability (N_t) [-]: represents the number of loading and unloading cycles to which the accumulation can be subjected without its storage capacity falling below 75% of the nominal capacity.
6. Specific cost of the storage (SC_s) [€/kWh]: represents the global cost (initial investment, maintenance and decommissioning) normalized to the energy that the system is able to supply during its life cycle.
7. Maximum self-discharge rate (SD) [%]: indicates the percentage of total accumulated energy that is lost even if the system is not charged or

discharged. The percentage value should be provided for standardized time periods (1, 10 or 100 hours).

- 8a. Storage size (S_t) [m³]: this is the volume occupied by accumulation equipping.
- 8b. Storage weight (W_t) [kg]: is the storage total mass.
- 9a. Energy storage factor on demand (ES_d) [%]: it is the percentage ratio between the energy released by the storage and the total energy demand for certain purpose (heating, DHW, etc.).
- 9b. Energy storage factor on demand (ES_{res}) [%]: it is the percentage ratio between the energy released by the storage and the energy produced by renewable sources for the same purpose (heating, DHW, etc.). Usually this last parameter is associated with the building where the energy system is installed.
10. Generated energy/cost saving (E_{sav} [kWh]/ CO_{sav} [€]): these parameters indicate the energy and economic savings that are expected from the installation of the energy storage. It is usually referred to a standard period and refers to the energy costs of the building where the system is installed.

The KPIs mentioned above will be considered during the experimental phase of this work and will be presented later in the Table 4-2 at the end of Chapter 4, making references to the experimental values obtained.

However, in addition to the proposed parameters, it is necessary to define in a clear way the main energy flows within the prototype. With reference to similar systems already analysed in the state of the art, the following quantities related to the prototype under examination have been defined:

- Heat pipe heat transfer coefficient: summarizes in a single parameter the heat transfer capacity through the heat pipes. it has been calculated following the definition of (Nemec, et al., 2011):

$$U_{HP} = \frac{\dot{Q}_{HP}}{T_{eva} - T_{cond}} \left[\frac{W}{^{\circ}C} \right]$$

- Stored power: represents the thermal power transmitted by the absorber towards the storage cavity:

$$\dot{Q}_{sto} = U_{HP} \cdot \#_{HP} \cdot \Delta T_{abs/front} [W]$$

- Lost power: it is the heat power dispersed from the storage cavity towards the external environment, where the coefficient D represents the global heat exchange coefficient and the temperature $T_{pe,m}$ is the average temperature of the front plate of the cavity.

$$\dot{Q}_{loss} = D \cdot (T_{pe,m} - T_{ext}) [W]$$

- Thermal efficiency of the system: defined as the ratio between the useful heat transferred to the storage through the heat pipes and the solar radiation that hits the absorber (Robinson, et al., 2013):

$$\eta = \frac{\dot{Q}_{sto}}{E \cdot A_{abs}}$$

- Finally, the power extracted from the storage by the domestic hot water heat exchanger is simply defined as:

$$\dot{Q}_w = \dot{m}_w \cdot c_{p,w} \cdot (T_{in} - T_{out}) [W]$$

Chapter 2

2 Prototype description

The main objective of this thesis is to test the reliability of a very particular Integral Collector Storage (ICS) (Fraisie, et al., 2017). In this chapter the studied prototype will be presented. Every single component included in the system has a specific role to ensure the proper functioning. The following sections will give a comprehensive review of the collector operations, starting from a general vision and then going into the specific of the prototype manufacturing and commissioning stages.

2.1 System presentation

As already stated, an Integral Collector Storage (ICS) is a complete thermal system able to collect and store the solar energy into a single device. The prototype examined is unique and not intended for the commercial market. The system under study belongs to a new ICS concept which brings together different objectives within a single machine: high energy performances in cold climates avoiding freezing issues, simplicity of operation, good architectural integration with reasonable production cost comparable with market-ready solutions.

To achieve these goals the studied prototype is made-up of several elements connected each other and installed inside the same casing:

- Collector section composed by a glass coverage, an air gap and the flat absorber layer;
- Heat pipe section, connecting the absorber to the storage;
- Storage cavity made up of honeycomb cells with PCM;
- Insulation layer all around the storage section.
- DHW heat exchanger, welded to the front side plate of the cavity.

The technological innovation proposed by this new concept is based on the integration of the heat pipes, used as heat flux carrier, with a PCM storage. These two elements, unconventional for the standard solar collector available on the markets, are coupled in the same device, providing at the same time an insulated solar circuit and a storage section. Figure 2-1 shows the prototype scheme with all the aforementioned components and their relative position. A proper slope is given to the prototype to optimize its solar energy collection.

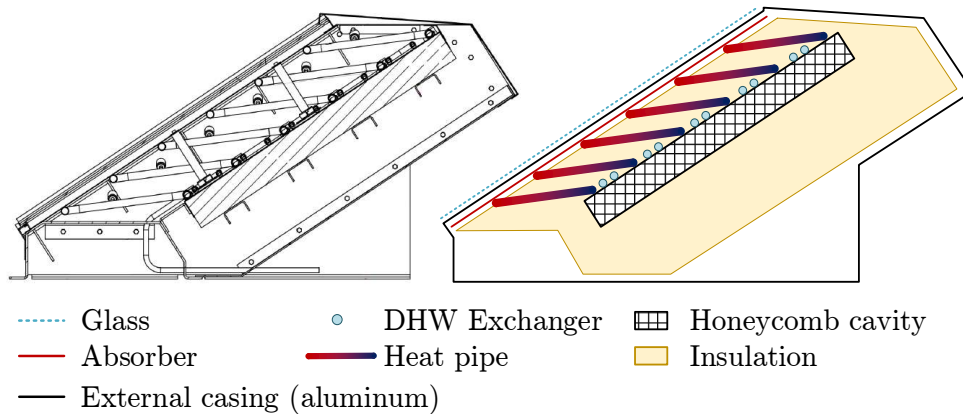


Figure 2-1. Prototype main components

As it can be noticed from the picture, the heat pipes section behind the absorber has a slight inclination upward in order to allow a thermal-diode behaviour: in this way the solar energy collected can only be transferred from the absorber to the storage and not in the opposite direction. A primary role, especially for cold climate applications, is also played by the insulation layer, which constitutes a considerable part of the prototype. Since the whole system is designed to be placed outside, high insulation properties are needed to reduce, as much as possible, thermal losses. The storage section of the system, unlike typical solar thermal solution, is installed outside and therefore the insulation can consistently affect the global energy performances. Furthermore, what distinguishes this thermal collector from similar ones (Hailot, et al., 2011) (Robinson, et al., 2013) is the storage cavity, consisting of an aluminium box divided into a multitude of small cells, always made of aluminium, with a honeycomb shape. This peculiar structure was designed to improve the heat exchange performance between the PCM, that is placed inside each cell, and the rest of the system. The honeycomb shape choice provides a greater exchange surface, providing excellent performance to mechanical stresses while maintaining a contained thickness, fundamental for a proper architectural integration.

2.1.1 Principle of operation

The principle of operation is now described. For the sake of simplicity, the solar energy flow can be considered. Solar radiation hits the front face of the collector, consisting of a simple flat-plate absorber section with a glass cover, commonly used by standard systems. Absorber converts solar energy into thermal power, that is immediately given to the heat pipe section which makes contact with the back side of the absorber. Once solar energy reaches the heat pipe section, energy is transferred to a heat transfer fluid (HTF). Heat pipes are made by U-shaped copper tubes, hermetically sealed and filled for 30% of their volume with methanol. Liquid methanol settles on the lower part of the heat pipe, right behind the absorber. Thermal heat transferred from the absorber makes the methanol evaporate. Gaseous methanol is now free to move towards the highest section of

the heat pipe, where it faces the colder storage cavity wall and condensates, reaching again the liquid state and flowing back to the lowest section. We can now distinguish two main segments: the evaporator section, behind the absorber and the condenser section, next to the storage cavity.

Figure 2-2 points out the energy loop that occurs inside the heat pipe, where the heat carried is the methanol. Such solution makes advantage of the heat pipe slope to create a classical thermosiphon heat cycle, based on natural convection driven just by gravity, that does not need any auxiliary equipment such as a mechanical pump. Furthermore, the benefit of such solution is to allow the heat flux to flow only in one direction, from the evaporator to the condenser, making the most of the incident radiation on the absorber and avoiding energy losses due to a reverse energy flow. Finally, the process does not include any control device and the heat flow that passes through the heat pipe is proportional to the temperature difference established between the evaporator and the condenser.

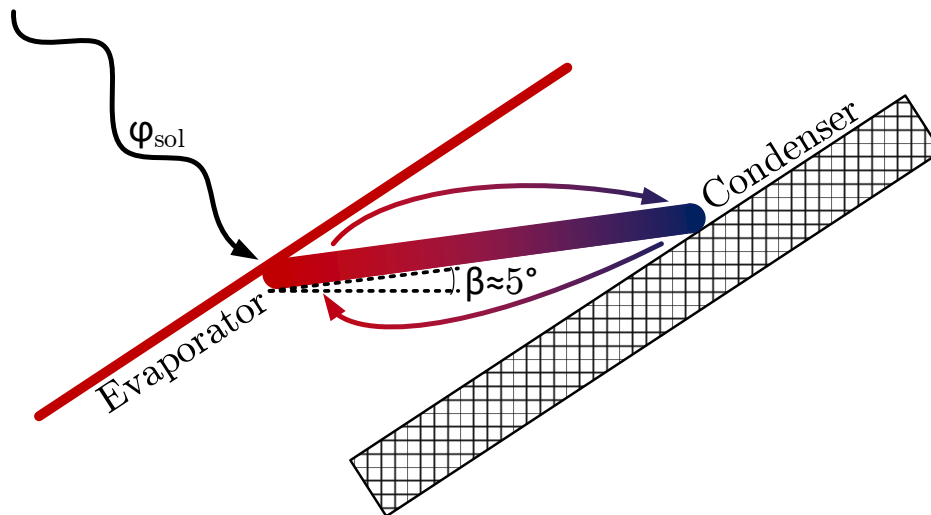


Figure 2-2. Heat pipe energy loop

After that the solar energy has been transferred to the condenser, it flows inside the aluminium cavity and heats the PCM up. The heat exchange occurs on the cavity front plate, where the condenser section is welded. Flowing inside the cavity, the solar heat increases the PCM temperature until it reaches the double phase region and starts melting (around 60°C). Regarding the phase change material, polyethylene glycol (PEG) was adopted because of its advantageous physical properties, which will be addressed later. PEG was placed inside the honeycomb cells of the cavity with a filling rate of 75% that allows the material to expand during the phase change without compromising the mechanical stability of the structure. The honeycomb pattern is kept in position by two aluminium plates on both sides. Now that the energy is stored in the PCM, it is ready to be supplied to a hydraulic circuit in order to provide domestic hot water (DHW). A new energy loop is therefore introduced into the system, consisting of a DHW pipeline installed in the same position of the heat pipe

condenser, on the cavity front side. This strategic placement provides a double advantage from an energy point of view: on one hand allows the cavity to discharge energy on the pipeline, on the other makes available a direct energy transfer from the condenser to the pipeline, avoiding the energy storage step. This last scenario might be useful when the heat production matches the hot water demand: in this case the heat flowing through the heat pipe can be directly discharged towards the DHW pipeline, since the HP condenser and the DHW exchanger are welded on the same plate (aluminium cavity front plate). The heat exchange is therefore predominantly conductive through the cavity front plate. The DHW pipeline is made by a simple copper pipe. For our study purposes, cold water from the network is intended to flow inside the pipeline. When the user needs it, a certain water flow goes through the pipe increasing its temperature.

To summarize, several energy fluxes are involved in the prototype principle of operation:

- 1) Heat flow through the heat pipes, with methanol as heat carrier (ϕ_{HP});
- 2) Heat flow from the condenser to the PCM, charging the storage;
- 3) Heat flow from the PCM to the DHW, discharging the storage;
- 4) Direct heat flow from the condenser to the DHW, bypassing the PCM

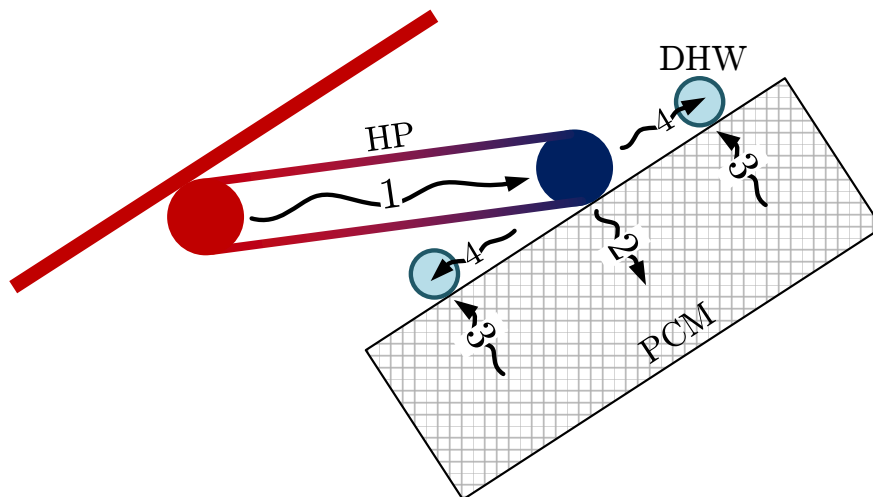


Figure 2-3. Principe of operation and main heat fluxes

Moreover, three different heat carriers are involved in the system:

- 1) Methanol inside the heat pipes, transferring solar radiation from the absorber to the cavity and acting as a thermal diode;
- 2) PEG inside the aluminium cavity, as a storage element;
- 3) Water in the DHW pipeline, extracting the energy produced and stored in the collector.

Comparing it with traditional solar thermal systems, this new ICS concept makes it available a stand-alone installation with no needs of external equipment. This prototype wants to introduce a simple and effective solution for DHW production with solar energy, taking advantage of its simple installation, good

architectural integration and appropriate insulation to avoid freezing risks in cold climates. After the literature review, no systems combining heat pipes, fully insulated storage and PCM in a honeycomb structure were found. This will certainly give to the study a unique value for the development of similar technologies. The following chapters will investigate its energy performances, making considerations about its reliability and efficiency.

2.2 Manufacturing

The manufacturing process involved different partners that took part in the project. The main task was to develop a reliable machine able to meet all the objectives set in the design phase. Apart from the flat absorber, all the other elements are the result of a careful analysis. The prototype has an opening area of 0.5 m² (1m x 0.5m) and a maximum height of 0.427m (Figure 2-4). The absorber slope is not adjustable and set to 33°.

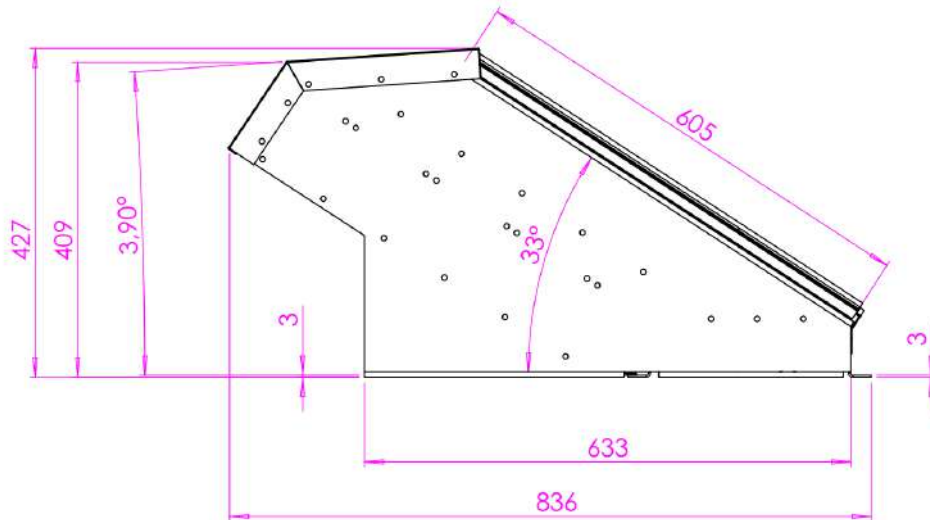


Figure 2-4. Prototype main dimensions (mm)

2.2.1 Honeycomb storage cavity

The cavity that contains the phase change material consists of three elements: two aluminium plates and the honeycombs internal structure. The interior of the cavity counts on more than 6000 cells with a hexagonal shape, a frontal section of 0.74 cm² and 0.04 m height. Each cell of the structure has been filled for 75% with the phase change material. Afterwards, the structure was vacuum-assembled with the two panels, in order to avoid that the material inside could migrate from one cell to another. PEG is therefore able to expand when it melts, without moving from its original cell. In this way the amount of PCM in each cell it is kept constant during normal operation condition, giving the cavity a homogeneous thermal and mechanical behaviour.

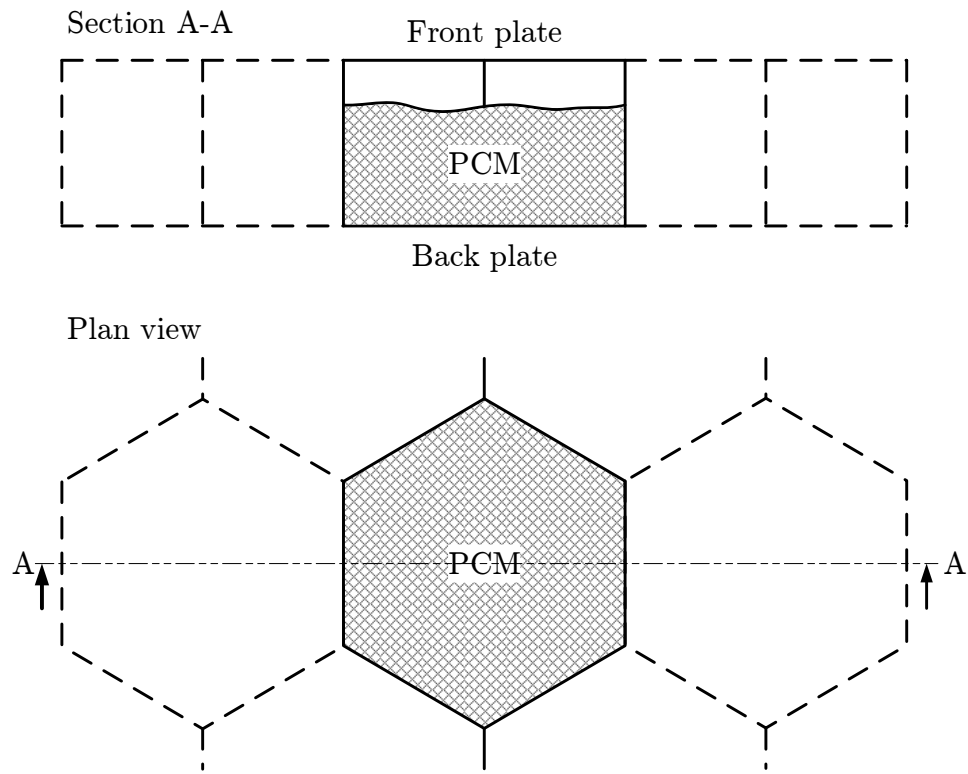


Figure 2-5. Honeycomb cell (detail)

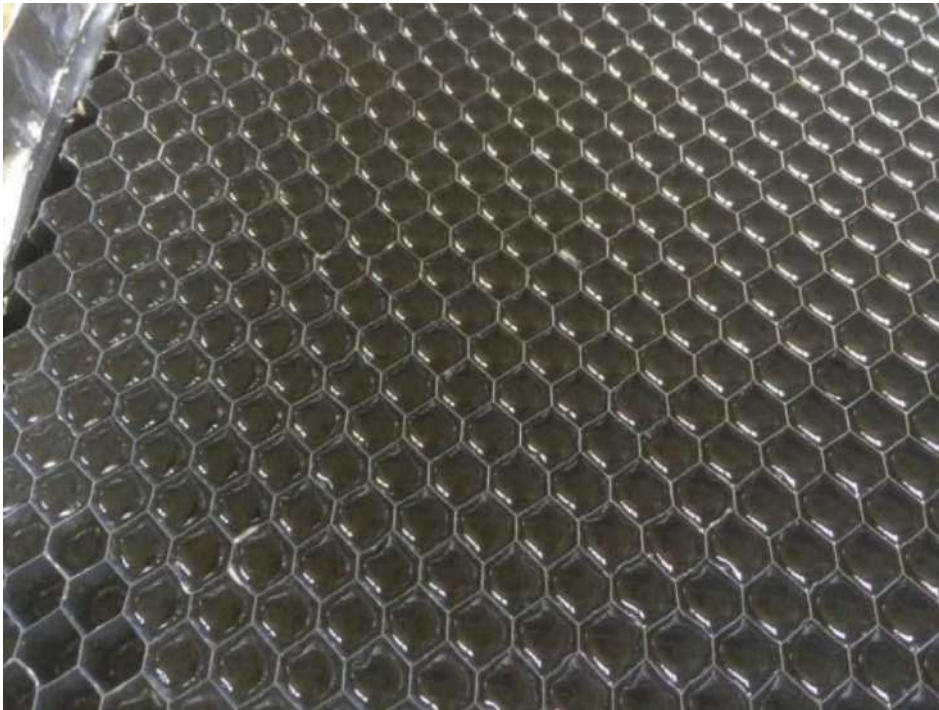


Figure 2-6. Honeycomb structure

The entire storage cavity has been made of aluminium to improve the thermal performances and at the same time limit the weight. The choice to use the honeycomb shape seemed the best solution to place the PCM in the most uniform way possible and to allow an effective heat exchange between the structure and the aluminium plates. The honeycomb structure was sealed on both sides by welding the two aluminium plates on it. Once the cavity has been manufactured, it is no longer possible to open it without compromising its operation.

2.2.2 Heat pipes

Six heat pipes have been installed in parallel between the absorber and the storage cavity. Methanol was chosen as phase change working fluid. Three main sections can be identified:

- 1) The evaporator, that collects the solar energy;
- 2) The adiabatic heat transfer duct;
- 3) The condenser, that gives back the collected heat to the storage.

The advantages that led to the choice of heat pipes concern both mechanical and thermal operation. From the mechanical point of view, heat pipes do not need any auxiliary equipment such as pumps to move the working fluid, that starts moving only thanks to the thermosiphon effect, based on natural convection. This gives the machine a passive functioning, as intended for the purpose of the prototype. Thermally speaking, the installation of the heat pipes inserts a thermal diode into the system which allows the heat flow to flow only in the desired direction, increasing thermal efficiency.

The heat pipes have a U-shape geometry with two long sides (1-meter length) horizontally installed representing the evaporator and the condenser. The short side, about 0.2 m, has a slight slope. The inner diameter is constant, and it is equal to 1 cm. Methanol was chosen as working fluid, because of its physical properties related to the operational temperatures, which can reach 100 degrees C. At these high temperatures the operating pressure does not exceed 4 bars. Other fluids considered by (Fraisie, et al., 2017), like ammonia, might reach dangerous pressure values at those temperatures, compromising the heat pipe functioning. Finally, the choice of methanol made it possible to adopt copper as a construction material, reducing costs compared to the use of aluminium.

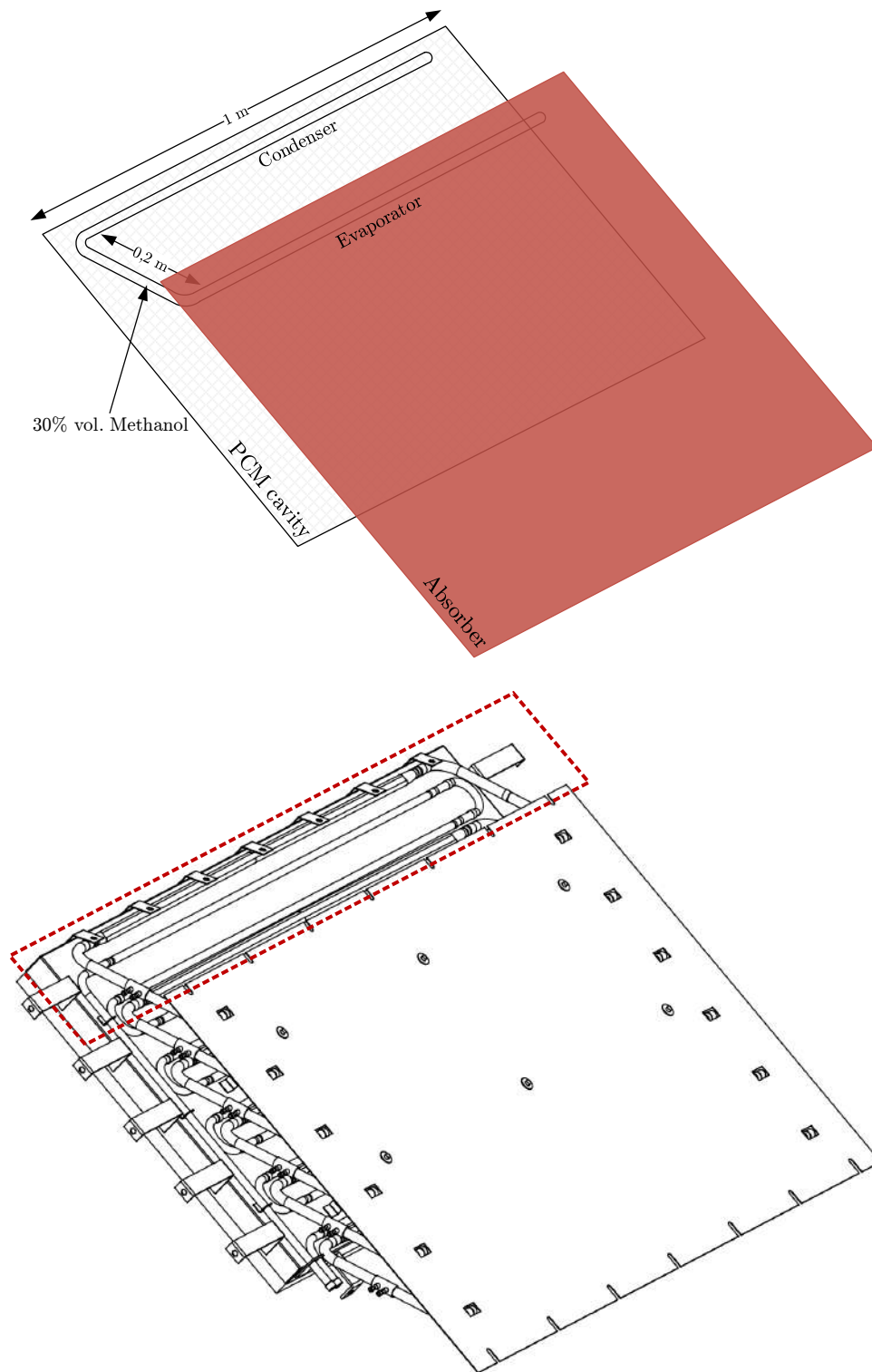


Figure 2-7. HP section (detail)

2.2.3 Domestic hot water (DHW) exchanger

The DHW exchanger was designed according to the required power output, based on the water temperature increase and the water flow. The exchanger consists of a simple copper pipeline with a total length of 12 meters. Internal and external diameter are respectively 6 and 8 mm. The exchanger pipe was placed alongside the heat pipe's condenser on the upper cavity plate to favour the direct heat exchange with the condenser. The water pipeline is the only elements of the system that communicates with the external environment, allowing an external water flow to pass through the prototype and collect the heat stored inside it. The exchanger was designed to operate with a relative low water flow, around 1 liter per minute, and with a temperature rise of about 40 degrees C between inlet and outlet. As it can be seen later in the analysis when operation conditions differ a lot from these settings the system will not be very performant.

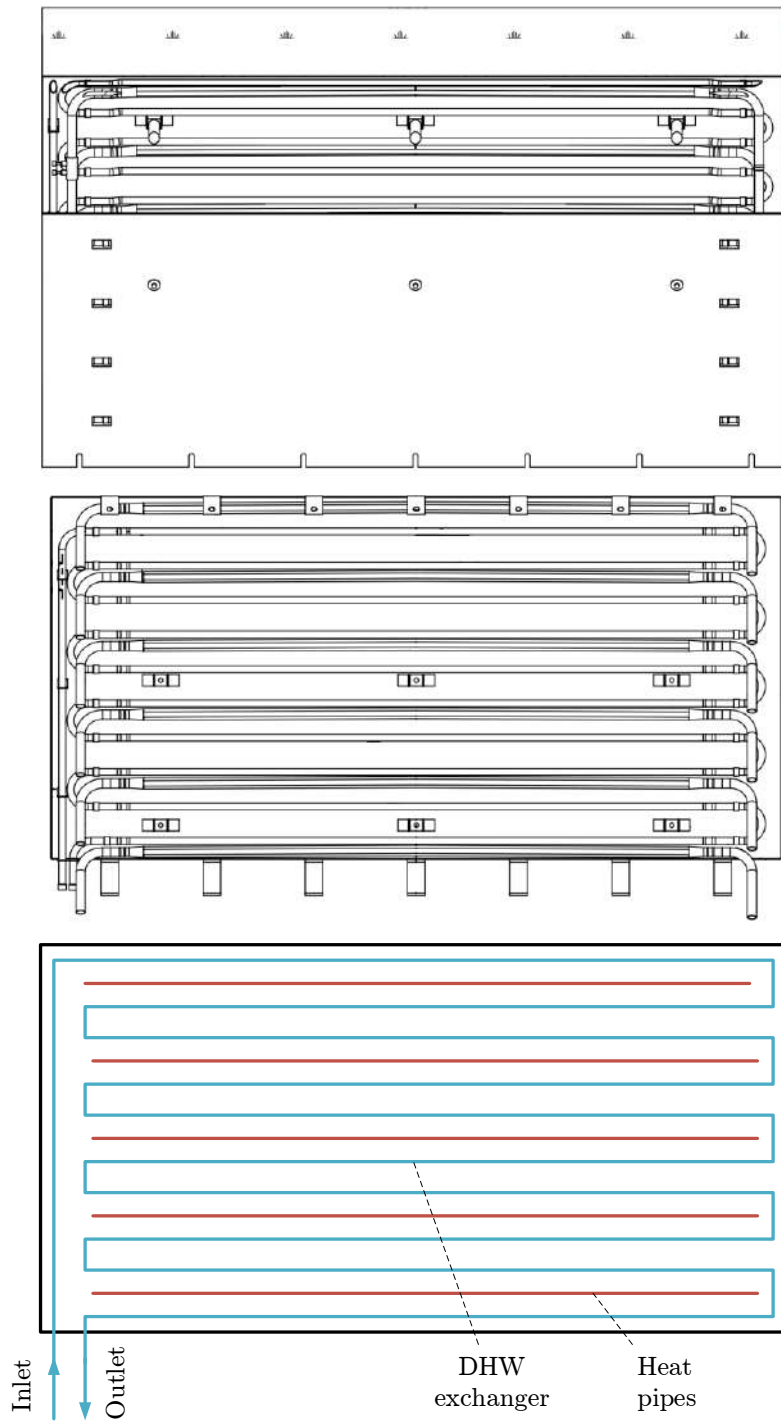


Figure 2-8. Heat pipes and DHW exchanger design

2.2.4 Phase change material (PCM)

The choice of the material to be adopted for the prototype was made following a careful analysis of the physical and energy parameters of a series of candidate materials. A first consideration was made regarding the melting and freezing temperature range of the material. For our purposes, in order to make the most of the phase change, the melting temperature should lay around 60°C. This temperature can be easily reached by a solar thermal collector, fully exploiting the phase change latent heat. However, the material must be able to withstand much higher temperatures, which can even reach 100 degrees C. Moreover, in order to obtain high performances from the thermal point of view, the thermal conductivity, the specific heat and the latent heat should be maximized. Since there are also some mechanical constraints to be respected, the density of the material should be as high as possible, so as to ensure a reduced thickness of the storage section. Finally, as in any design choice, the price should be reasonable.

In view of the above, the choice was to adopt Polyethylene glycol (PEG), with a molecular weight of 6000 g/mol, a polyether compound rather used in the medical and chemical industry. The product is marketed in solid-state grains, which solidifies in a single block after the first melting and crystallization cycle, losing the initial granularity. PEG 6000 meets almost all the required characteristics. Its specifications are collected in Table 2-1.

Table 2-1 - PEG 6000 specifications

Polyethylene glycol 6000 (PEG 6000)

<i>Property</i>	Value	Unit
<i>Melting range</i>	55-62	C
<i>Melting latent heat</i>	192	kJ/kg
<i>Specific heat capacity (sensible)</i>	2.3	kJ/kgK
<i>Conductivity</i>	0.2	W/mK
<i>Density (solid)</i>	1210	kg/m ³
<i>Price</i>	2.8	€/kg

The melting range of this compound perfectly fits our DHW production purpose, since water is usually supplied at a temperature lower than 60°C. Having a double phase region around 60°C allows to take full advantage of the latent heat that PEG could store.

All the characteristics presented above have been provided by the supplier of the material. However, during this study, some of them will be further investigated and verified through appropriate methods.

The choice of adopting a phase change material allows to reduce considerably the storage volume compared to a classic system with water storage, taking advantage of the latent heat. For instance, assuming to heat from 20 °C to 70 °C both a volume of water and PEG 6000, the volumetric energy stored in the PCM is more than 1.5 times greater (Fraisse, et al., 2017). Increasing by 50 °C, the heat stored by the water is purely sensible ($\rho c \Delta T$), while the PEG 6000 in that temperature range will be able to store also the latent heat (ρL), since the melting occurs around 55 °C:

$$\begin{aligned} \text{PEG 6000} : \rho L + \rho c \Delta T &= 1210 * 192 + 1210 * 2.3 * 50 = 371470 \frac{\text{kJ}}{\text{m}^3} \\ \text{Water} : \rho c \Delta T &= 1000 * 4.187 * 50 = 209350 \frac{\text{kJ}}{\text{m}^3} \end{aligned}$$

To keep geometrical dimension as low as possible, as well as the prototype weight, the final cavity thickness was set to 4 cm and filled with 0.015 m³ of PCM inside.

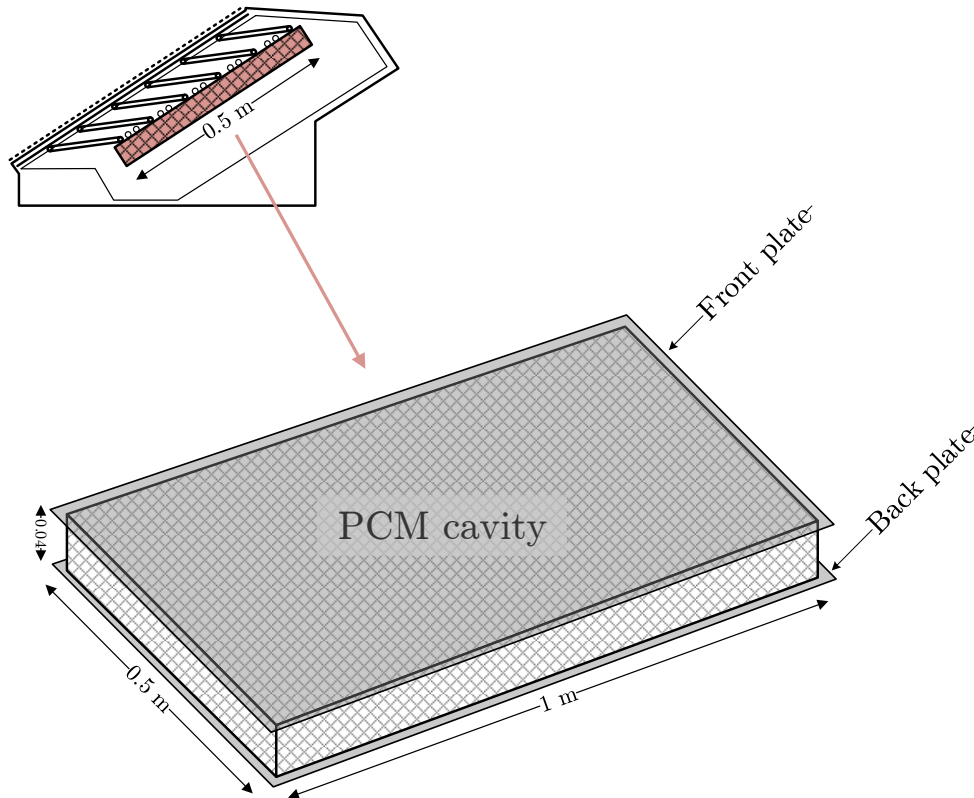


Figure 2-9. PCM cavity section with dimensions in m (detail from Figure 2-1)

2.3 Possible advanced installations

Even though most of the following analyses will focus on the reliability and the energy performances of the single prototype under study, this solar collector should not be seen just as a single stand-alone unit. Looking at a bigger picture, the final idea is to implement a certain number of this kind of ICS in a parallel network, in order to provide a reasonable amount of thermal energy comparable with conventional solar thermal system. For this reason, is important to remark since the very beginning of this study that all the results found investigating on this machine should not be directly compared with conventional systems, especially when speaking of energy output. A more realistic scenario would involve more ICS units coupled in a parallel water circuit, so as to make up a solar field with a solar facing surface in accordance with the energy demand. Since a single unit has an opening surface of just 0.5 m^2 , a realistic design for a typical family house should involve around 8 units like the one taken into consideration, in order to provide a total solar collecting area of 4 m^2 . The advantage of such solution for domestic application is to have an almost independent system that can be totally installed outside and easily integrated with standard DHW production equipment. The whole system has been designed for a classical rooftop installation, with no need of extra room for the auxiliary equipment, leading to a considerable space-saving. The global weight of the entire device is around 60 kg.

However, a possible extra equipment installation might include a simple water pipeline that couples the water flowing inside the ICS units and the one coming from the public network. For the sake of simplicity, during the performances tests, water was withdrawn directly from the network and forced to flow inside the collector pipeline. After a single investigation on the waterflow processed and its temperature rise, water was discarded and not used for further applications.

The following section will point out the bench test used to evaluate the prototype performances in different climates conditions. Although the installation could be slightly different from a definitive building implementation, the main placement conditions have been kept similar. The following pictures show the bench test installation (Figure 2-10) and a possible building implementation with several units (Figure 2-11).

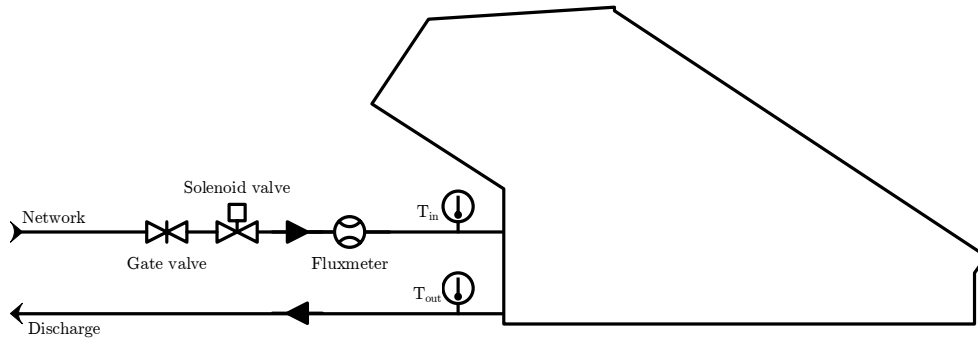


Figure 2-10. Bench test scheme

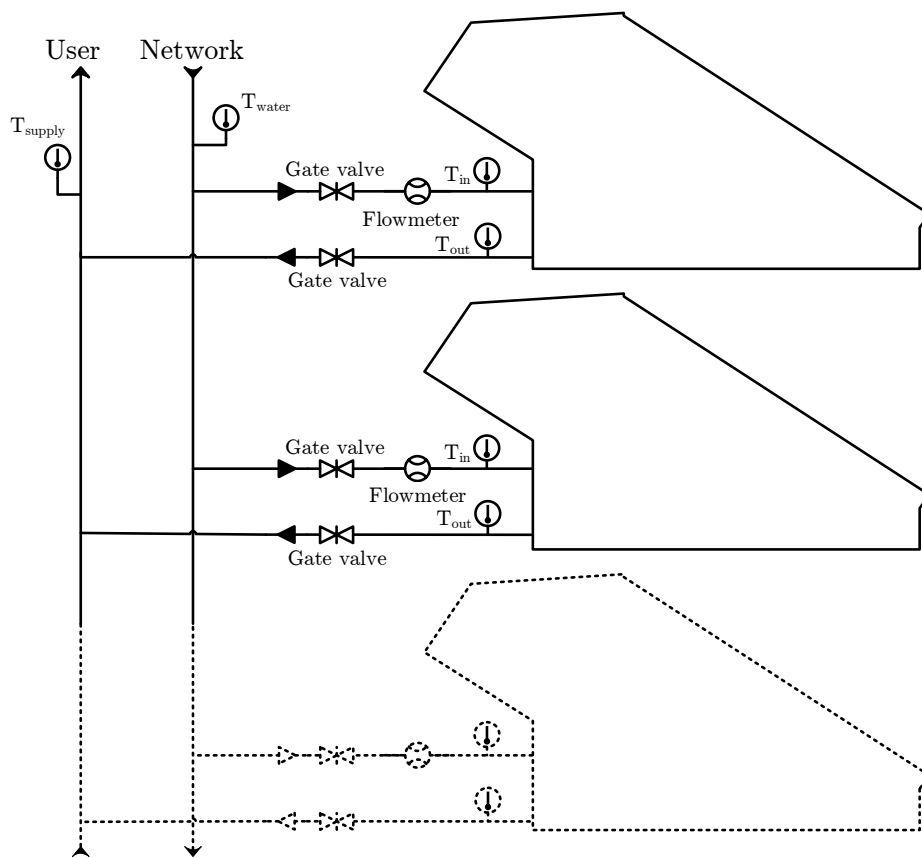


Figure 2-11. ICS implementation for a building

Both the bench test and a multi-units installation have a very simple hydraulic scheme, meaning the ease of installation of this system. The hydraulic equipment they need is simple without involving expensive and peculiar tools. In both the schemes presented a control system is missing, especially for the building implementation case, where it plays an important role.

2.4 Bench test

In order to study the thermophysical characteristics, the prototype was installed on a test bench composed of the apparatus itself, the external source of water and all the necessary sensors to study its behaviour. An aluminium structure encloses all the elements just explained and makes each module self-supporting. Since the storage cavity is the heaviest element of the prototype, it has been anchored to the outer casing with 5 metal elements on each side, also in aluminium. Furthermore, 4 bars with a U-shaped profile are positioned on the back, to further support its weight and prevent it from slipping. As will be seen later in this study, the metal parts, while offering a solid mechanical stability to the system, consistently compromise the thermal performance, favouring the thermal exchange between the prototype and the external environment, which in our case translates into an increase in thermal losses.

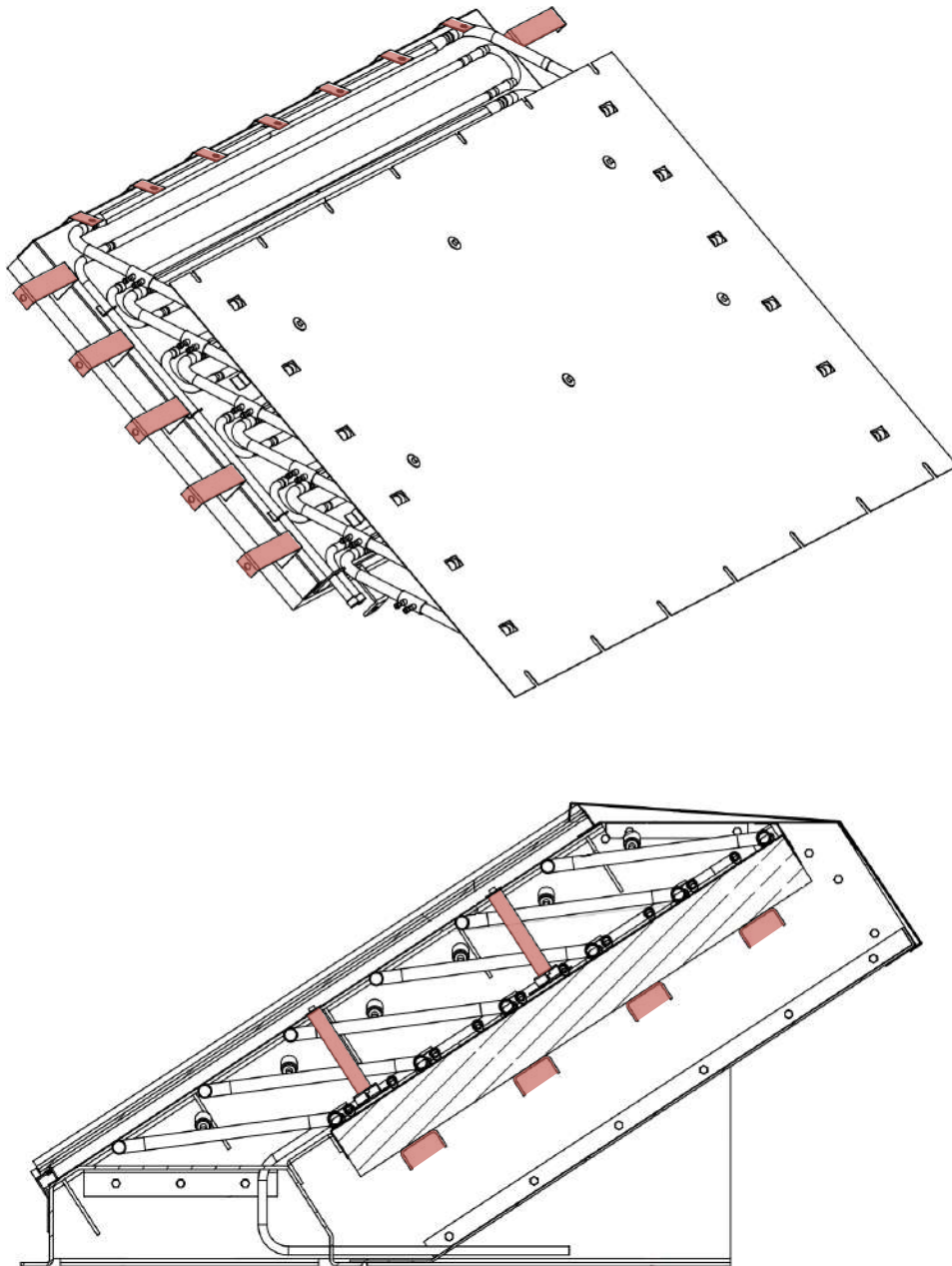


Figure 2-12 - Metal supports

The entire casing was then fixed to a cement structure positioned at the installation site, to prevent it from moving and guarantee a fixed angle of 33° . Two different installation sites were chosen during the experimental test phase. Initially, during the summer, the prototype was placed on the ground, inside a solar field predisposed to collecting data. During the winter testing phase, however, it was placed on a flat roof of a neighbouring building. Both locations are located in Bourget-du-Lac (France), inside the university campus of

Université Savoie Mont Blanc. This location perfectly recalls the climatic conditions for which the prototype was designed, i.e. a typically cold climate in winter and temperate in summer.

Between the two experimental test phases, the prototype underwent a test phase in a closed laboratory environment, during which some modifications and implementations were made to the structure to further improve its thermal properties.

The set-up of the test bench was completed by a series of sensors used to monitor the activity of the appliance. 25 K-type thermocouples have been installed in different positions to detect the temperature trend of different sections. Instead, a flowmeter measures the flow of water that flows inside the ACS exchanger. The solar activity is finally measured by a pyranometer, while the wind speed from an anemometer. Thermocouples, as well as the flowmeter, have been previously calibrated (Appendix 1). All data are then recorded in an Agilent 34972A acquisition units and stored in a USB device. An overview of the prototype, during the summer installation, is shown in Figure 2-13.



Figure 2-13. Bench test outside installation during summer period

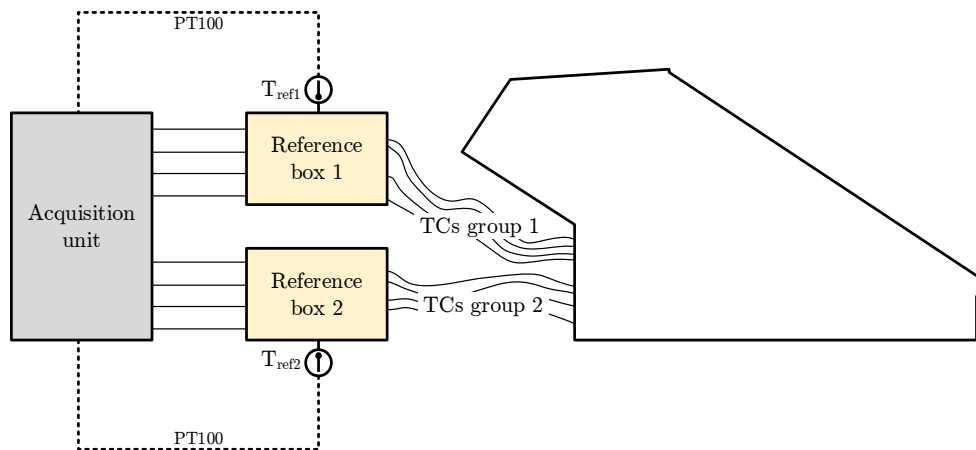
2.4.1 Thermocouples

After a calibration processes that involved a thermal bath in a lab environment, 25 K-type thermocouples were installed inside the prototype casing. In order to have a temperature as homogeneous as possible, several thermocouples were applied to the various sections of the prototype, according to the following table:

Table 2-2. Thermocouples installed

<i>Section</i>	<i>Nomenclature</i>	<i>Quantity</i>
<i>Absorber</i>	T_{abs}	4
<i>Air gap</i>	T_{la}	1
<i>Evaporator</i>	T_{eva}	4
<i>Condenser</i>	T_{cond}	4
<i>Front cavity plate</i>	T_{pe}	3
<i>Back cavity plate</i>	T_{pi}	3
<i>Back side</i>	T_{ar}	3
<i>External air</i>	T_{ext}	1
<i>Water inlet</i>	T_{in}	1
<i>Water outlet</i>	T_{out}	1

After being applied, the thermocouples were assembled into two groups, so as to group the cold junctions just into two isolated boxes, thus having a uniform reference temperature. Finally, a connection was made to the data acquisition unit, where the potential differences of each individual thermocouple have been saved, as well as the reference temperature. For the latter a PT100 thermoresistance was used instead of a thermocouple (Figure 2-14).

**Figure 2-14. Thermocouples sensors scheme**

All temperature sensors installed have an accuracy of about 0.1°C . The following figures schematically summarize the various positions of the thermocouples inside the casing.

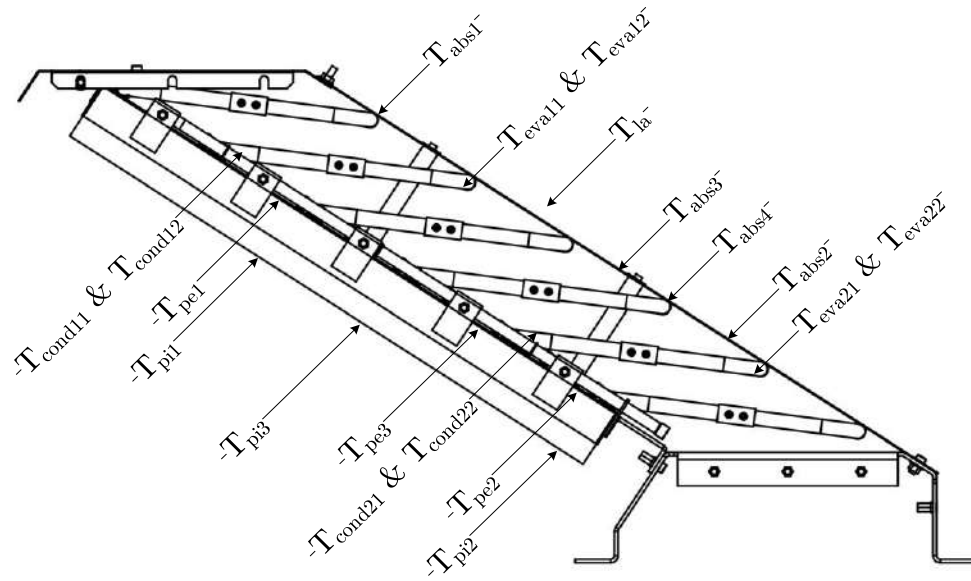


Figure 2-15. Thermocouples position in the casing

2.4.2 Acquisition unit

An Agilent 34972A data acquisition unit, manufactured by Keysight technologies, was installed to store experimental data collected on-site (Figure 2-16).



Figure 2-16. Acquisition unit

The unit consists of a two-slot mainframe, where the temperature sensors, as well as the pyranometer, flowmeter and anemometer sensors were installed. Data are stored into a USB device which a user-defined timestep. Accordingly to the experimental phase purpose, different investigation timesteps were used, from 5

seconds when water withdrawals were studied up to 1 minute for normal condition studies.

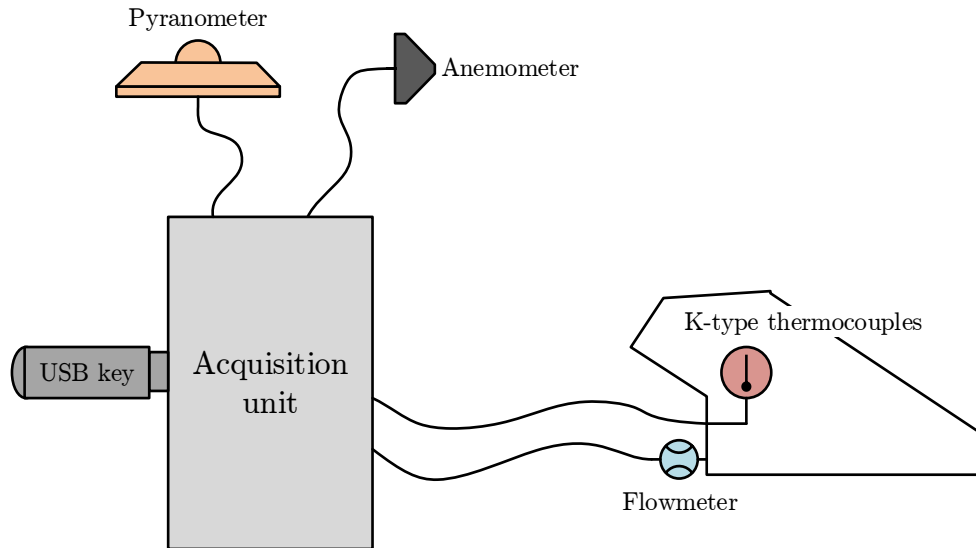


Figure 2-17. Acquisition unit connections

2.4.3 Extra experimental tools

Other instruments relevant for experimental purposes were the pyranometer and anemometer, useful for identifying atmospheric conditions, as well as the flowmeter, installed at the water pipe inlet, able to evaluate the flow of water flowing inside the DHW exchanger during withdrawals. In addition, a thermal camera was subsequently used during the test phase in the laboratory, in order to identify possible thermal bridges.

Chapter 3

3 Early stage performance analysis

After setting up the test bench, the experimental test phase has begun. Different scenarios have been analysed, taking into consideration different climatic conditions, both summer and winter. The experimental phase of the tests conducted did not involve only a collection of data in an external environment, but also several tests in an internal laboratory. The test period, which began in May 2017, ended in February 2018. In a first phase, the prototype's performance was studied in an external environment. The collector has in fact been positioned inside a solar field, anchored to a special structure to keep it in a fixed position (Figure 2-13). During this phase the general performances of the prototype have been studied, considering the trend of the temperatures inside it as well as the charging and storing capacity of the cavity with the phase change material. From these initial analyses, which lasted from May 2017 until November 2018, important information were obtained, allowing a first comparison between the studied prototype and commercial systems on the market. Furthermore, from this initial experimental analysis, some parameters missing from the design phase have been evaluated in such a way as to be subsequently implemented in the development of a mathematical model.

Once this first phase was completed, the solar collector was moved from the external environment to an indoor laboratory during the months of November and December. Further tests were carried out in this environment, putting aside the effect of solar radiation, but studying in more detail some aspects of the prototype which, according to the results of the first phase, seemed to require further studies. In fact, more attention was paid to the thermal losses and the performance of the domestic hot water exchanger. At the same time, some structural modifications were made to the prototype, with the aim of improving its energy performances. In the view of the changes made, new tests were conducted, comparing the new results with previous ones and obtaining significant improvements. As well as the previous phase, this series of experiments also made it possible to study in depth the behaviour of individual sectors of the collector, managing to extrapolate important parameters from the experimental analysis that were previously unknown, as they were not specified in the design phase.

A third test period saw the PEG6000, used as a phase change material, as a protagonist. Since the previous experiments have shown some gaps in the characterization of this material provided by the manufacturer, a series of experimental tests have been conducted on a PCM sample in the laboratory between January and February 2018. The main purpose of this phase was to characterize from the physically point of view the material used, investigating in detail its thermal properties such as specific thermal capacity and specific enthalpy. Moreover, with the same experiments it was also possible to determine

with greater precision the temperature range in which the material melts or crystallizes, leading to a different behaviour in the two cases, which had not been well specified by the manufacturer. The PCM characterization was performed using the differential scanning calorimetry (DSC) method. The advantage that this phase produced was an accurate description of the thermal behaviour of the material, especially in the phase change region, during which no exhaustive descriptions were provided. The results of these tests, while not directly influencing the operation of the prototype, have allowed us to extrapolate important data for the implementation of a future mathematical model, within which an accurate description of each individual component is necessary.

Finally, after completing the tests in the laboratory, the prototype was re-installed in an external environment. This time, however, the installation site has been changed, preferring a flat roof. This last phase of data collection, conducted during the month of February 2018, allowed to develop further considerations during the winter period, with a rather harsh climate. In this last phase, some water withdrawals were made, extracting thermal power from the prototype, after having connected it to a source of cold water coming from the state distribution network.

The results of each experimental test will be analysed in detail in the following paragraphs of the next two chapters. The analysis of the data will follow the timeline of the tests, as they have just been presented. However, some exceptions will be made for the part during which structural changes to the prototype have been made (Chapter 4) in such a way as to compare the results obtained before and after the changes as clearly as possible.

An added value that has been demonstrated by all these series of experiments has been a relative ease in moving the system, unlike traditional systems, which once installed can be hardly removed. In our case, the lack of auxiliary systems and the integration of the storage inside the casing have allowed considerable ease both in the movement of the prototype and in the installation of the same in different study environments.

As previously stated, the entire experimental phase was conducted at the university campus of the Université Savoie Mont Blanc in Bouget-du-Lac, France. The indoor premises have also been made available thanks to the same university, as well as the study equipment. The following diagram summarizes the timeline of the experiments carried out.

3.1 Energy evaluation parameters

The system analysed, as already seen during the literature review, is unique in its kind. For this reason, it was necessary to define some physical quantities that could be subsequently used to evaluate the energy performances of the prototype, so as to make it in some way comparable with other similar systems. The following energy powers have therefore been taken into consideration:

$$1) \dot{Q}_{sto} = U_{HP} \cdot \#_{HP} \cdot \Delta T_{abs/front} [W]$$

This relation represents the useful power transmitted and accumulated inside the cavity. U_{HP} represents the heat exchange coefficient of the heat pipe, which will be obtained in a specific experimental phase illustrated in section 3.3.2.

$$2) \dot{Q}_{HP} = U_{HP} \cdot \Delta T_{eva/cond} [W]$$

This definition represents the heat output carried by the heat pipe, which in this case also depends on the U_{HP} coefficient.

$$3) \dot{Q}_{loss} = D \cdot \Delta T_{pe/ext} [W]$$

With this report we want to estimate the total thermal power lost by the storage cavity to the environment. It is proportional to the temperature difference between external environment and storage cavity by means of the coefficient D , which is also evaluated experimentally in section 4.1.

3.2 Charge study

This first experimental phase, conducted in May 2017, was first and foremost to verify the proper functioning of the test bench. Furthermore, the prototype was subjected to a complete thermal discharge of the storage cavity every morning at 6:00 am, forcing a rather high flow of cold water equal to 9.3 l/min inside the DHW exchanger for a duration of 19 minutes. In this way it was possible to concentrate on the behaviour of the collector starting from a stored energy condition equal to zero and studying its energy charging phase thanks to the solar radiation collected during the day. The trend of the monitored temperatures, collected in Figure 3-2, shows the direct relationship between the solar radiation trend and the absorber temperature. In general, these first days of study had a fair solar activity, which allowed to a decent verification of the correct thermal charge process of the storage cavity.

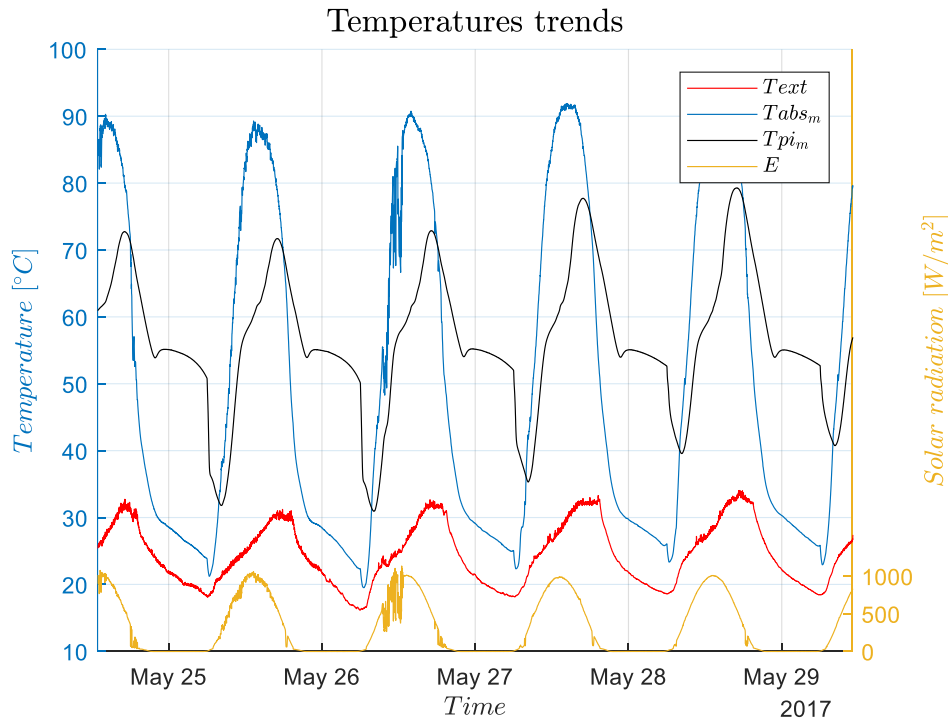


Figure 3-2. Main temperatures trend in May 2017

From the trends of the selected temperatures there is a clear relationship between solar radiation and the temperature of the absorber plate, as already stated. The solar radiation reaches peak values around $1000\text{W}/\text{m}^2$, which allows the absorber to reach a maximum temperature of about $90\text{ }^\circ\text{C}$. As regards the temperature of the storage cavity, the sensors positioned on the back of it have been taken into consideration. From the graph we can see the temporal phase shift of the latter, which has a certain thermal inertia with respect to the absorber. The temperature of the cavity can exceed $70\text{ }^\circ\text{C}$ every day. During daylight hours, it can be seen that the temperature of the cavity grows rather quickly thanks to solar radiation. However, when the latter fails, the temperature decreases just as quickly, immediately highlighting possible gaps in the thermal insulation of the cavity. During the night hours, the temperature of the cavity is established for several hours around $55\text{ }^\circ\text{C}$, forming a “plateau” easily recognizable from the graph. That region highlights the process of crystallization of the PCM, during which the solid phase and the liquid phase coexist. This phenomenon does not occur during the day, when the material passes from solid to liquid. This could indicate a different behaviour between the fusion process and the crystallization process, which will subsequently be analysed. Furthermore, the high values of solar radiation make the process of fusion of PCM much faster than that of crystallization. Finally, at 6:00 a.m. the temperature drops decisively due to the scheduled water withdrawal.

Another unexpected phenomenon that occurs during the cooling phase of the PCM is the so-called subcooling. As can be seen from Figure 3-2, before going through the crystallization phase, the PCM temperature is lowered and then goes back a couple of degrees C. This clear subcooling phenomenon allows the material to fall below the crystallization temperatures while still being in totally liquid state. Although this phenomenon does not seem to significantly influence the performance of the collector, it should be taken into account for future analyses, especially when the mathematical modelling is applied.

Since the temperature of the storage cavity is rather redundant during all the days in which this first experiment was carried out, the day of May 25 was chosen as a sample for a more detailed analysis on the way in which the temperature of the cavity increases. Focusing on the T_{pi} temperature trend during that day, it can be seen that the temperature of the storage increases very fast during the solid phase, while it slows down during the liquid phase. Furthermore, as expected, the phase change further slows this growth. Figure 3-3, describes the increase of T_{pi} during the day, from 8:00 am to 5:00 pm, a time interval in which the temperature is continuously increasing. For the sake of clarity, this increase was normalized over an entire hour, allowing a subsequent comparison with similar systems designed for DHW production. As can be seen, the average increase during the solid phase (which ends when PCM reaches 55 °C) is equal to 7.65 °C/h, almost doubling the average value recorded in the liquid phase (3.43 °C/h). The double-phase region, for obvious reasons, was excluded from this analysis.

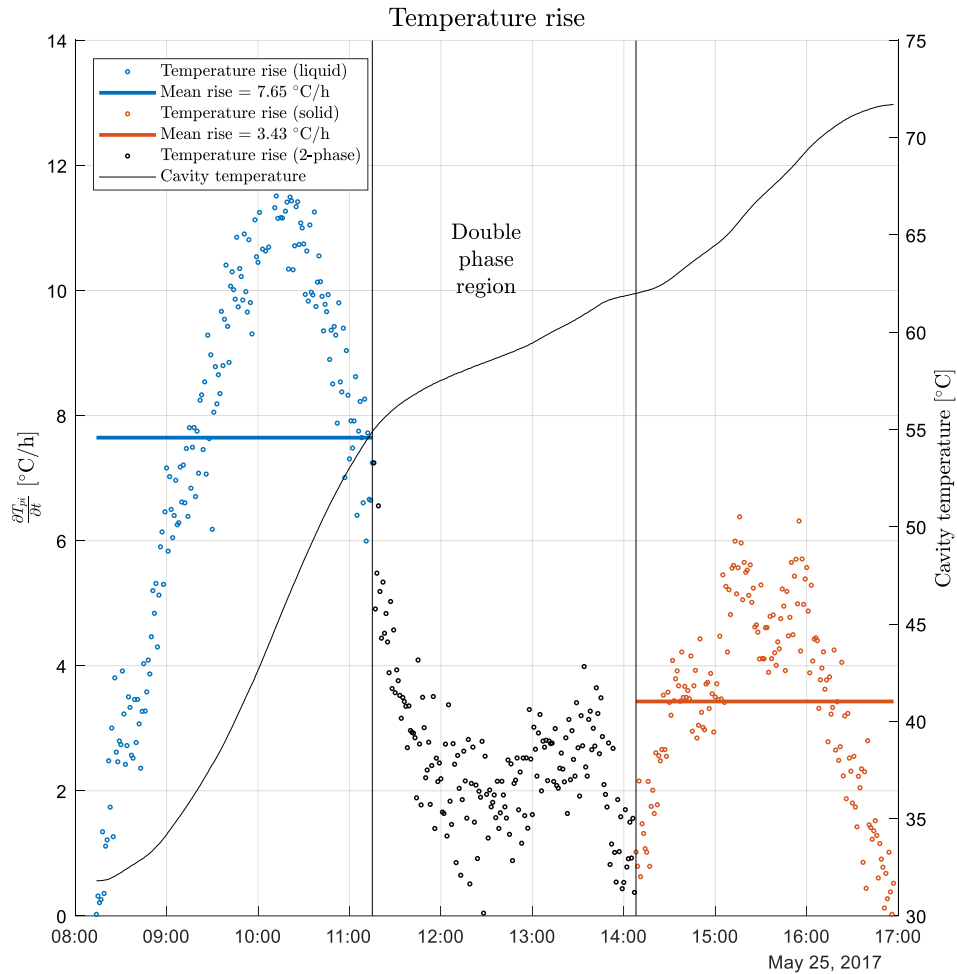


Figure 3-3. Hourly T_{pi} rise during cavity charging phase

The result obtained shows a rather satisfactory behaviour, especially when the material is in the solid phase, during which the heat exchange seems to be more effective. This allows the system to reach useful temperatures in the shortest time possible in order to produce DHW at a reasonable temperature. From the experiment conducted, in fact, at 11:00 a.m. the cavity, after being totally discharged, has already reached 55 °C. Comparing the values obtained with those of a classical system with water storage, the increase in temperature developed during the experiment in the 30/55 °C range was greater. A simulation performed with TRNSYS, starting from similar input data, determined a water temperature increase of 6.2 °C/h in the same temperature range.

For the purpose of this first experimental set, the data sampling time used was equal to 1 minute, since it was not necessary to study very rapid temperature changes. Furthermore, attention was not paid to the waterflow used because its purpose was only to discharge the cavity. Surely, a flow as high as that used is not applicable for the production of DHW.

3.3 No withdrawal studies

the second experimental phase was carried out during the months of July and August, during which no water withdrawal was carried out. This long period of testing has allowed us to study the reliability of the system, which has undergone numerous loading and unloading cycles, even reaching high temperatures. The amount of data collected has also allowed to conduct detailed analyses on some specific components of the system, investigating some parameters that were subsequently used for the development of the mathematical model, such as the heat transfer coefficient of the heat pipes.

Despite being very similar to each other, in the following paragraphs will be shown the results for the month of August, during which the experiments were conducted from the first day of the month until the twenty-second. Figure 3-4 shows the main temperature trends monitored inside the system. The solar irradiance has almost always exceeded 1000 W/m^2 as a peak value every day, except for some cloudier days. The outside temperature instead ranged between 15 and $35 \text{ }^\circ\text{C}$. By shifting the attention on the absorber, a peak value of $102.6 \text{ }^\circ\text{C}$ has been reached, which, although quite high, does not compromise the mechanical integrity of the component. Moving on the cavity, the influence of irradiation is quite visible. In the cloudiest days the temperature drops below $20 \text{ }^\circ\text{C}$. However, in very sunny days, the cavity most of the time exceeds $70 \text{ }^\circ\text{C}$, recording a peak value of about $83 \text{ }^\circ\text{C}$. The sampling time for this series of tests was 10 minutes, since there were no thermal phenomena of a certain speed and the data collection period was rather long.

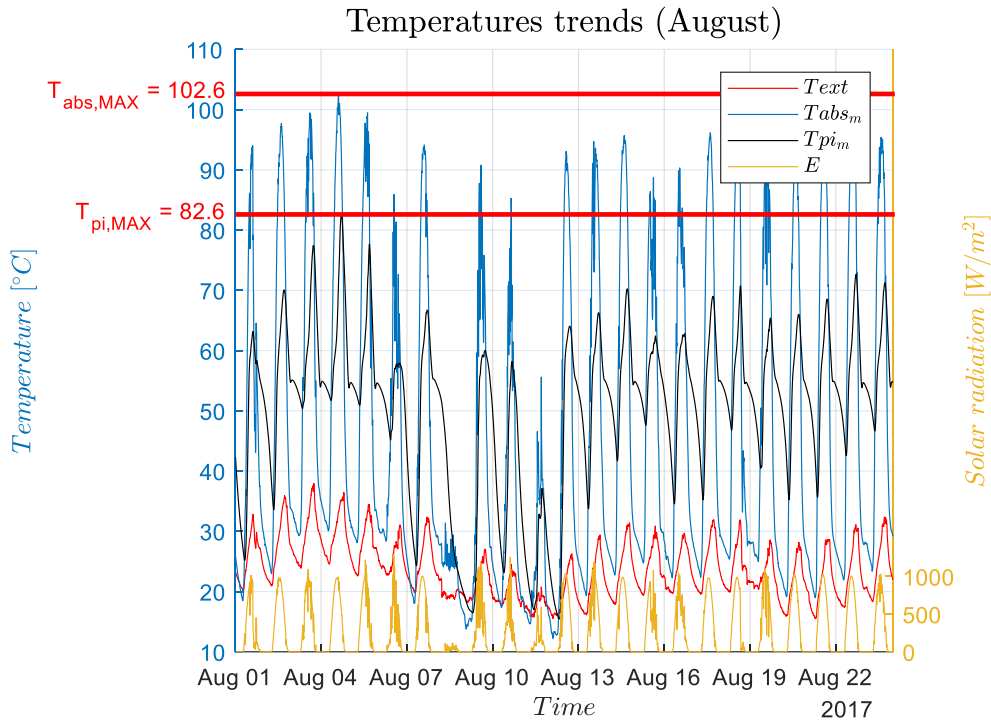


Figure 3-4. Main temperatures trends in August 2017

3.3.1 Thermal diode effect

During this period without water withdrawals it is very easy to identify the behaviour of the heat pipes as thermal diodes. The advantage of using heat pipes as a mean of heat transmission from the absorber to the storage cavity is precisely that of creating a thermodynamic barrier that allows the passage of heat only in one direction, that is from the condenser (in contact with the absorber), to the evaporator (in contact with the storage cavity). This solution allows the passage of heat during the day, when the absorber has a higher temperature of the cavity due to the effect of solar radiation. On the contrary, during the night hours, when the solar irradiation is less, and the temperature of the absorber decreases to become lower than that of the cavity, the thermal flow is interrupted, and consequently the cavity, containing the PCM, is maintained at a higher temperature without losing the stored energy. This thermal diode effect is made possible thanks to the slight inclination of the heat pipes, as presented in the previous chapter. The slope angle (5°) maintains, in effect of gravity, the heat-carrying fluid inside (methanol) in the lower part (condenser), in a liquid phase. The lack of solar radiation during night leads to an interruption of the methanol evaporation process, and therefore to a stoppage of the heat exchange through the heat pipe. Figure 3-5 shows this effect during some days in August. Evaporator and condenser have almost equal temperatures in the

presence of solar radiation, while their temperature gap grows up to 20 °C in the night hours.

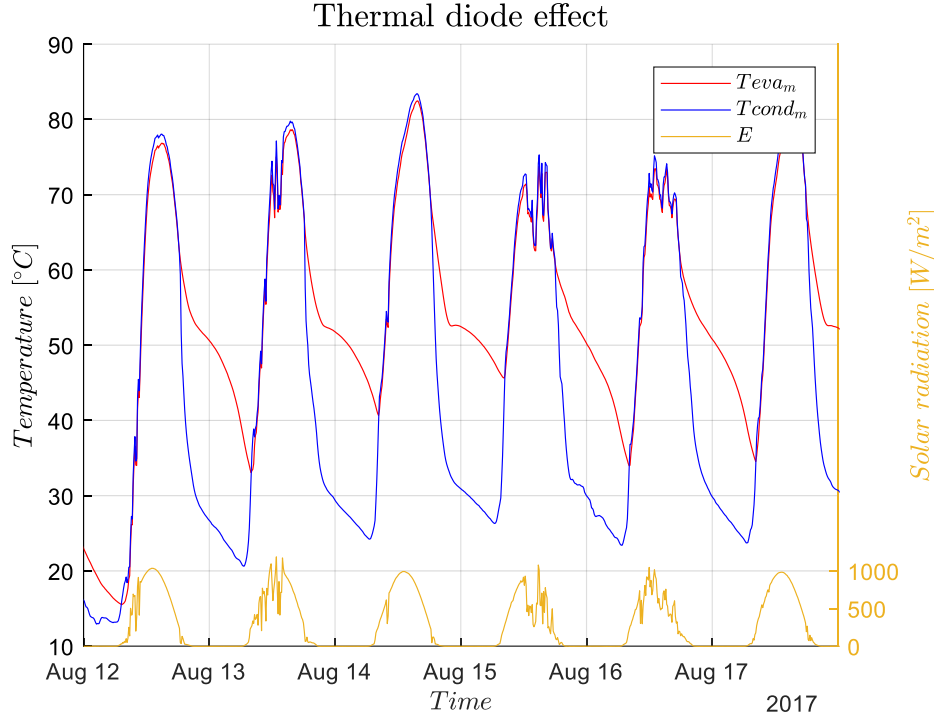


Figure 3-5. Evaporator and condenser temperatures highlighting the thermal diode effect

3.3.2 Heat pipe heat transfer coefficient

The data collected were used to estimate some parameters useful for future evaluations, as well as for the subsequent development of the mathematical model. The first section to be taken into consideration was that of the heat pipes. The thermofluid dynamic process that develops inside the heat pipe can be rather complicated to analyse; for this reason, it was preferred a simpler approach, that does not take into consideration the thermofluid dynamic phenomena in the specific, but consider the phenomenon from a quantitative point of view.

All the heat exchange phenomena occurring within the heat pipe have therefore been incorporated into a single coefficient, which can be defined as the global heat exchange coefficient of the heat pipe. From the literature can be defined as (Nemec, et al., 2011):

$$U_{HP} = \frac{\dot{Q}_{HP}}{T_{eva} - T_{cond}} \left[\frac{W}{^{\circ}C} \right]$$

Where \dot{Q}_{HP} is the thermal power that passes through the heat pipe. The latter can in turn be defined, as regards our system, as the solar power supplied by the sun through the absorber, less thermal losses:

$$\dot{Q}_{HP} = \dot{Q}_{sol} - \dot{Q}_{abs,loss} = E \cdot (\tau\alpha) \cdot A_{abs} - U_L \cdot A_{abs} \cdot (T_{abs} - T_{ext}) [W]$$

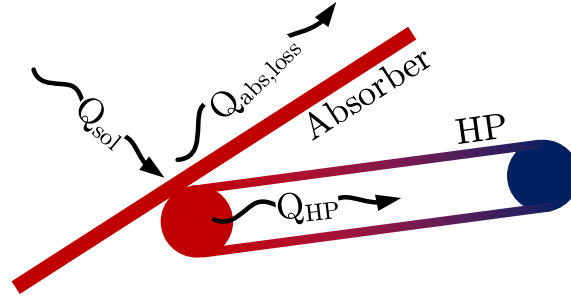


Figure 3-6. Heat fluxes in HP evaporator section

Where τ and α are respectively the coefficients of transmission and absorption of the absorber, while U_L is the coefficient of heat exchange that is established between the absorber and the external environment, taking into account the presence of the glazed surface and the air gap:

$$U_L = \frac{1}{\frac{s_{abs}}{\lambda_{abs}} + \frac{1}{h_r + \frac{h_c}{2}} + \frac{s_{glass}}{\lambda_{glass}} + \frac{1}{h_e}} \left[\frac{W}{m^2 \cdot ^\circ C} \right]$$

Most of these parameters will be addressed and commented later in the modelling phase.

In order to have a correct evaluation of the U_{HP} coefficient, not all the data collected during the experimental phase of August have been used. The selected values have been defined in such a way as to ensure the presence of an adequate heat flow inside the heat pipe. For this reason, the data taken into account were those that met the following conditions:

- $(T_{eva} - T_{cond}) > 4^\circ C$, so as to ensure a minimum flow of heat.
- $E > 0 W/m^2$, so as to discard all the values collected at night time, when the heat pipe is supposed to work as a thermal diode.

The result of this analysis, collected in Figure 3-7, shows how the value of U_{HP} is rather variable depending on the conditions in which the system is working. However, its average value, equal to 1,522 W/K is perfectly in line with what was expected.

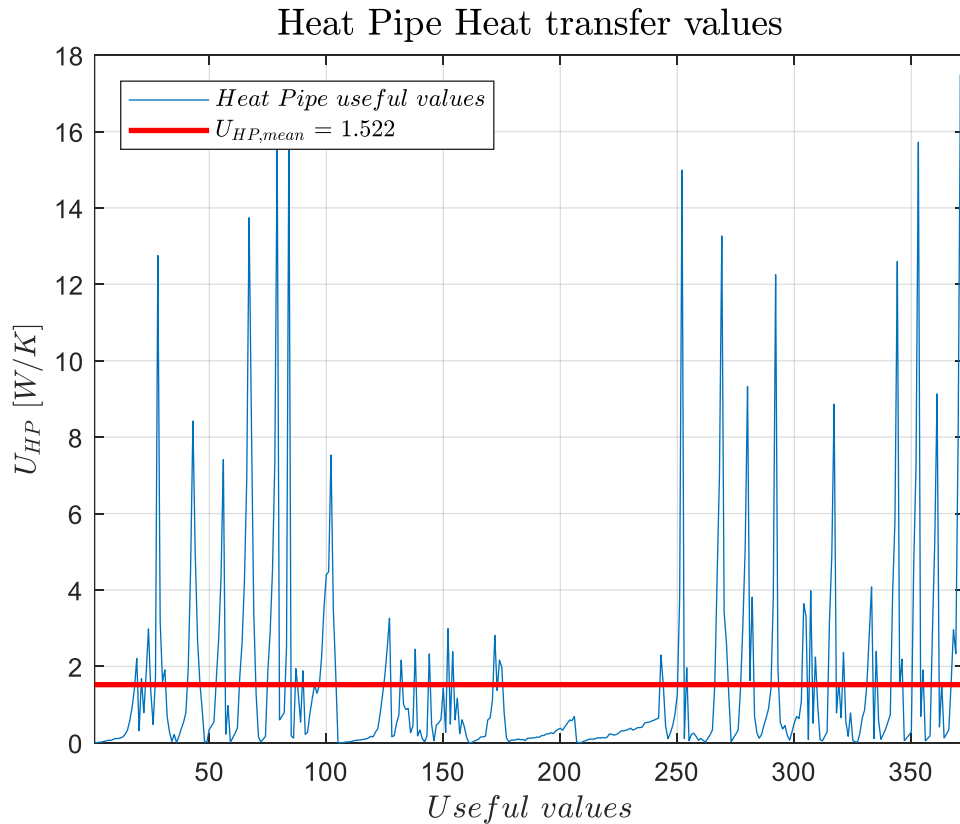


Figure 3-7. Heat pipe heat transfer coefficient evaluation

3.3.3 System efficiency evaluation

Always using the same starting data, some considerations have been made regarding the efficiency of the prototype. Since no DHW withdrawals were performed during this test phase, the useful efficiency in the production of DHW was not evaluated. However, the focus has been shifted to the potential efficiency of the system, which is the ability to take advantage of the solar radiation and then store it inside the PCM.

A preliminary consideration can be made by analysing the average daily value of the useful gains, as previously defined in section 3.1, as a function of the average daily value of the solar contributions from 9 am to 5 pm. The result obtained, shown in Figure 3-8, presents the average values evaluated for all the days of August. A trend line (in red) has been added to the graph, allowing comparison with a similar study conducted by (Robinson, et al., 2013) in which the analysed system was quite similar to the one under examination, as already mentioned in the previous chapter.

The analysis shows a result consistent with what is present in the literature, also highlighting a better behaviour of the prototype studied in cases of poor solar radiation.

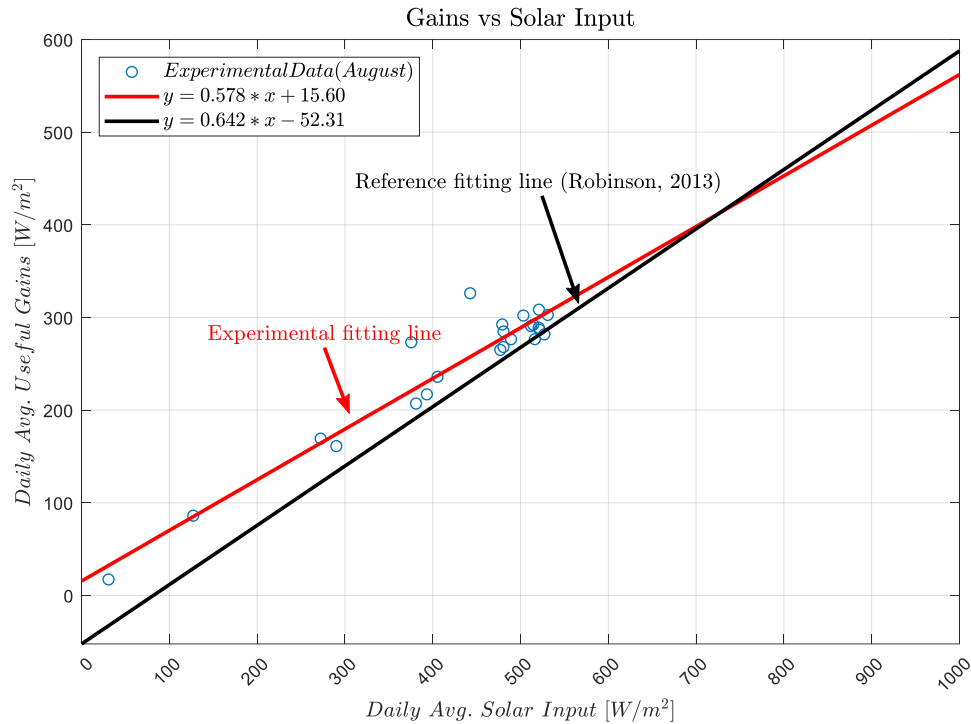


Figure 3-8. Daily average useful gains versus daily average solar input from 9 a.m. to 5 p.m.

The efficiency of the collector was then calculated as the ratio between the useful energy stored in the cavity and the solar energy due to irradiation, according to the following relation:

$$\eta = \frac{\dot{Q}_{sto}}{E \cdot A_{abs}} = \frac{U_{HP} \cdot \#_{HP} \cdot (T_{abs} - T_{pe})}{E \cdot A_{abs}} [-]$$

Also in this case, to obtain comparable results, the average experimental values collected during the central hours of the day were used as starting data, in order to ensure that the following condition was respected:

$$T_{pe} > T_{ext}$$

The average efficiency values for each day were finally collected in Figure 3-9 as a function of the temperature difference between storage and external environment over solar radiation. Each value in the figure (blue circles) represents an experimental day of August.

Also in this case a linear trendline was drawn (solid red line), demonstrating that the system achieves an efficiency of 61.0% when the storage temperature is equal to the external one. As in the previous chart, the fitting line found by (Robinson, et al., 2013) in his study has been reported, showing once again the affinity between the two systems.

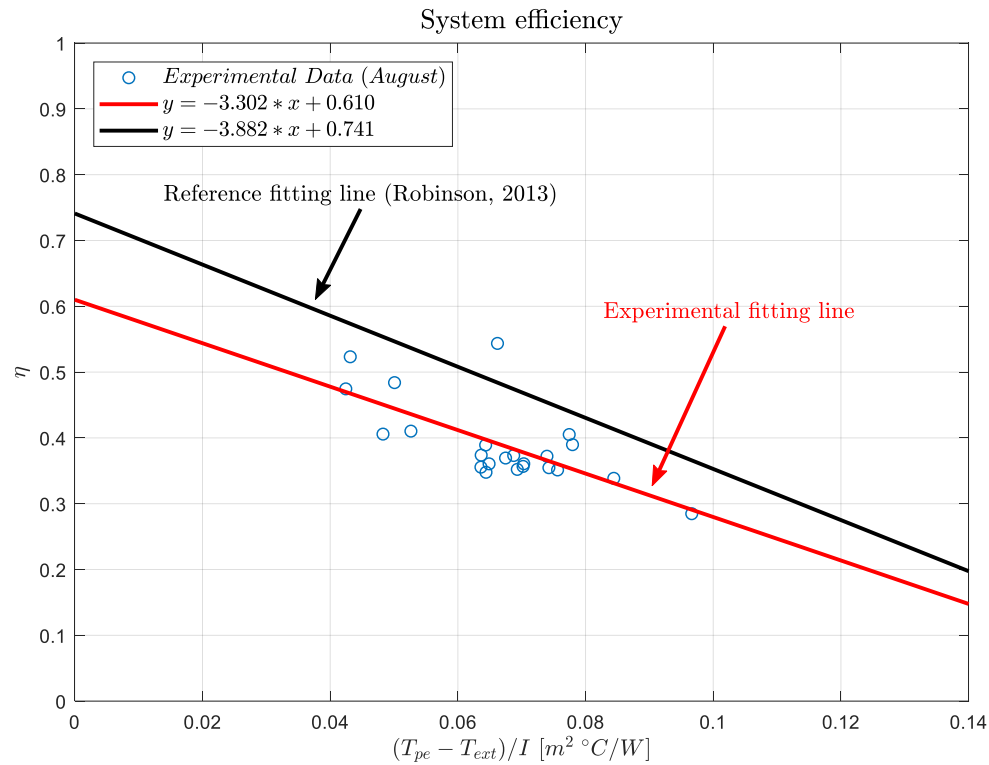


Figure 3-9. System efficiency versus loss potential/insolation ratio

What emerges from this analysis is certainly a poor optical efficiency of the collector, which is rather low compared to similar systems on the market. The glazed surface installed in the prototype, as well as the flat absorber, are in fact standard elements that do not reach particular performance in terms of energy. In this respect the prototype could receive future improvements.

3.3.4 Power loss study

This section analyses what seems to be the most critical problem of the prototype, i.e. thermal losses. Power loss was taken into consideration, by evaluating the energy stored during the month of August and comparing it with the energy lost during the same period. The result is collected in Figure 3-10, where both the energy lost and stored were expressed in kWh. These two quantities were evaluated by referring to the equations presented in section 3.1 of this chapter, bringing into play two experimental coefficients already presented: in the case of the stored energy (Q_{sto}) the global heat transfer coefficient of the heat pipes was used (U_{HP}), discussed in section 3.3.2. On the other hand, as regards the lost energy, the global convective coefficient (D) has been brought into play. The latter was always obtained experimentally but through a subsequent experimental phase conducted in a laboratory environment, during the month of November. Therefore, the way in which it was

obtained will be explained in the following paragraphs, that follow the experimental timeline.

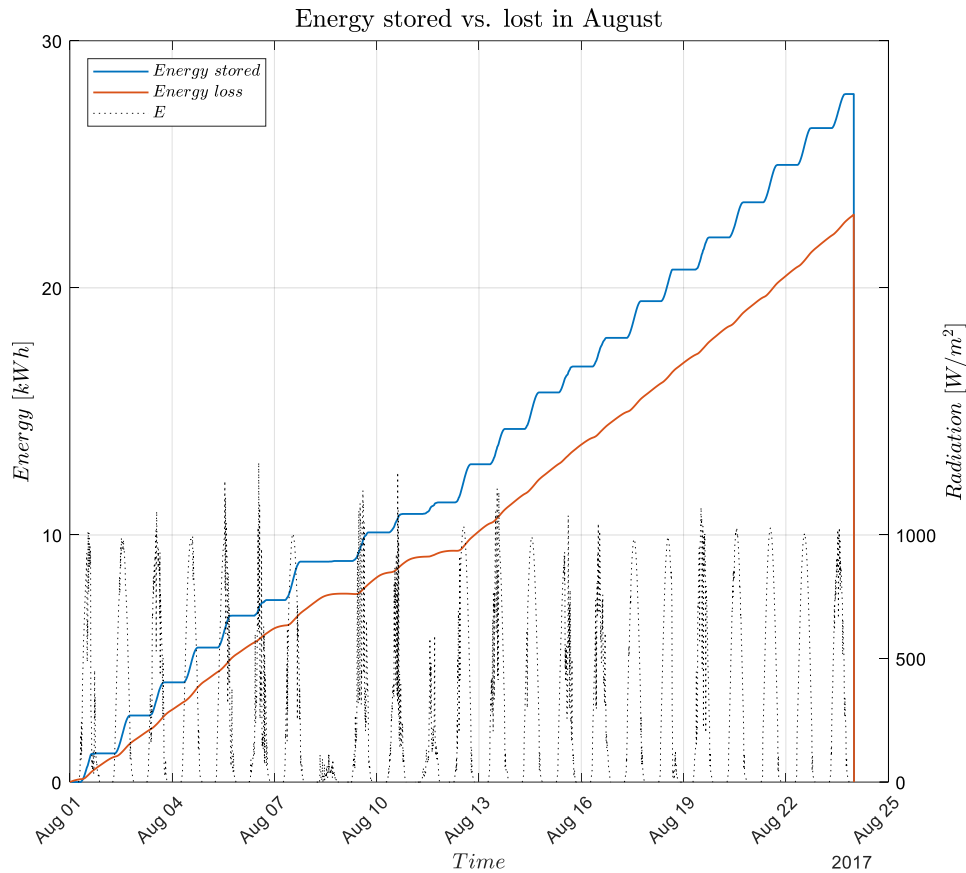


Figure 3-10. Energy stored and energy lost in August 2017

What emerges from the previous graph is a significant impact of thermal losses on the thermal storage capacity of the prototype. As expected, the solar radiation (black dashed line) has a considerable impact on the stored energy, while it does not significantly influence thermal losses, which have a constant linear growth over time.

Finally, the same data have been elaborated in Figure 3-11 to show the trend of the thermal power losses, as the effective power lost. All the values presented are negative, indicating a heat flow dispersed from the system to the environment. On one hand, this behaviour is justified by the fact that the temperature from the storage cavity is always greater than the external temperature (although still in August). On the other hand, however, the calculated values are quite high, recording an average value of 41.626 W, meaning a specific thermal loss of 80 W/m² considering the absorber surface of the collector. These results further confirm a thermal insulation of the system that is not too efficient, causing the loss of an important amount of energy stored.



Figure 3-11. Thermal power loss in August 2017

3.4 Withdrawal study

During the month of September 2017, the prototype phase was studied, simulating on the test bench, always positioned inside the solar field, a water withdrawal. During the 22nd of September two daily withdrawals were scheduled, at 12:00 for a duration of about 15 minutes and at 17:00 for a duration of about 30 minutes. For these experiments it was decided to use a water flow that is suitable for the system's purposes, equal to 0.87 l/min. The purpose of this phase was to investigate the thermal power that the prototype is able to provide to a possible user.

Figure 3-12 shows some days of the month of September, reporting some temperature trends. It is interesting to note that the temperature difference between the front surface of the cavity and the back surface never exceeds 10 ° C, indicating an effective heat exchange inside, by means of the honeycomb structure. Furthermore, the temperature of the front plate (T_{pe}) is higher during the day, thanks to the effect of solar radiation. At night instead, the back plate, dispersing less heat, is at a higher temperature (T_{pi}).

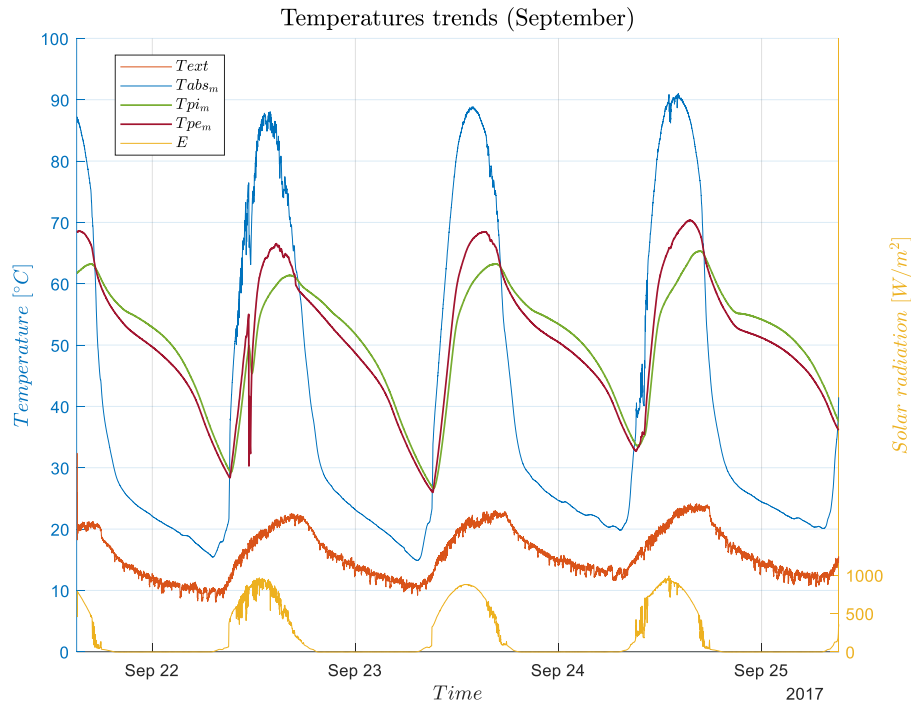


Figure 3-12. Main temperature trends in September 2017

Focusing on the water withdrawals (September 22nd), collected in Figure 3-13, it can be seen the effect of the external water on the cavity, whose temperatures have been shown in the figure. The temperature of the water leaving the exchanger reaches maximum temperatures close to 50 °C, without going below 30 °C for the entire duration of the withdrawal. However, what is interesting is the effect that the withdrawal of water has on the cavity. The first one, carried out at around 12:00, has a significant impact on cavity temperatures, while the second, carried out in the afternoon (17:00), affects the cavity much less. This behaviour can be justified by the fact that at the time of the first withdrawal the cavity, having a temperature slightly above 50 °C, did not have the PCM in total liquid phase and consequently the latent heat accumulated was not exploited. On the contrary, at the time of the second withdrawal, as the cavity was at a temperature above 60 °C, it was possible to exploit the latent heat accumulated in the PCM. It is also easy to see how the front plate of the cavity, being in direct contact with the water heat exchanger, is more affected by temperature variations.

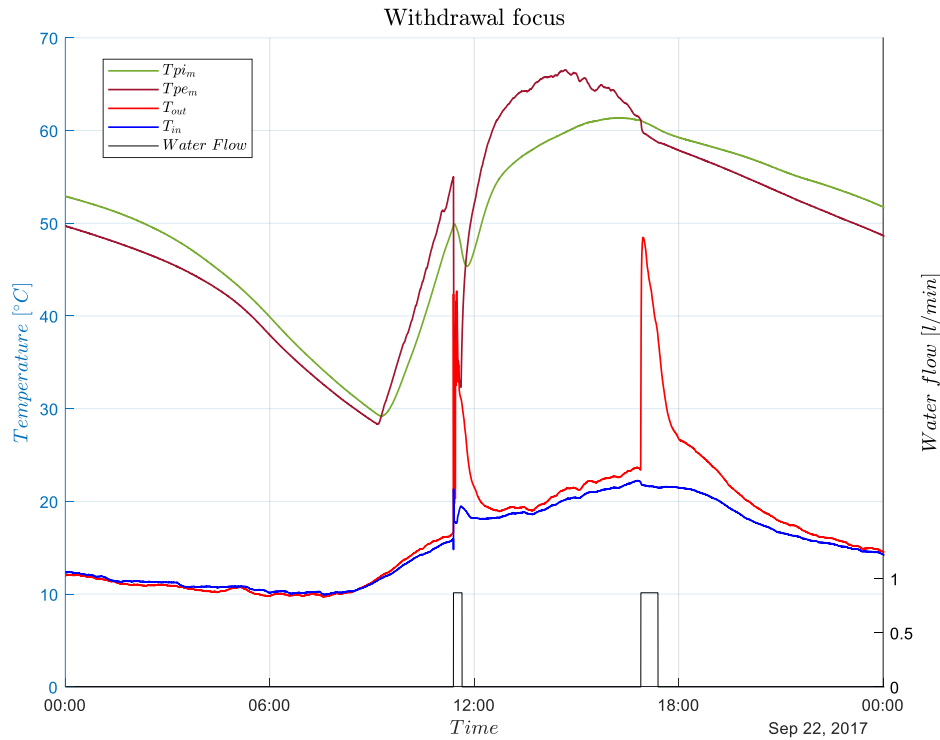


Figure 3-13. Water withdrawals in September 2017

Finally, focusing only on the afternoon sampling, the power extracted from the water during the experiment was evaluated. An average value of 1.32 kW was determined for an absorber surface equal to 0.5 m². Normalizing this result, it can be concluded that the prototype is able to provide a power of about 2.6 kW/m², with a water flow of less than 1 l/min (Figure 3-14). In the light of the results obtained, it can be seen that the heat exchange between the water coil and the front plate of the cavity does not have a high efficiency and could be improved. This explains the rather high temperature difference between the outlet water and the front plate.

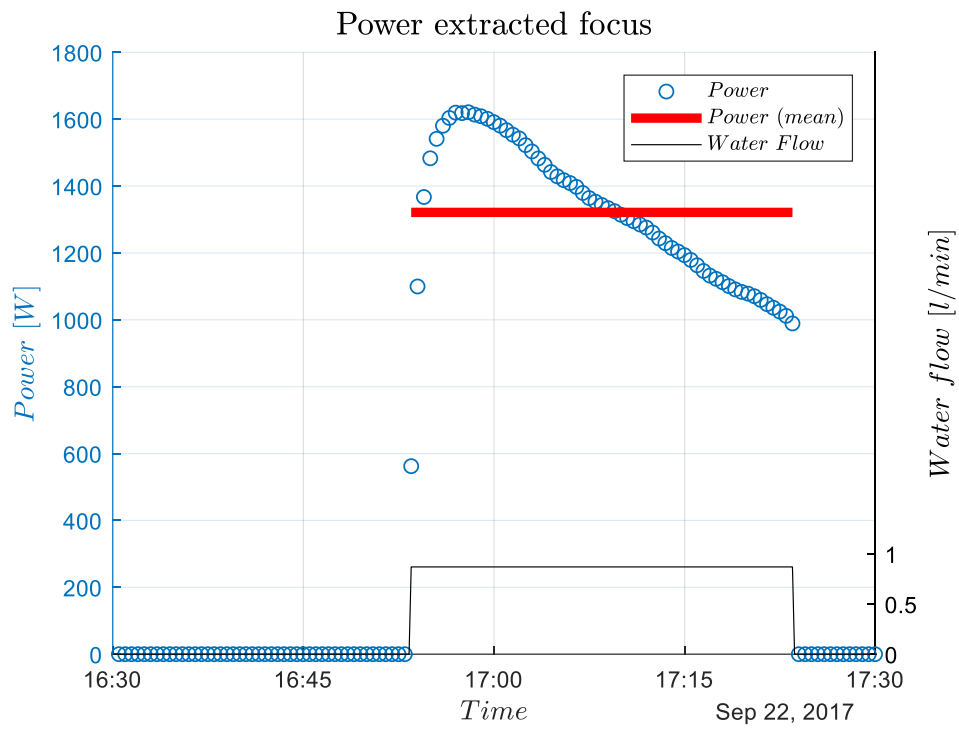


Figure 3-14. Extracted power from water withdrawal

Chapter 4

4 Prototype thermal improvement and advanced analysis

With the end of the summer season, the first part of the experimental phase was also concluded. Given the results obtained, a new series of experimental tests were conducted, no longer focused on the overall functioning of the prototype, but by analysing in detail some of the internal components, in order to better understand what the critical points of the system were. Moreover, this type of analysis has also allowed us to gather useful information for the future development of the mathematical model.

Finally, after completing this second phase, carried out entirely in an indoor laboratory environment, the prototype was again moved outside to study its winter performance.

4.1 Prototype thermal improvement

At the end of the summer period, starting from the month of November, the prototype was moved from the solar field into an internal laboratory environment. This second phase of investigation was more focused on the study of thermal losses, to be able to better understand the rather poor results obtained during the summer tests. The prototype, together with all the equipment for data collection, has been connected to a new external water source, no longer coming from the national water network but from an electric heater. With this new experimental set up, shown in Figure 4-1, an external hot water loop was created and hot water was forced to flow into the prototype DHW exchanger in order to artificially “charge” the storage cavity and increase the PCM temperature until a value of about 60 °C, reaching the totally liquid phase.

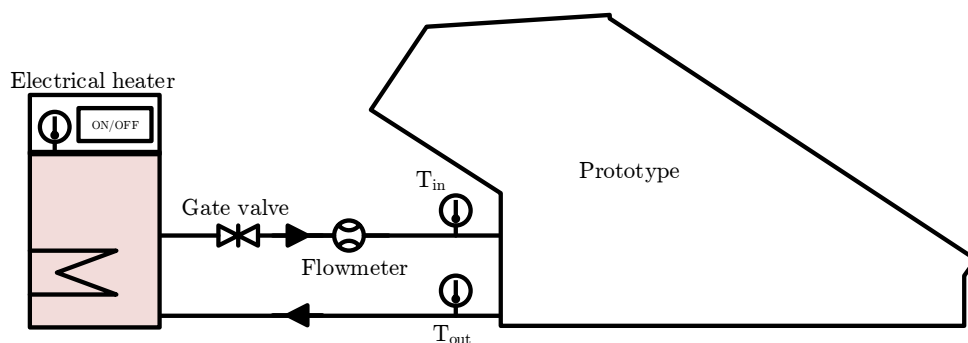


Figure 4-1. Laboratory experimental setup with external heater

Once the desired temperature has been reached, the prototype has been left free to cool naturally, exchanging heat with the surrounding environment, which in this case was the laboratory room, kept at a constant temperature around 20

°C. The decreasing trend of the storage cavity temperatures is shown in Figure 4-2 for both T_{pe} (front cavity plate) and T_{pi} (back cavity plate).

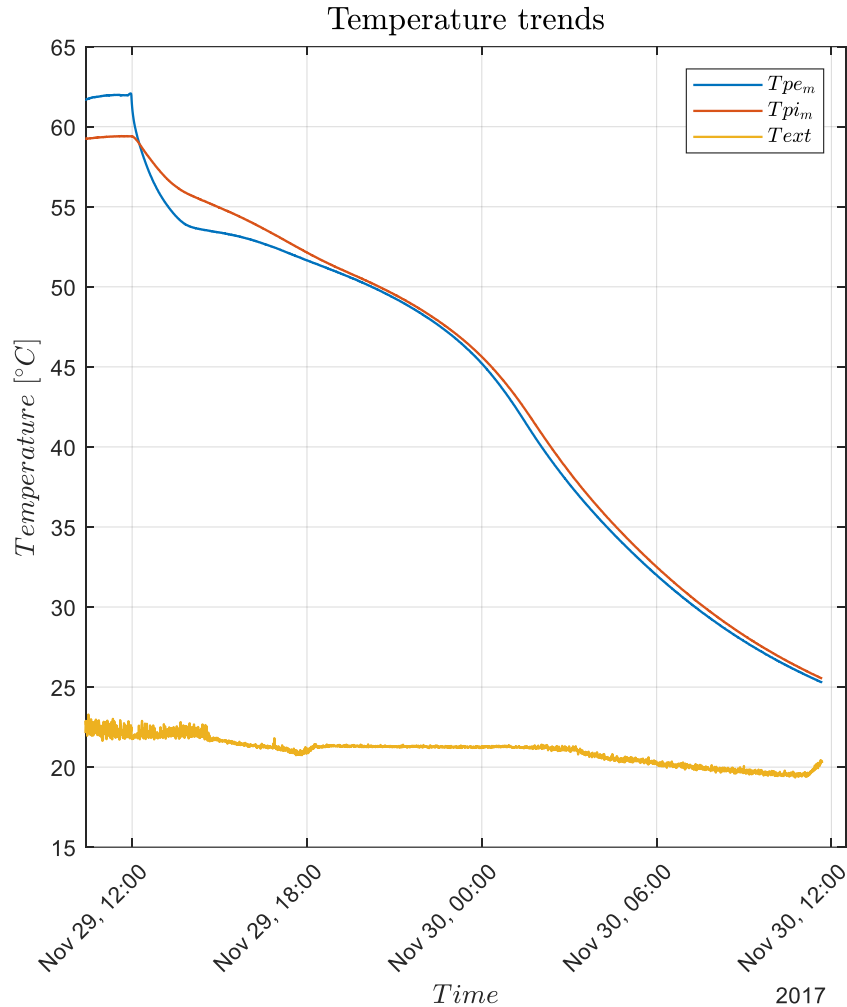


Figure 4-2. T_{pe} and T_{pi} temperature trends during natural cooling

As can be seen from the figure, the cavity has been heated up to 60 °C. The cooling process, which was interrupted when the temperature reached 25 °C, clearly highlights the three states of the phase change material: liquid phase, transition phase, and solid phase. The solid yellow line instead represents the external temperature, which in this case is the laboratory room temperature. After collecting these data, the liquid and solid phases were isolated and studied separately. Applying Newton's cooling law, fitting curves were obtained for experimental data in the liquid phase (above 54 °C) and solid phase (below 46 °C), according to the differential equation:

$$\frac{dT}{dt} = -\tau \cdot (T - T_a)$$

$$T(0) = T_0$$

Solution:

$$T(t) = T_a + (T_0 - T_a) \cdot e^{-\tau t}$$

Where T_0 is the initial temperature of the cavity and T_a is the temperature of the external environment. τ instead represents the time constant of the system, which can also be expressed as:

$$\tau = \frac{C}{D} \left[\frac{1}{s} \right]$$

Where C is the thermal capacity of the PCM inside the cavity, whose value, provided by the manufacturer, is equal to 2.3 kJ/kgK, while D , expressed in W/K represents the global heat exchange coefficient between the cavity and the environment. Thanks to this analysis, the coefficient D has been used both for the previous and for the future analyses of the experimental data as the main parameter for quantitatively estimating the heat losses of the system, as had already been anticipated in section 3.3.4. Fitting curves, together with experimental data are collected in Figure 4-3.

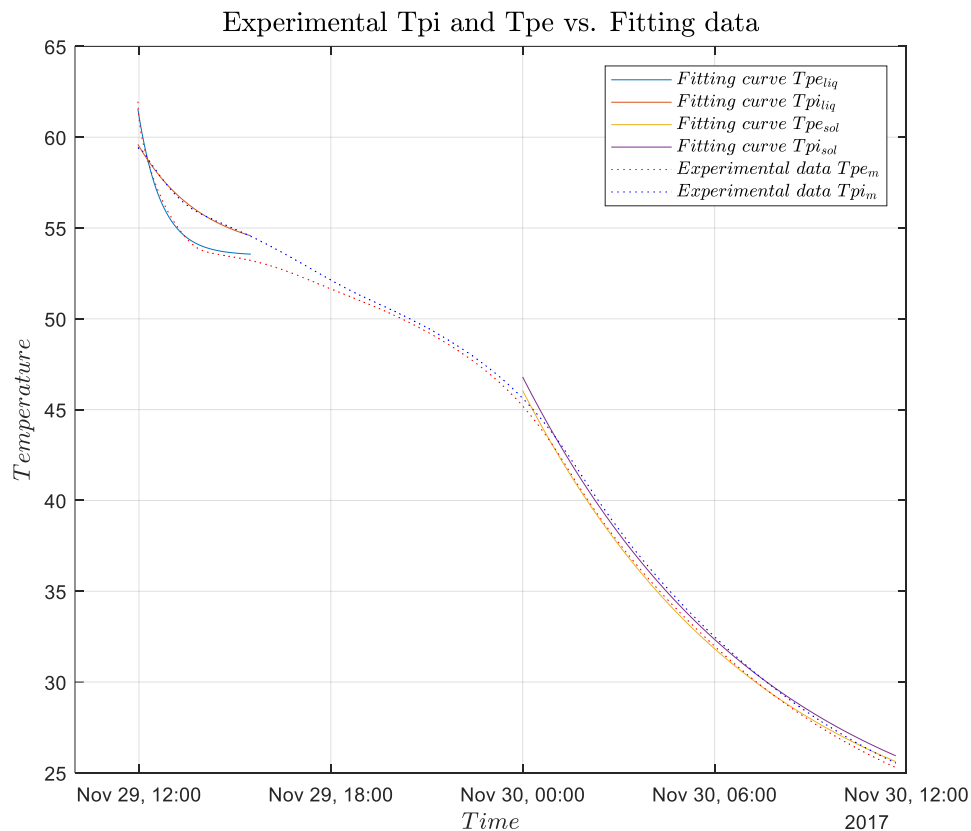


Figure 4-3. Exponential fitting for T_{pe} and T_{pi} temperature trends

Although each section analysed gave a slightly different global exchange coefficient, the average value was 1.51 W/K. Furthermore, it is interesting to

note that the total cooling time from a temperature of about 60 °C to 25 °C was approximately 24 hours.

4.1.1 Casing improvements

Having now established with certainty some shortcomings in terms of thermal losses of the prototype, it has been tried to investigate their primary source. For this purpose, the prototype was charged again using the hot water source, bringing the storage cavity to a temperature of about 70 °C. Once the storage is established on that temperature, a thermographic analysis was performed thanks to the use of a thermal camera. In this way, some “weak points” of the system have been identified. These points, being at higher temperatures, were responsible for most of the thermal losses. As can be seen from the Figure 4-4, Figure 4-5 and Figure 4-6, while the storage cavity was at a temperature of around 70 °C, some elements on the outer surface of the envelope reached almost 50 °C.

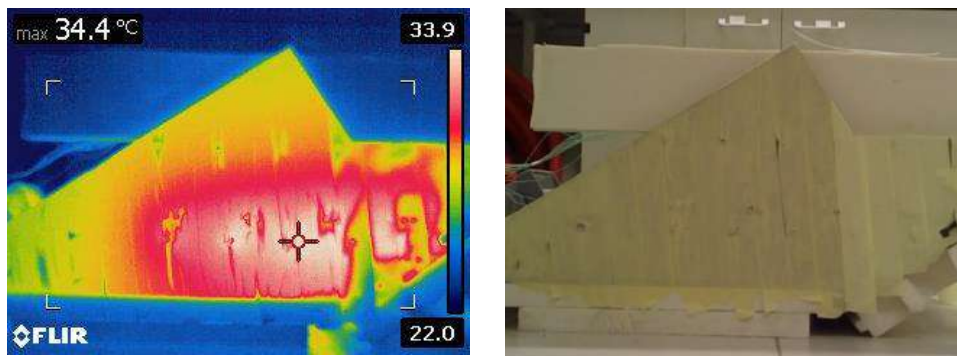


Figure 4-4. Thermal (left) and real (right) picture. Side view

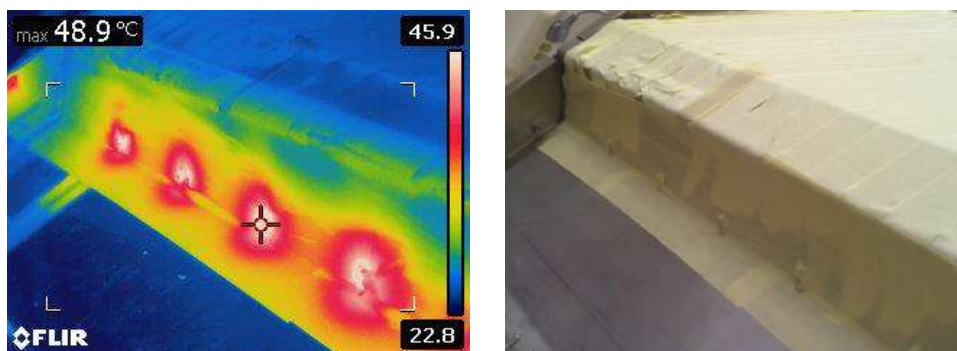


Figure 4-5. Thermal (left) and real (right) picture. Bottom view

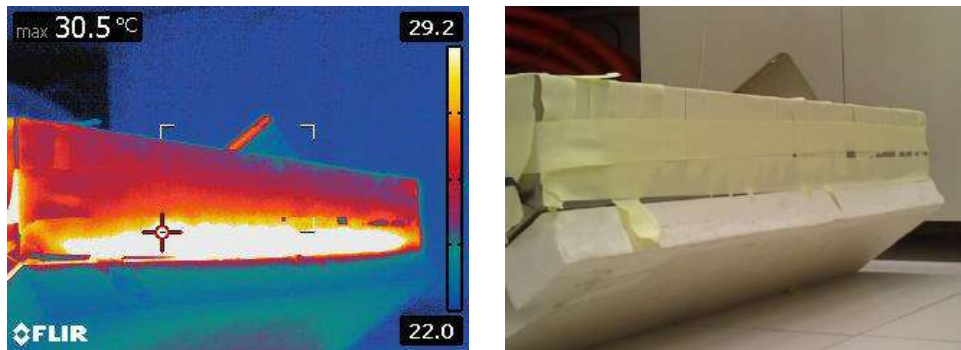


Figure 4-6. Thermal (left) and real (right) picture. Top view

It was therefore simple to verify that these “hot spots” of the system were in the presence of the support elements of the cavity (screws, bolts, etc.) which, having been made of aluminium, created a direct connection between the internal cavity and the outer casing, dispersing a considerable amount of thermal energy.

Based on this analysis, the outer casing of the prototype was opened to make some structural changes by acting on the dispersing elements just identified. The internal structure in charge of supporting the cavity is in fact formed by four metal bars positioned on the back of the cavity, by 5 aluminium spacers on each short side and by 7 metallic junctions positioned on the upper part (Figure 4-7, Figure 4-8 and Figure 4-9).



Figure 4-7. Metallic support bars on the back of the cavity



Figure 4-8. Cavity back plate with thermocouples



Figure 4-9. Metallic joints supporting the cavity on its sides

After making some structural considerations, it was decided to remove all the structural elements in aluminium to replace them with wooden elements, thus limiting heat loss. In addition, the rear support bars have been reduced from 4 to 2, while the metal joints on the upper part from 7 to 3. The new structural elements have been made starting from the old ones. The production of the new elements took place entirely within the experimental laboratory. The various stages of production and subsequent installation have been documented in the

Figure 4-10 and Figure 4-11. The Figure 4-12 represents the installation of the new components inside the casing.

At the end of this process, additional rock wool was added to ensure the insulating properties of the prototype. After that, the casing was closed again to be subjected to further tests.



Figure 4-10. Old metal bar (top) versus new wooden bar (bottom)

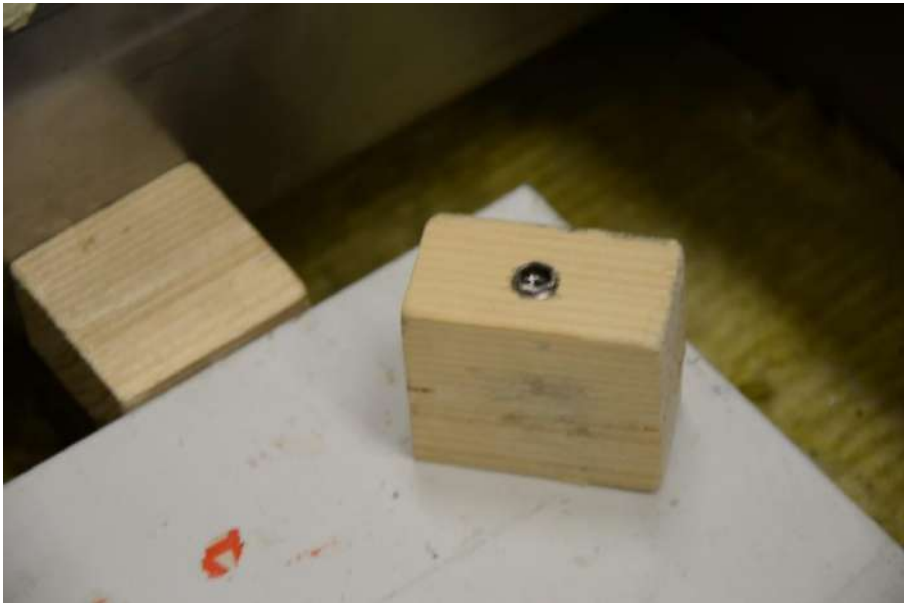
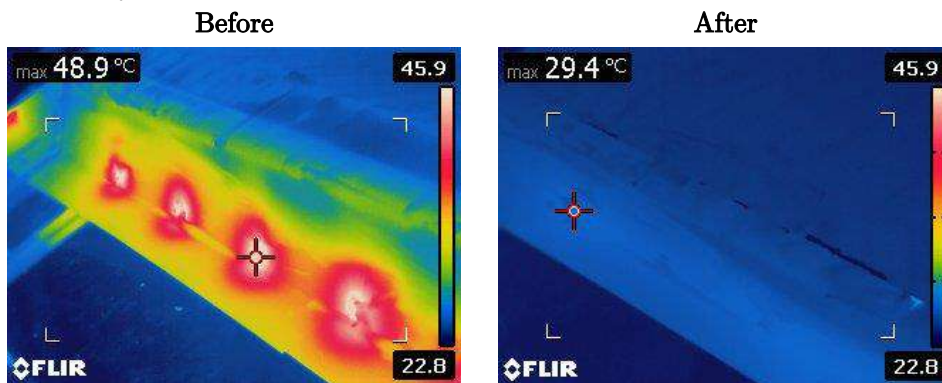


Figure 4-11. New wooden joints supporting the cavity sides



Figure 4-12. Wooden support parts installation

To verify the effectiveness of the changes made, the thermographic analysis was again carried out on the prototype, with the same previous procedures. The cavity was brought to the temperature of 70 °C and the dispersions were analysed with the thermal camera. The results between the previous analysis and the new one were collected in the following figures, where the casing elements on which the modifications were made have been visually compared. The temperature scale used in the thermal images was the same, so as to compare the results consistently.



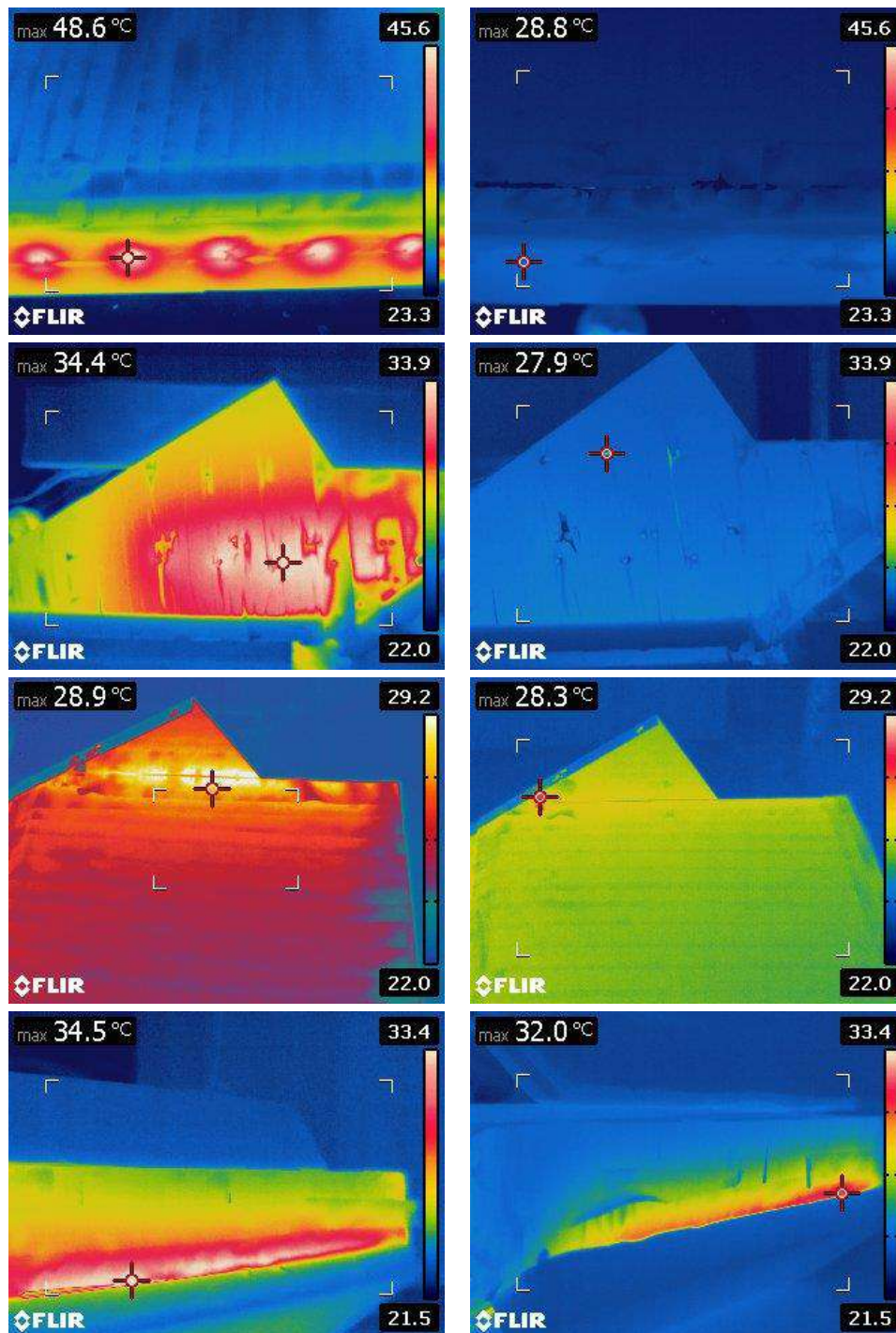


Figure 4-13. Different thermographic comparisons between old support structure (left column) and new wooden structure (right column)

What is evident is a substantial reduction in the external surface temperature, thus leading to a drastic reduction in thermal losses. To verify numerically what is expected, the temperature trend of the storage cavity has

been studied again. As already explained at the beginning of this section, the prototype has been brought up to a temperature around 60 °C and then its natural cooling towards the ambient temperature (about 21 °C) was studied, reproducing similar conditions to the previous experiment. Figure 4-14 shows the trend of T_{pe} and T_{pi} , along with the external temperature for the duration of this new experiment.

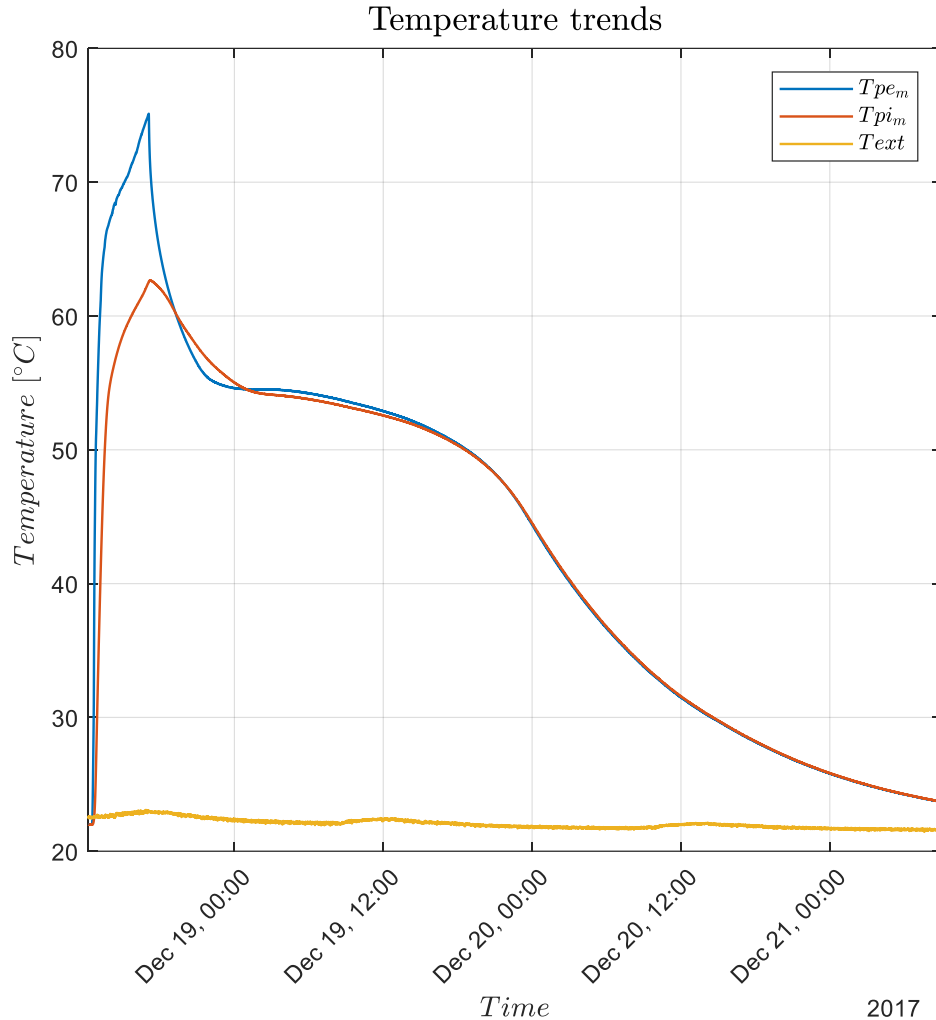


Figure 4-14. T_{pe} and T_{pi} temperature trends during natural cooling (improved prototype)

What is immediately evident is the transition phase from liquid to solid. Compared to the previous case, the phase change zone is more marked and evident. Since having less heat loss, the cavity maintains a constant temperature longer. Furthermore, by focusing on the duration of the experiment, it can be seen that in this case the final temperature (always around 25 °C) is reached

after more than three days, tripling the time it was necessary to reach the same temperature in the previous conditions.

Again, the experimental curves were fitted with an exponential relationship, following Newton's law of cooling (Figure 4-15). With the same procedure, a mean global heat exchange coefficient was computed (D), finding a value of 0.84 W/K, almost halving the previous value.

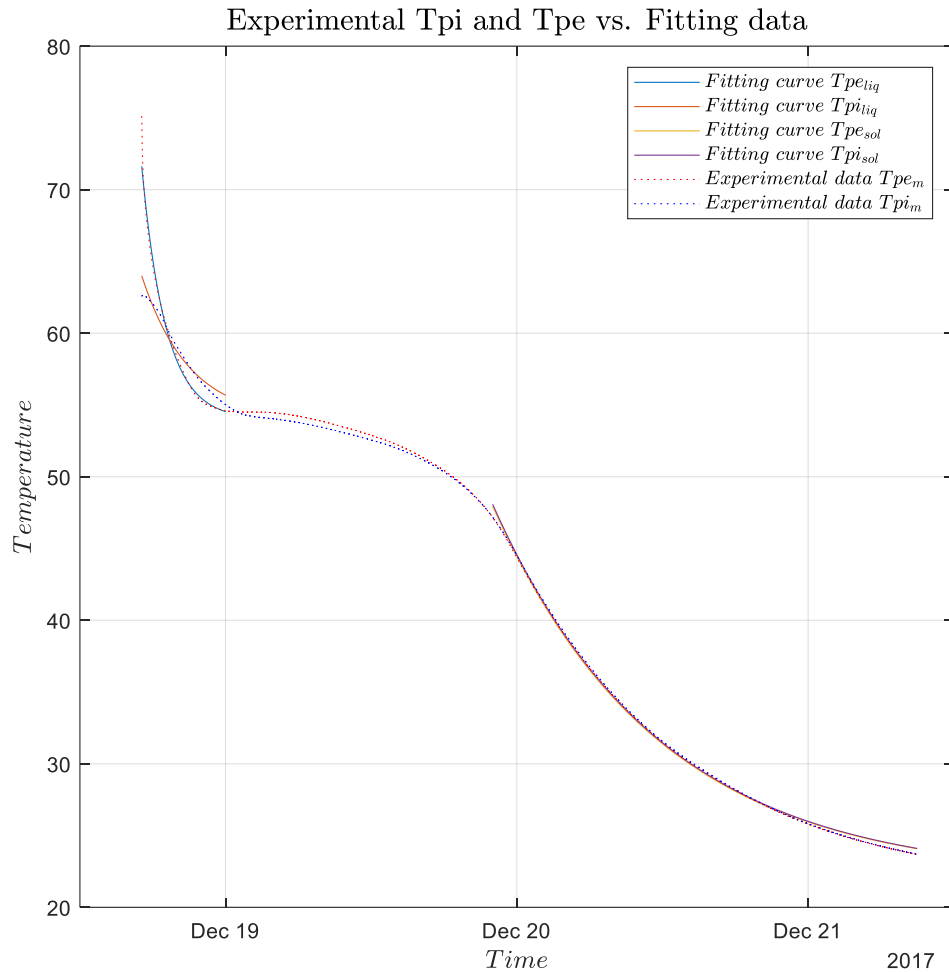


Figure 4-15. Exponential fitting for T_{pe} and T_{pi} temperature trends (improved prototype)

Finally, the trends of the two experiments were compared in Figure 4-16 using the same time scale on the x axis. From the image it can be seen very clearly how the latent heat stored in the phase change phase was difficult to use in the old case, since the thermal losses cancelled the effect. On the other hand, the new configuration clearly improves the energy performance of the prototype at isolation level, thus allowing better exploitation of the stored energy.

On a structural level, after having kept the prototype in its natural operation position, no anomaly has been identified.

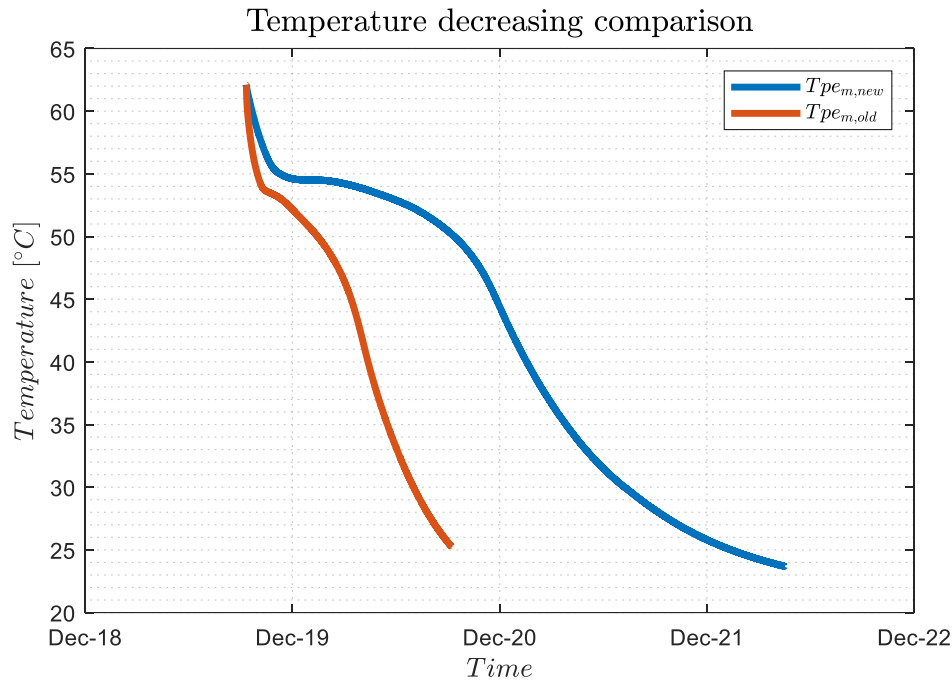


Figure 4-16. Comparison between old and new cooling trend

4.2 DHW exchanger performances

Following the improvements made, a subsequent study focused on the performance of the water heat exchanger with the cavity surface was carried out. The purpose of this analysis was to evaluate the energy performance, as well as some characteristic parameters of the DHW heat exchanger. To achieve this, the same test bench as the previous experiment was used, using the electric water heater to charge the cavity in a fictitious way and increase its temperature. However, this time the charging process was performed more slowly through a very restricted flow of water. Attention was paid to the charging phase, monitoring both the flow of water that flowed inside the exchanger, and the temperatures at the inlet and outlet, as well as the temperature of the cavity. From the trend of these temperatures, collected in Figure 4-17, it has been possible to estimate some characteristic parameters of the installed exchanger.

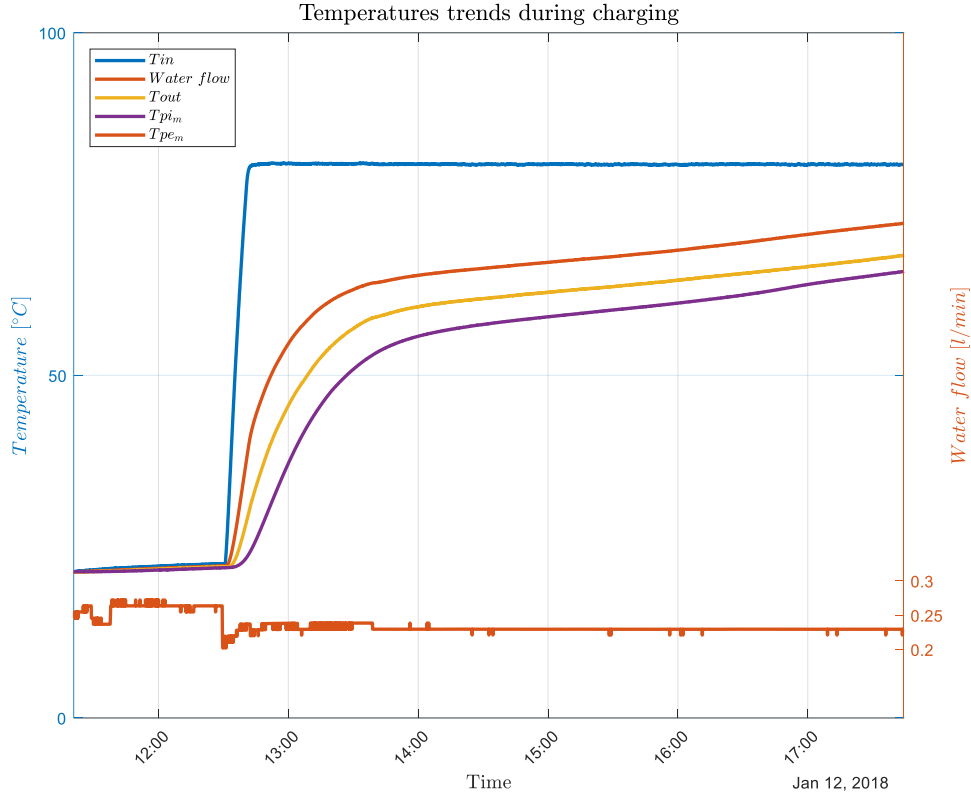


Figure 4-17. Laboratory charging phase (temperatures trends)

Furthermore, by implementing the previous analysis regarding thermal losses, it was possible to estimate the power lost during the cavity charge process by means of the coefficient D , developing the following relation:

$$\dot{Q}_{loss} = D \cdot (T_{pe,m} - T_{ext}) [W]$$

The total available power transmitted by the waterflow to the cavity is instead estimated with the relation:

$$\dot{Q}_w = \dot{m}_w \cdot c_{p,w} \cdot (T_{in} - T_{out}) [W]$$

Where \dot{m}_w is the flow of water, $c_{p,w}$ is the water specific heat, while T_{in} and T_{out} are the temperatures at the inlet and at the outlet of the exchanger.

By setting a simple balance it is possible to evaluate the energy stored in the system, as shown in Figure 4-18.

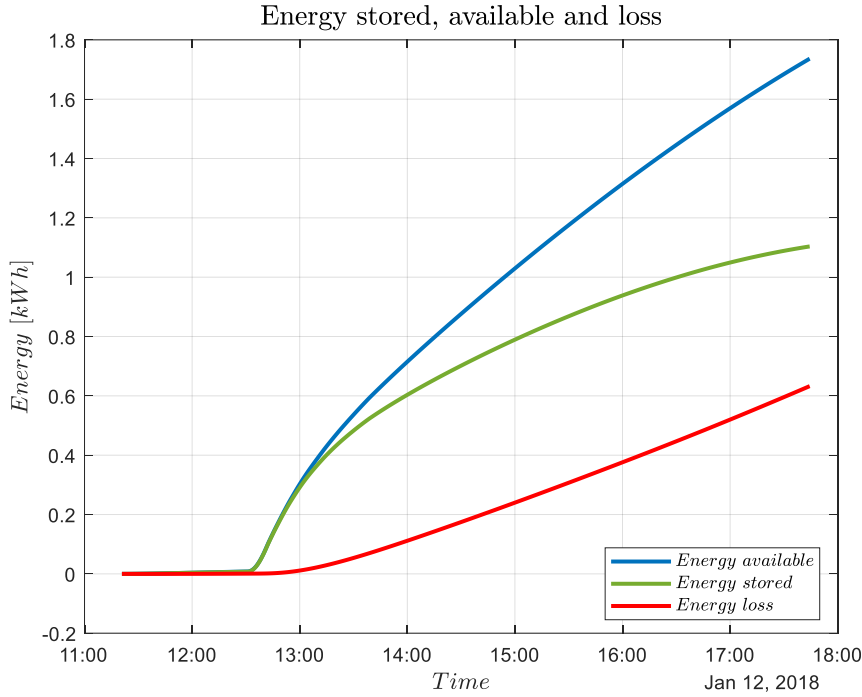


Figure 4-18. Stored, available and lost energy during charging process

The examined heat exchanger is not part of any conventional fluid exchangers groups since the heat exchange process occurs between the waterflow on one side and the aluminium cavity plate on the other side. For this reason, it is necessary to define the characteristic parameters that are closest to the traditional calculation methods, so to have reasonable data that can be compared with other solution in the market.

A first parameter useful to characterize the exchanger is the global exchange coefficient, which has been experimentally determined by means of the relation:

$$U_{HX} = \frac{\dot{Q}_{stored}}{A_{HX} \cdot \Delta T_{ML}} \left[\frac{W}{m^2 K} \right]$$

Where \dot{Q}_{stored} is the stored power, A_{HX} is the total exchange surface and ΔT_{ML} is the logarithmic temperature difference, which in this specific case has been defined as:

$$\Delta T_{ML} = \frac{(T_{w,in} - T_{pe}) - (T_{w,out} - T_{pe})}{\ln \left(\frac{T_{w,in} - T_{pe}}{T_{pe} - T_{w,out}} \right)} [K]$$

Subsequently, the effectiveness of the heat exchange was taken into consideration, defined as the ratio between the actual energy stored and the total available energy:

$$\varepsilon = \frac{\text{Actual heat transfer}}{\text{Maximum possible heat transfer}} = \frac{\dot{Q}_{stored}}{\dot{Q}_{water}} [-]$$

Finally, the efficiency of the exchanger has also been calculated as the ratio between the following temperature drops:

$$\eta = \frac{T_{pe} - T_{w,out}}{T_{w,in} - T_{w,out}} [-]$$

All the above parameters have been processed starting from the experimental data shown in Figure 4-17. The results obtained are instead collected in the Figure 4-19 figure as a function of the time during which the experiment was conducted, consistently with the previous figures.

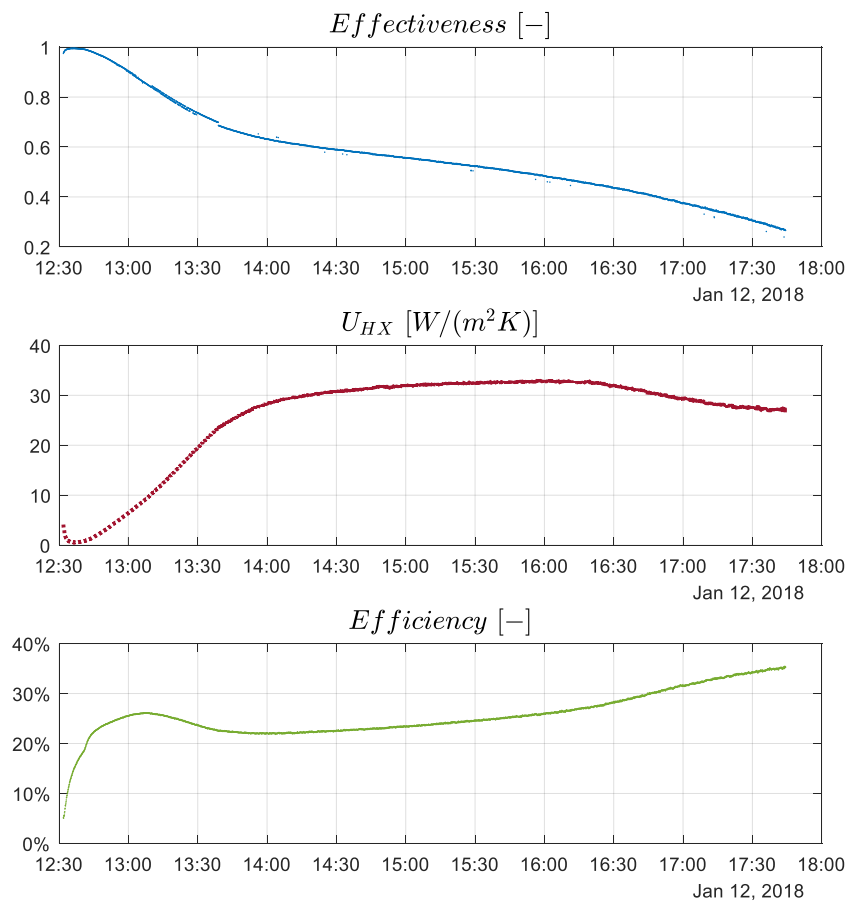


Figure 4-19. Experimental effectiveness, heat transfer coefficient and efficiency for the DHW heat exchanger

From the image it is clear how the effectiveness of the exchange is greater in the initial part of the experiment, when the difference in temperature between water flow and cavity is high. It subsequently decreases as the two temperatures approach, settling around a value of 0.5. Regarding the global exchange coefficient, by excluding the initial transitory regime of the experiment, we can estimate that its value is around 30 W/m²K. Finally, the efficiency of the

exchanger varies between 20% and 40%, increasing when the difference between water flow and storage becomes smaller.

4.3 PCM performance: DSC analysis

In order to better understand the physical behaviour of the phase change material, during the month of February 2018 specific experiments were conducted to investigate deeply the properties of the PCM. The main problem was represented by the fact that PCM, a polyethylene glycol with an average molecular weight of 6000 g/mol (PEG6000), was supplied by the manufacturer without a very detailed data sheet, especially from the point of view of the thermophysical properties. Since the latter is a phase change material, it presents, as already stated, a region in which both the liquid and the solid phases coexist at the same time. From previous experiments it was also possible to notice how this two-phase region is included in a temperature range of 55 to 62 °C, leading to a behaviour of this PCM similar to that of a peritectic mixture. Furthermore, the manufacturer has provided a constant value of the specific heat of the material, referred only to the complete liquid phase. However, the value of the specific heat, which is fundamental for developing further considerations from the energy point of view, is certainly not constant when the temperature changes, especially when the transition region is crossed. Due to the lack of additional elements useful to characterize the PCM used in the prototype, and in view of the development of a mathematical model capable of simulating its behaviour, it was decided to carry out a thermal analysis experiment using the differential scanning calorimetry method (DSC).

The aim of this experimental phase was to study the specific heat trend of PEG6000 according to its temperature. Moreover, with the same method it was possible to investigate the behaviour of the material during both the melting and the crystallization phases.

The DCS method is based on the measurement of the thermal flux difference between a material sample (PEG6000 in our case) and a reference sample (sapphire was used). The two samples are placed inside two chambers arranged in the calorimeter and are then subjected to a pre-scheduled program that controls the variation of their temperature, heating or cooling them in a controlled manner. The sample mass used is very limited, in the order of milligram units. Knowing a priori the thermal properties of the reference sample it is possible to determine those of the analysed material following a specific calculation procedure.

This experimental phase was also conducted entirely within the material properties laboratory in the University of Savoy, Chambéry.

4.3.1 DSC procedure

The experimental apparatus used to conduct the differential calorimetric analysis is the model DSC 2920 produced by TA instruments. The apparatus consists of an insulated chamber with two housings for the sample material to be analysed

and for the reference one. Inside the same chamber there is also a nozzle for the pressurized gas injection used to bring the calorimeter back to the starting conditions. The atmosphere inside the chamber is controlled through the use of inert gases or reagents that allow to raise or lower the temperature. The sample positions are placed on a thermoelectric disk which is able to record the heat flow exchanged with the samples. The latter are in fact positioned above the disc, inside aluminium pans specifically designed by the manufacturer. Two thermocouples, positioned below the capsule housings, have the task of monitoring the sample temperature. Figure 4-20 represents a cross-section view of the calorimeter cell.

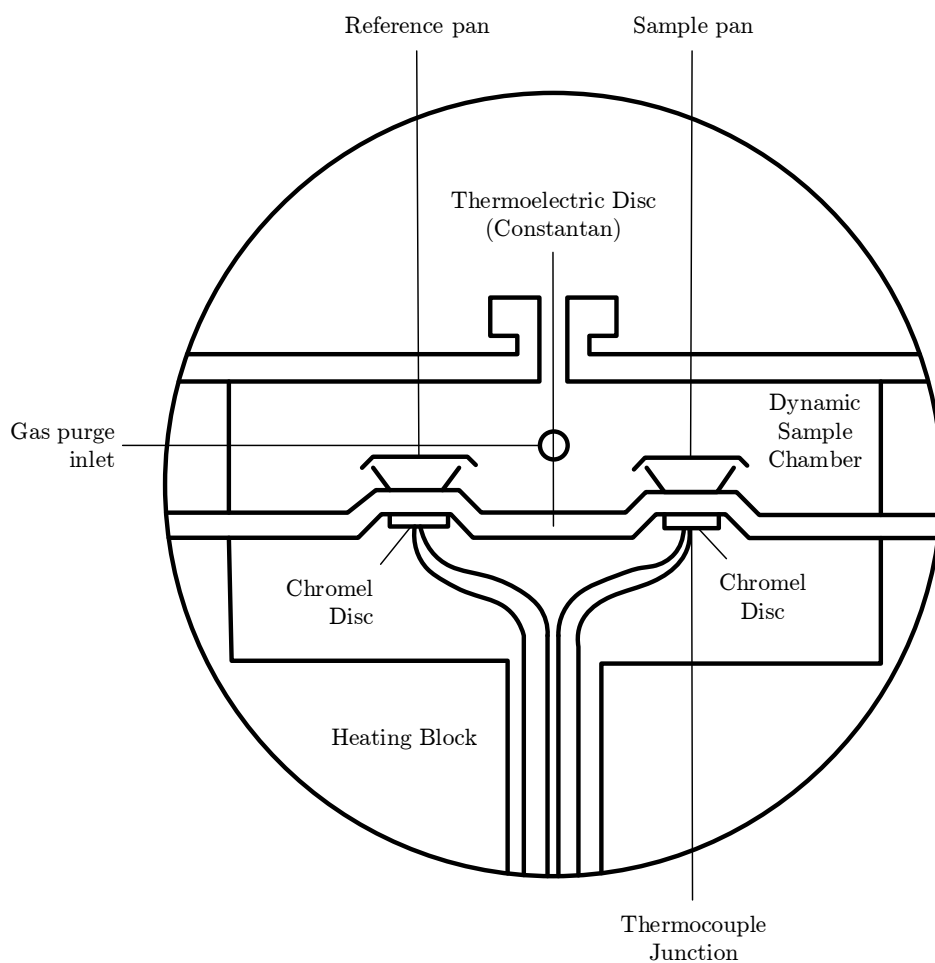


Figure 4-20. DSC Cell Cross-Section (TA Instruments)

The experimental procedure involves several phases, necessitating different elements within the calorimeter:

- A first step consists in the calibration of the instrument, in which a first heating and cooling cycle of the calorimetric chamber is performed with the aim of determining a baseline, on which the subsequent results will

then be calibrated. During this phase only the housing dedicated to the reference sample is occupied by an empty pan.

- In the second phase the heating and cooling cycle is repeated for the reference sample. For the experiment, a sapphire sample weighing 22.3 mg was used, whose thermal properties were provided by the manufacturer. In this phase it is important that the experimental cycle is the same as that of the next phase, which will involve the PCM sample. Both samples must in fact be subjected to the same heating and cooling cycle to obtain consistent results.
- The last phase repeats the procedure of the previous one but with the sample of the material under study inside the calorimetric chamber.

For each of the phases described above, it is necessary to define the individual heating/cooling operations by specifying the desired rate. Also, the isothermal phases, as well as those of temperature equilibration, must be specified a priori through the appropriate software.

The experiment was conducted using a PEG 6000 sample weighing only 5.9 mg. The temperature limits have been set at 20 °C (lower limit) and 90 °C (upper limit), since the material considered rarely exceeds these values in the real operation phase. The heating and cooling rate has been set to 1 °C/min, in order to simulate the real behaviour of the PCM when it is inside the cavity. A lower heating and cooling rate would have been necessary, since in real operation the cavity undergoes even lower temperature variations, of the order of 0.1 °C/min. However, due to the availability needs of experimental material, a greater rate has been adopted. For each phase of the experiment, the output produced by the appliance is the instantaneous value of the heat flow absorbed or released from the sample, expressed in mW, depending on the temperature. The raw data, collected in Figure 4-21 and Figure 4-22, show exactly the flow exchanged by the sample of sapphire (Figure 4-21) and that of PEG 6000 (Figure 4-22) in relation to that calibrated on the empty capsule. A negative flow indicates a flow absorbed by the sample (heating phase), while a positive flow indicates that it has been released from the sample (cooling phase). While there is a rather constant trend in the case of the reference sample (sapphire), the behaviour of the PEG 6000 sample is completely different in the zones where the phase change takes place, during which the heat flow absorbed or released intensifies particularly.

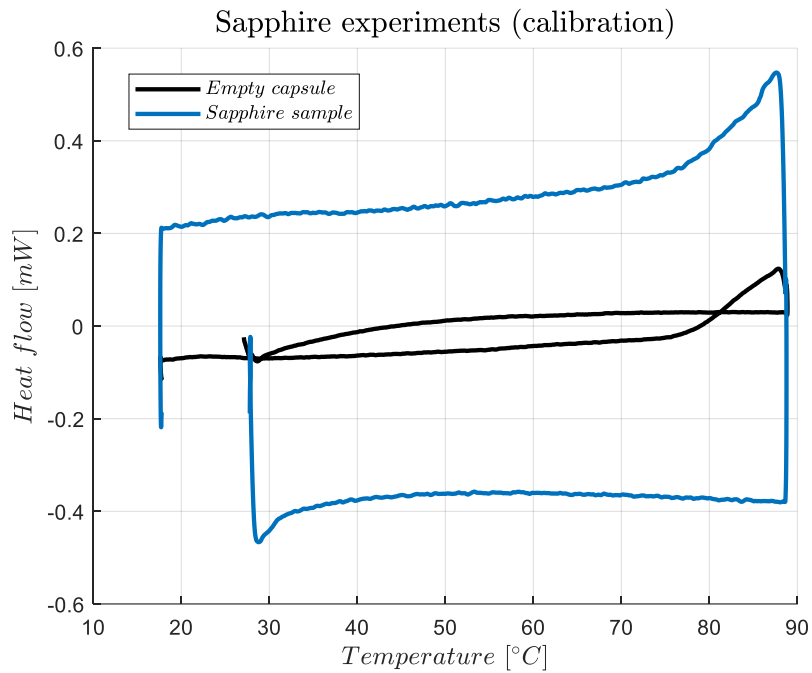


Figure 4-21. Heat flow vs. Temperature for a sapphire sample (DSC method)

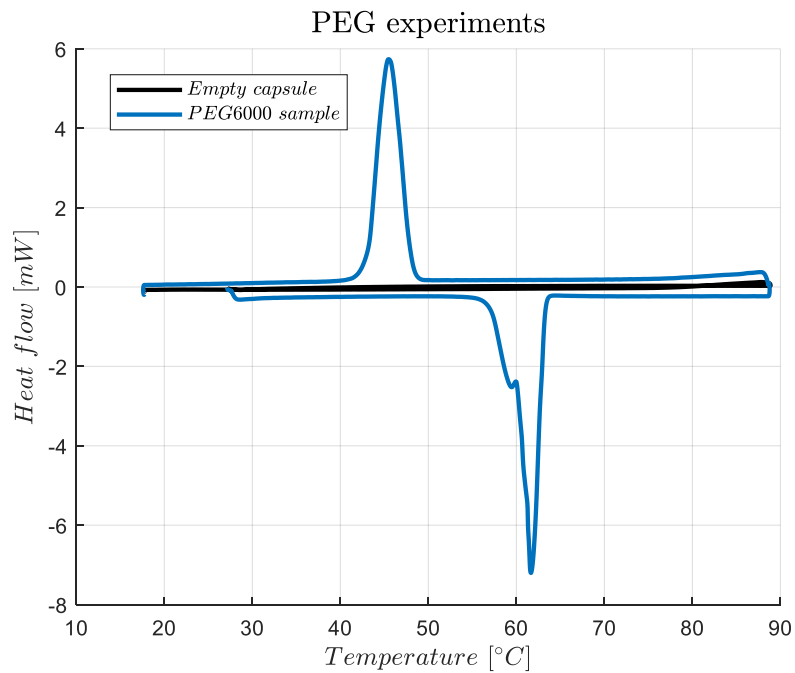


Figure 4-22. Heat flow vs. Temperature for a PEG 6000 sample (DSC method)

For the sake of clarity, the procedures applied to the PEG6000 sample experiment were as follows:

- 1) Temperature equilibration at 30 °C.

- 2) Isotherm condition for 5 minutes.
- 3) Ramp 1 °C/min up to 90 °C.
- 4) Isotherm condition for 2 minutes.
- 5) Ramp 1 °C/min down to 20 °C.
- 6) Isotherm condition for 5 minutes.

4.3.2 Data elaboration and analysis

After collecting the raw data, i.e. the heat flow absorbed or released as a function of temperature, both for the reference sample and for the PEG6000 sample, these have been processed to obtain the value of the specific heat, always according to the temperature, through the following equation (Instruments, 1998):

$$C_p = \left[\frac{60 \cdot E}{H_r} \right] \cdot \frac{\Delta H}{m} \left[\frac{J}{g \cdot ^\circ C} \right]$$

Where:

- E = cell calibration coefficient at the temperature of interest (dimensionless)
- H_r = heating rate, in °C/minute;
- ΔH = difference in y-axis deflection between sample and blank curves at the temperature of interest, in mW;
- m = sample mass, in mg;
- C_p = specific heat, in J/g°C.

The value of the E coefficient is constant for a whole set of experiments that fall under the same conditions. Its value depends on the temperature and allows to convert the heat flow (mW) into specific heat. The value of this constant does not depend on the sample used, as long as it is subjected to the same experimental conditions. For this reason, the value of the constant E was determined starting from the experimental data collected for the sapphire sample, of which the specific heat was already known. Figure 4-23 depicts the behaviour of the specific heat of the sapphire as a function of temperature, determined by (Ditmars, et al., 1982) of the National Bureau of Standards. Highlighted in red the values used for the purposes of our experiment, between the temperatures of 20 and 90 °C, can be seen.

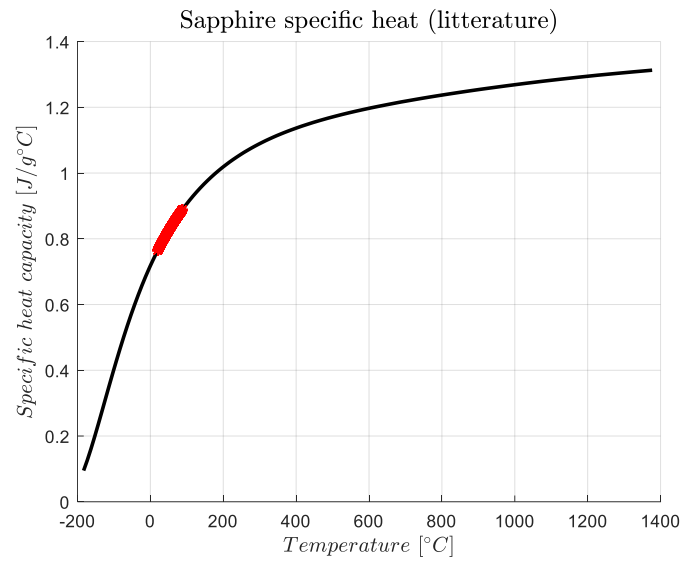


Figure 4-23. Sapphire specific heat by (Ditmars, et al., 1982)

Once the value of E has been determined, the previous relation has been applied to the values found by the calorimetric analysis of the PEG6000 sample, thus determining its specific heat. Both the data related to the heating phase, in which the material melts, and the ones related to the cooling phase, in which the material crystallizes, are collected in Figure 4-24 respectively in the red and blue solid lines.

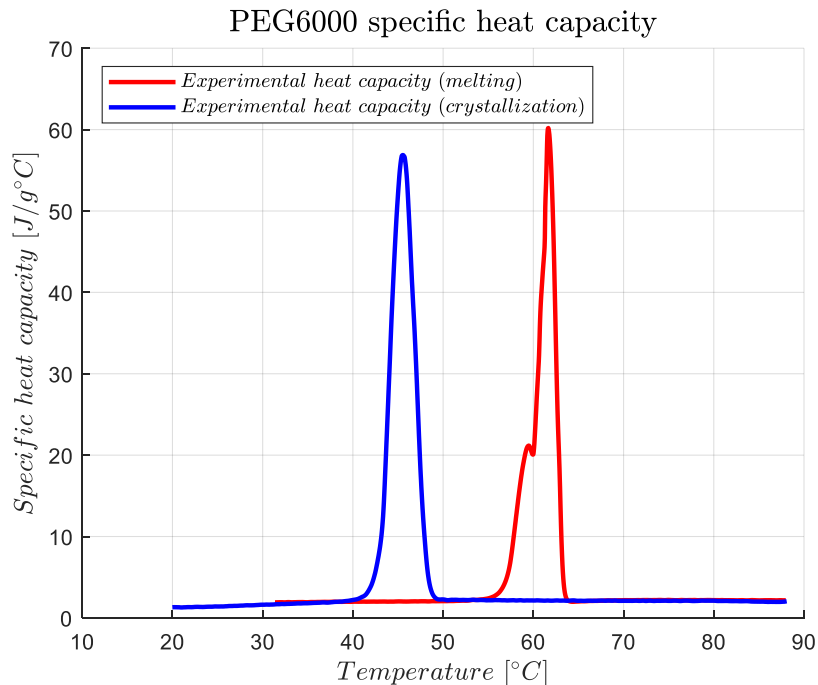


Figure 4-24. Experimental PEG 6000 specific heat for melting (red) and crystallization (blue) process

Two basic information emerge from the analysis of the figure. First of all, it can be seen that the specific heat trend is not exactly identical depending on whether the material is melting or crystallizing, even reaching different peak values. Furthermore, the figure shows how the temperature range in which the material melts is very different from that in which it crystallizes. As for the fusion process, it occurs between 55 and 63 °C, confirming what was declared by the manufacturer. However, by shifting the focus on the crystallization phase, the temperature range changes substantially, moving to a range between 42 and 50 °C. This phenomenon, not stated by the technical data supplied, lowers the level of temperature at which the latent heat is stored, and must certainly be considered for future applications. Finally, as regards the specific heat during the liquid and solid phase, it is established at a value around 2.3 J/g°C, as already stated by the manufacturer. However, it is necessary to clarify that the experimental values reported here might undergo some variations especially as a function of the heating/cooling rate, which, although set at 1 °C/min, does not perfectly reflect the actual behaviour of the PCM under real conditions of operation.

Finally, for the sake of completeness, the experimental trend of the specific enthalpy of the PEG6000 has also been evaluated and is shown in Figure 4-25 as a function of temperature. Also in this case the difference between the melting phase and the crystallization phase is evident. The data presented in the figure have not been referred to any reference value. However, what can easily be read from the graph is the value of the latent heat of fusion and crystallization, which corresponds to the enthalpy drop between liquid and solid state. As can be seen quantitatively, its value is around 190 J/g, in line with what was declared by the manufacturer (192 J/g).

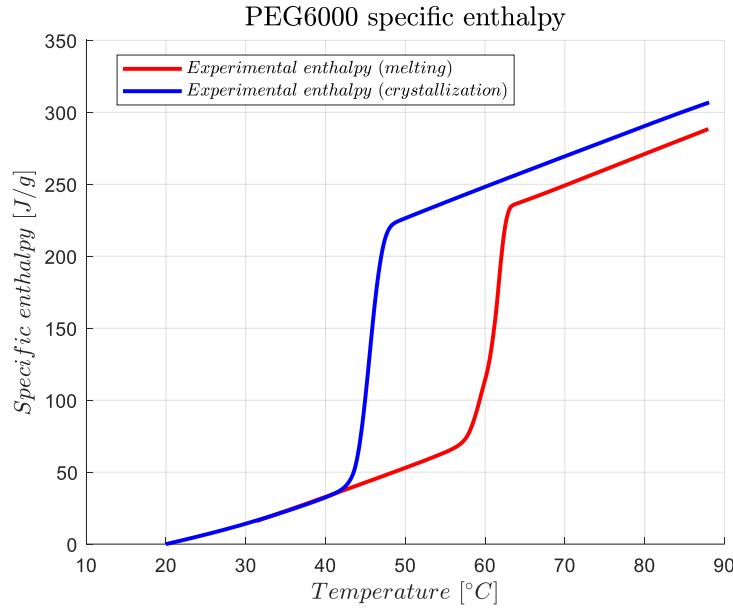


Figure 4-25. Experimental PEG 6000 specific enthalpy for melting (red) and crystallization (blue) process

4.3.3 Model building

After defining the specific heat trend as a function of temperature, the experimental results were used to build a mathematical model able to describe the physical behaviour of the PCM. To achieve this goal, reference was made to the analytical relationship proposed by (Kuznik, et al., 2006) to describe the specific heat curve evolution:

$$C_p = \begin{cases} a + b \cdot e^{-((T_{peak}-T)/4)^2} & \text{if } T \leq T_{peak} \\ a + b \cdot e^{-((T_{peak}-T)/3)^2} & \text{if } T > T_{peak} \end{cases}$$

Where a and b are two characteristic parameters of the material, while T_{peak} is the temperature value in which the peak value of the specific heat is reached. This point usually corresponds to the mean value of the melting or crystallization temperature range.

Using the proposed analytical relationship, it was therefore possible to analytically define two curves that describe the trend of specific heat as a function of temperature. Thanks to the experimentation data just found, it was possible to determine the values of the coefficients a and b , through a fitting process. The curve found thanks to the literature relation is shown in Figure 4-26, together with the experimental data collected on which it was modelled. This curve was subsequently used for the development of the mathematical model.

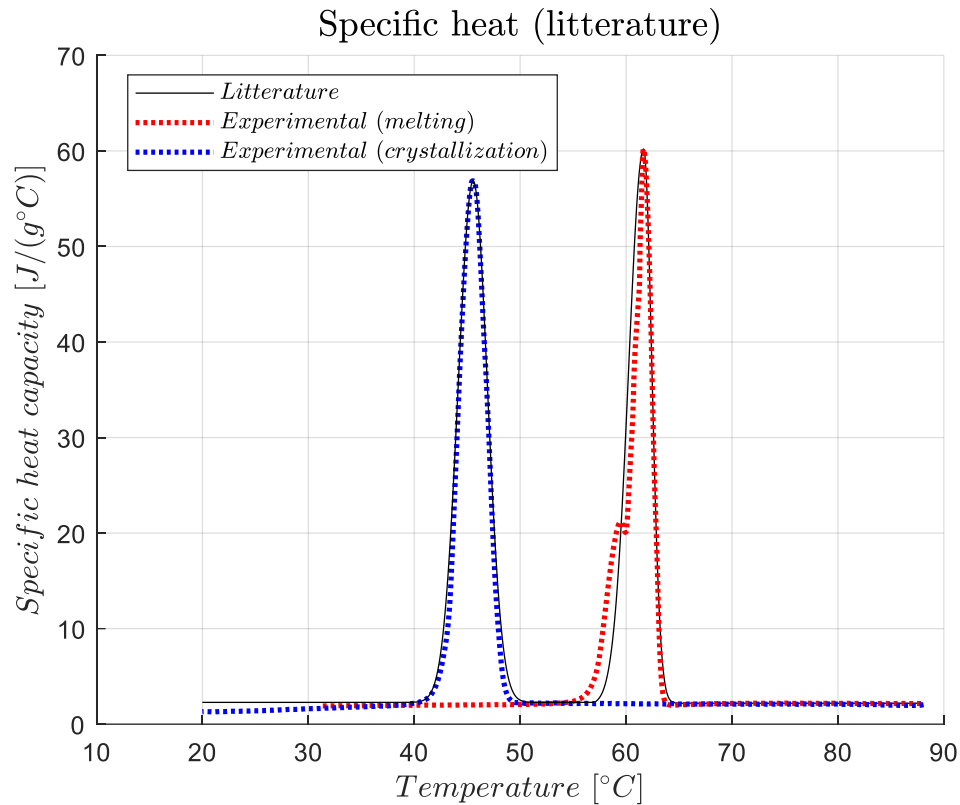


Figure 4-26. Experimental PEG 6000 specific heat fitting from litterature

4.3.4 Thermographic analysis

The experimental analysis on PCM was concluded with a photographic analysis, during which the behaviour of some PEG 6000 crystals was observed on a microscope. The apparatus used was an optical microscope equipped with a heating plate. After placing a sample of PEG 6000 on the heating plate, it was brought to melting temperature, observing the transition phase of the crystals. Once the liquid phase has been reached, the melted sample has been allowed to cool down naturally, until complete crystallization has been achieved again.

The evolution of the experiment was monitored through some images taken at different temperatures. Table 4-1 summarizes the phases of the experiment by indicating the elapsed time, the temperature reached, the size of the crystals (in solid phase), some notes and the corresponding picture.

Table 4-1. Microscopic analysis

<i>Time</i>	<i>Temperature [°C]</i>	<i>Crystal size [μm]</i>	<i>Note</i>	<i>Figure</i>
0:00	30.5	1394	Experiment starts	Figure 4-27
3:30	62	/	Instant fusion	Figure 4-28
3:35	65	/	Crystals disappear	Figure 4-29
14:23	43	/	Crystals appear	Figure 4-30
15:00	42	Evaluation impossible	Total recrystallization	Figure 4-31

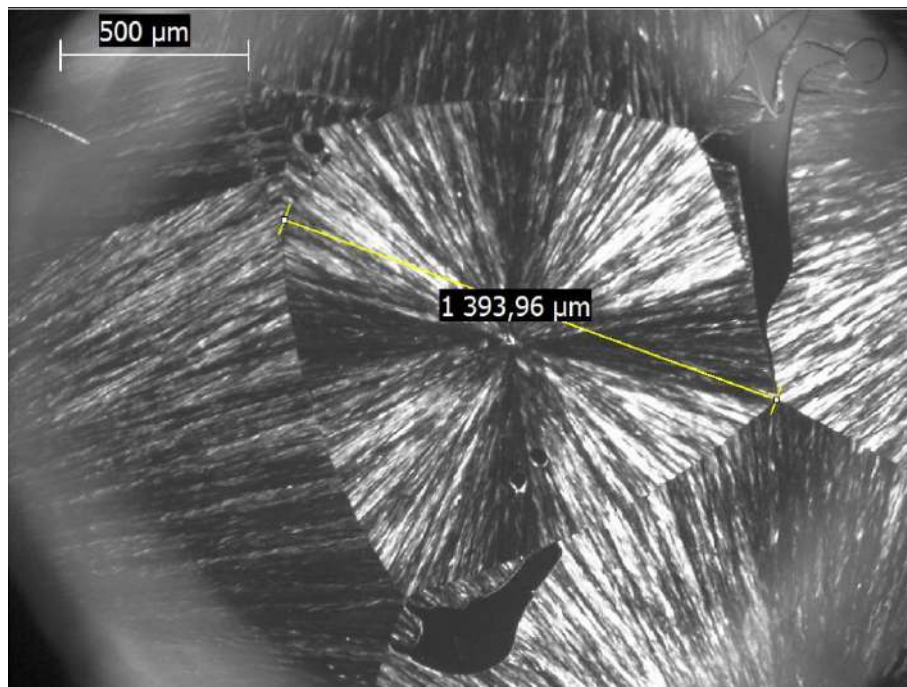


Figure 4-27. PEG 6000 microscopic view (T = 30.5 °C). Solid phase

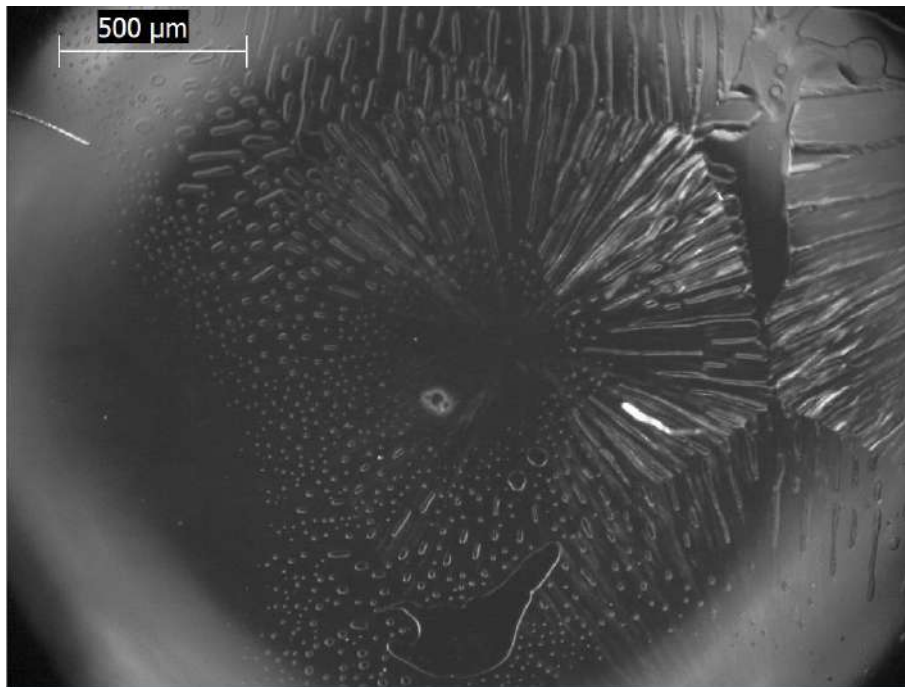


Figure 4-28. PEG 6000 microscopic view ($T = 62\text{ }^{\circ}\text{C}$). Melting phase

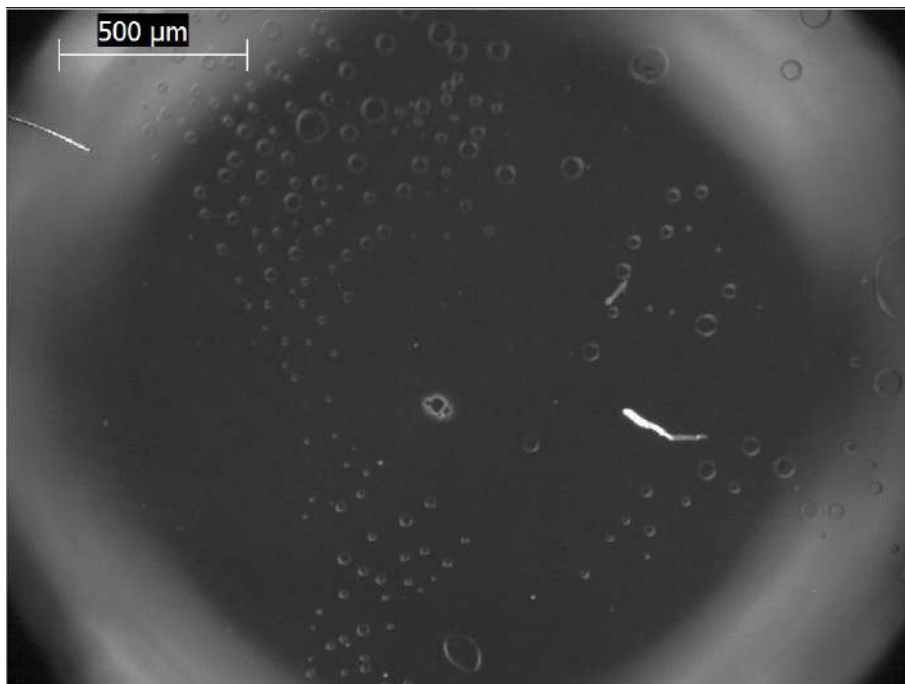


Figure 4-29. PEG 6000 microscopic view ($T = 65\text{ }^{\circ}\text{C}$). Liquid phase

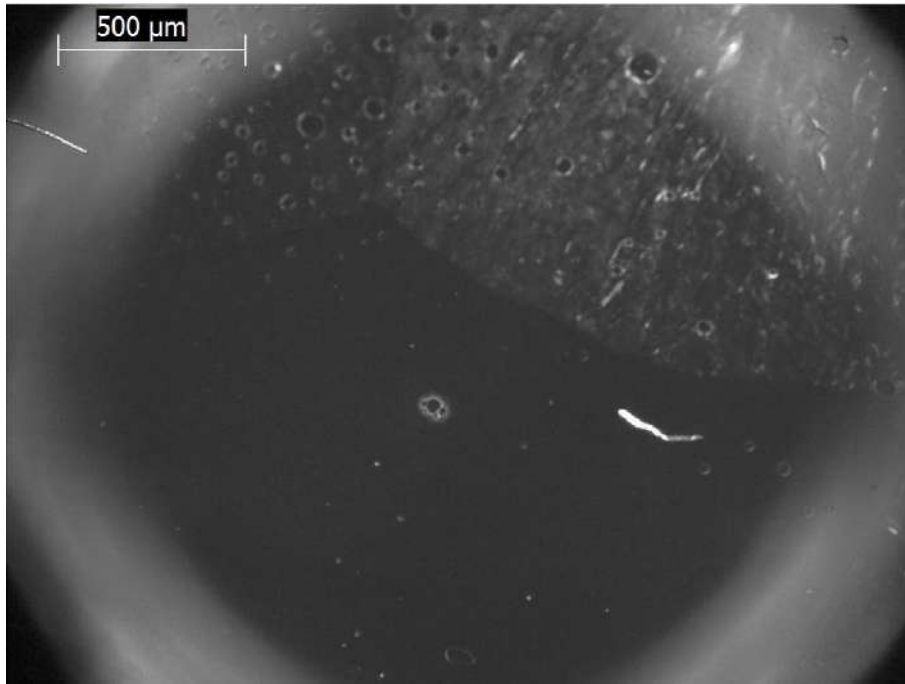


Figure 4-30. PEG 6000 microscopic view ($T = 43\text{ }^{\circ}\text{C}$). Crystallization phase

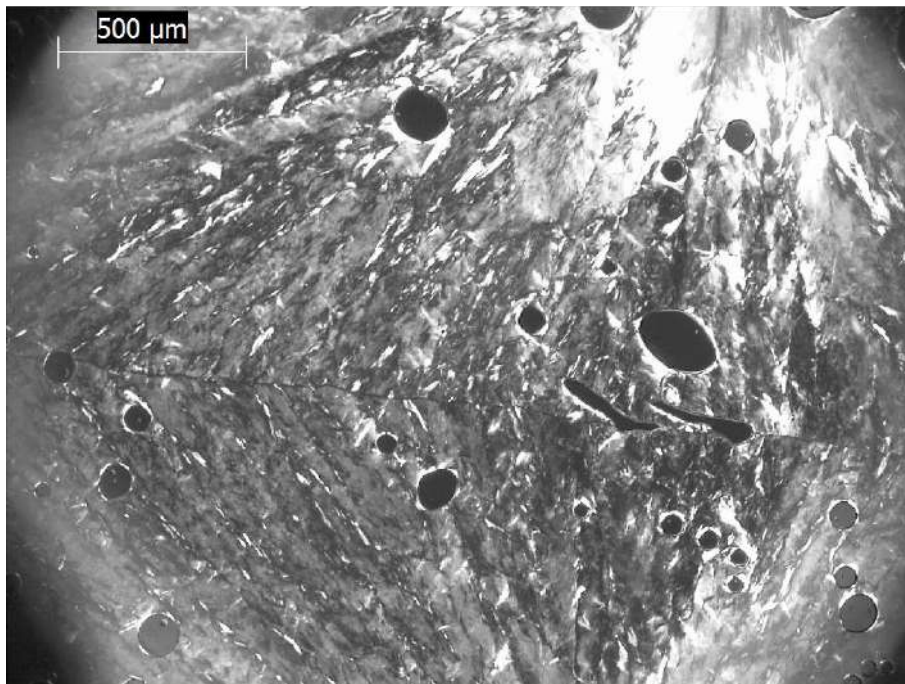


Figure 4-31. PEG 6000 microscopic view ($T = 42\text{ }^{\circ}\text{C}$). Solid phase

From these images showing a complete melting and crystallization cycle, it is noted that the PEG 6000 has a well-defined crystalline molecular structure, which however is lost when the material passes from the liquid to the solid state.

At the macroscopic level, while the material is supplied by the producer in the form of separate granules, after the first melting and crystallization it assumes a completely different appearance, losing the separation of the single grains and solidifying in a single block. This is in fact explained at the microscopic level by the Figure 4-31, where the crystals are no longer identifiable. Always referring to the same figure, we can notice the presence of some air bubbles trapped in the solidification process of the PCM. Precisely for this reason, during the repeated melting and solidification cycles, the volume of PEG 6000 tends to increase with respect to the starting value. From this point of view, the design choice of leaving 25% of free volume in the honeycombs cells is reasonable, so as to avoid mechanical stress inside the cavity.

4.4 Winter performances (February)

The experimentation period in the laboratory was concluded with the previous analysis. In February 2018 the prototype was again moved outside to study its performance with a winter climate. Unlike the first outdoor installation, this time the prototype was installed on a flat roof. The trend of the main temperatures is shown in Figure 4-32.

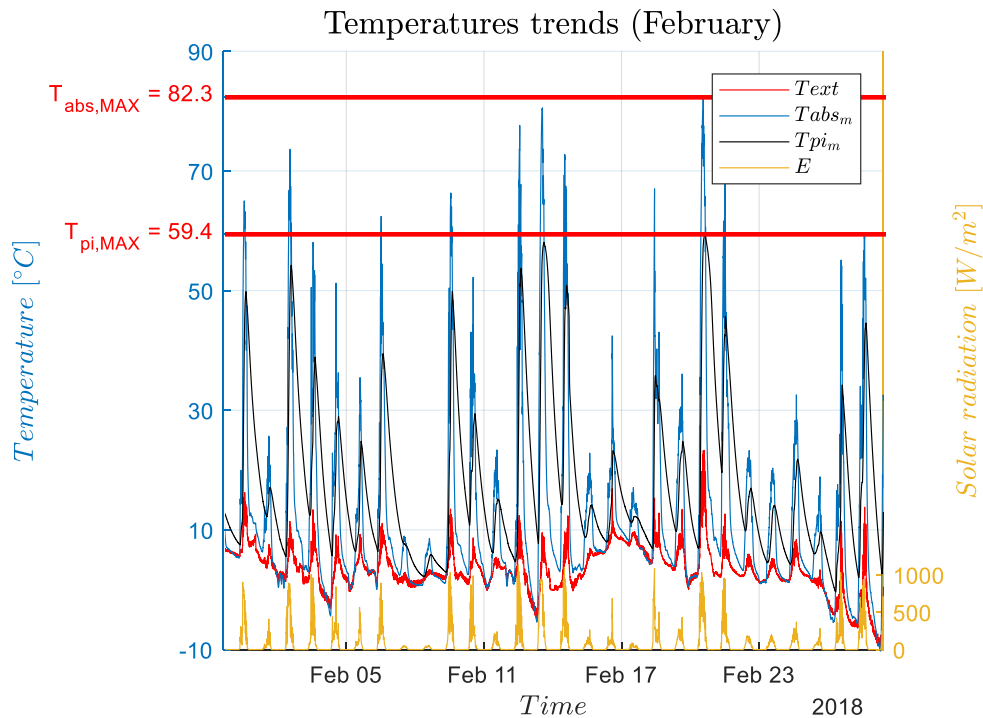


Figure 4-32. Main temperatures trends (February)

During the month of February, the outside temperature reached minimum values around -4 °C, never exceeding 20 °C. However, thanks to new implementations, the cavity has reached 60 °C, an acceptable value for the production of hot water. During this period a water withdrawal was also carried

out on February 14th. Figure 4-33 shows the trend of the temperatures at the inlet and outlet of the water coil, as well as the temperature trend of the two sides of the cavity. The sampling was carried out around 17:00 for a duration of about 20 minutes, when the cavity had a temperature of about 47 °C. The outlet temperature was maintained, over the duration of the sampling, above 25 °C. Also in this case the water flow used was around 0.8 l/min. The significant difference in temperature between the water outlet and the cavity confirms a poor efficiency of the heat exchange in the water coil, which proves to be one of the aspects that requires major improvements in the future.

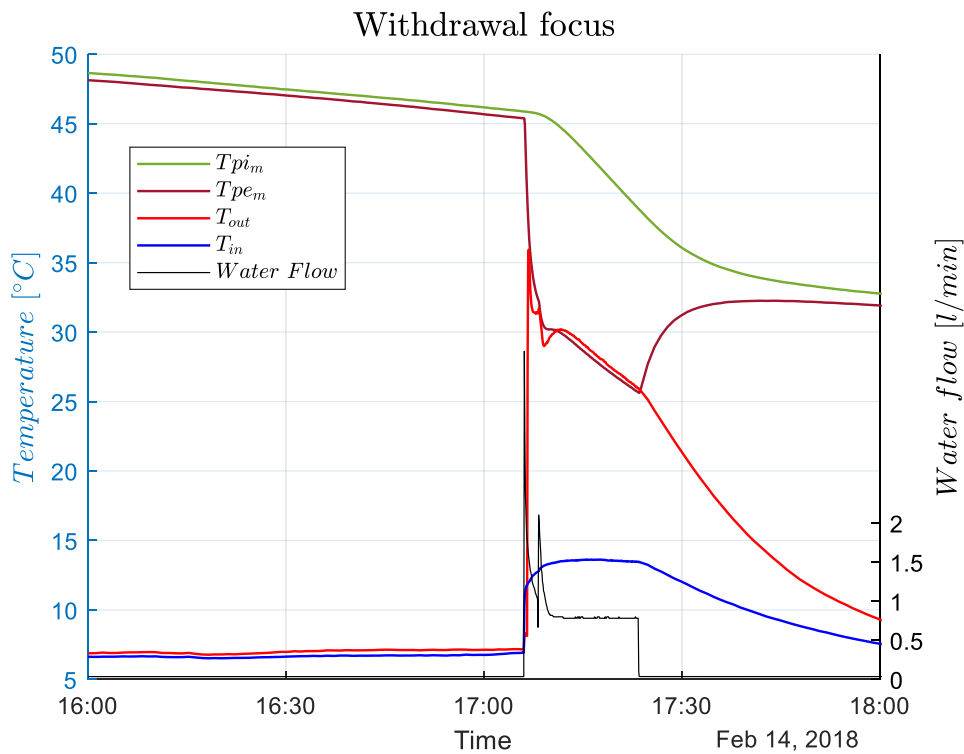


Figure 4-33. Water withdrawal temperatures detail during February 2018

Again, the power extracted from the storage was evaluated. Because of the lower temperatures involved, the power extracted is lower than that obtained in the summer, settling on an average value of around 950 W (Figure 4-34).

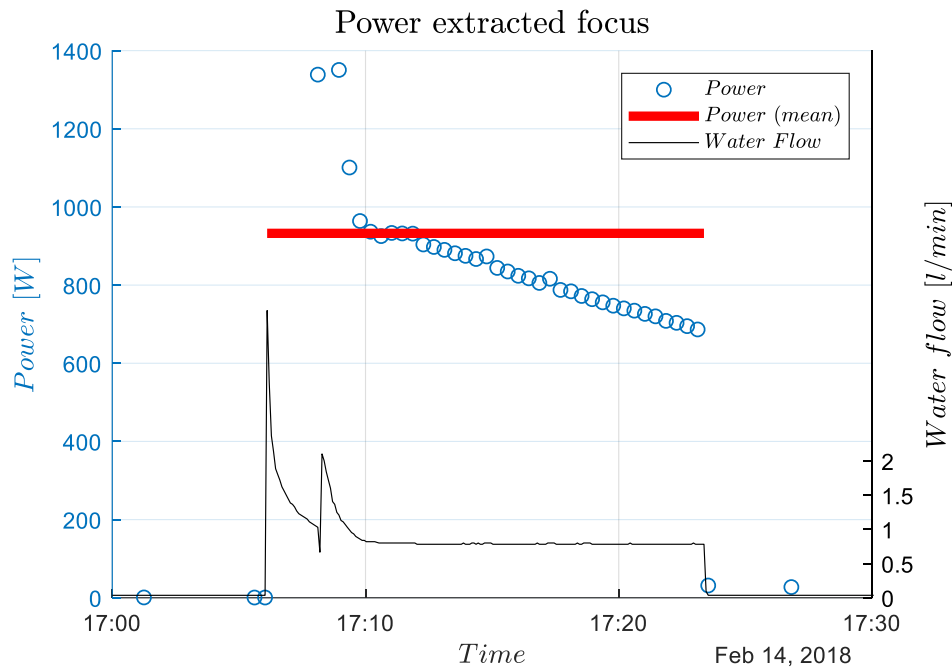


Figure 4-34. Extracted power from water withdrawal in February 2018

4.5 Key performance indicators (KPIs)

To conclude this section dedicated to the experimental analysis of the prototype, some indicators will be presented that briefly describe the main technical characteristics of the system studied, and in particular the effectiveness of the energy storage section. The set of indicators, already presented in the introductory chapter of this thesis (section 1.5), have been proposed in Annex 31, drafted by (IEA, 2018). The main values were collected in Table 4-2, and are the result of the experimental analyses conducted before the structural renovation of the prototype and already presented by (Fraisie, et al., 2017) combined with the new analyses presented in this chapter, after having modified the prototype.

Table 4-2. KPIs values for ICS prototype (IEA, 2018)

<i>No.</i>	<i>KPI</i>	<i>Value</i>	<i>Comment</i>
<i>1a</i>	Storage total capacity	16.9 kWh	
<i>1b</i>	Storage useful capacity	16.9 kWh	
<i>2</i>	Recharging energy	31.0 kWh	
<i>3a</i>	Maximum charge power	~0.5 kW	Solar radiation energy (1000 W/m ²)
<i>3b</i>	Maximum discharge power	3.13 kW	
<i>4</i>	Depth of discharge (DOD)	100%	
<i>5</i>	Durability (numbers of cycles)	1825	5 years is the PCM lifetime
<i>6</i>	Specific cost of the storage	0.02 €/kWh	
<i>7</i>	Maximum self-discharge rate	4.13% (1h) 9.99% (10h)	
<i>8a</i>	Storage size	0.02 m ³	
<i>8b</i>	Storage weight	24 kg	
<i>9a</i>	Energy storage factor on demand	100%	
<i>9b</i>	Energy storage factor on RES production	N/A	To be defined in a building integration
<i>10</i>	Generated energy/cost saving	N/A	To be defined by monitoring

Chapter 5

5 Numerical modelling

The following chapter has been entirely dedicated to the development of a mathematical model able to describe the ICS performances, considering all its internal components. Knowing the actual solar radiation, the external temperature and the water inlet temperature used during the withdrawals, the model is able to describe the prototype thermal behaviour and its internal temperatures profiles. The input data used in the model have been directly collected on the field experiments, improving in this way the reliability of the modelling validation process. Moreover, taking advantage from the exhaustive experimental analysis already performed, some unknown design parameters are defined in order to decrease the computational cost and simplify the model structure. Due to the general complexity and the high number of components, every single element has been modelled following a one-dimensional approach. However, a different procedure has been developed for the PCM cavity model, that is described with a two-dimensional model, trying to simulate its real behaviour as well as possible.

All the modelled components will be carefully examined in the next dedicated sections, pointing out the main governing equations and the energy balances.

The ICS model has been modelled into the EES (Engineering Equation Solver) environment, an equation-solver program able to numerically solve non-linear algebraic and differential equations. The early modelling phase was subsequently followed by an optimization phase, integrated in the same program, with the aim to improve the reliability of the model, especially regarding unknown parameters.

The aim of this chapter is therefore to propose a numerical model and validate it by means of the experimental data just analysed. The entire EES code used for simulating the prototype behaviour is collected in Appendix B.

5.1 Components models

The studied prototype, as already widely discussed, can be detached into several components, that starting from the top are:

- Solar thermal absorber (glass, air gap, absorber plate);
- Heat pipes;
- Insulation layers (both at the front and at the back);
- DHW pipeline;
- PCM cavity.

The following picture provides a schematic view of the ICS components modelled.

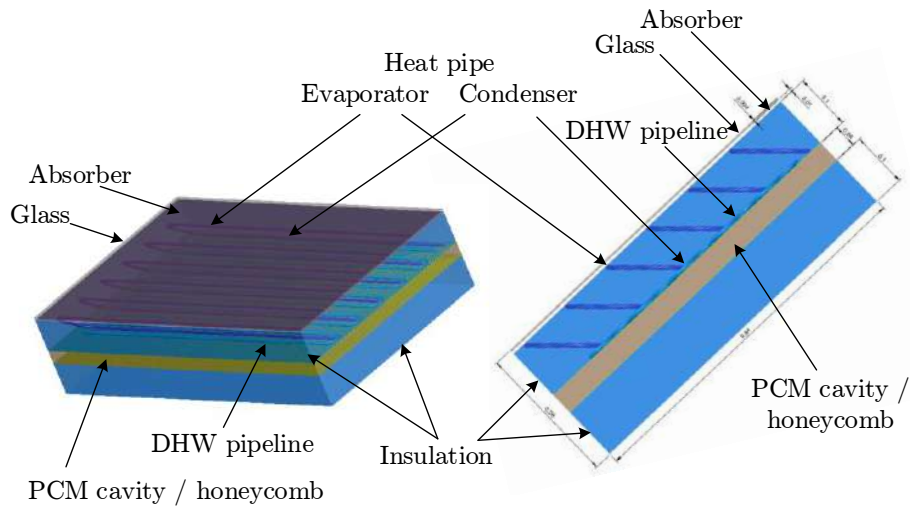


Figure 5-1. ICS 3D view with main components

A proper numerical model was developed for each component. After that, energy balances at each temperature node have been set to simulate the whole system. The next picture clearly presents the electrical analogy according to which the ICS was modelled. The nomenclature used is the same as the experimental study. Except the PCM cavity, every layer is considered one dimensional. For this reason, the temperature at nodes are supposed to be constant along the surface. On the other hand, the PCM cavity, together with the aluminium plates, is discretized into 21 separate nodes (7 in the x direction, 3 in the y direction), generating a two-dimensional pattern. While the x-axis represents the main direction, normal to the absorber plane, the y-axis indicates a direction parallel to the prototype width. The way in which the pattern of the nodes becomes two-dimensional is shown successively in Figure 5-8, where through a more detailed analysis it will be explained how the temperature node T_{pe} communicates with the nodes T_{11} , T_{12} and T_{13} .

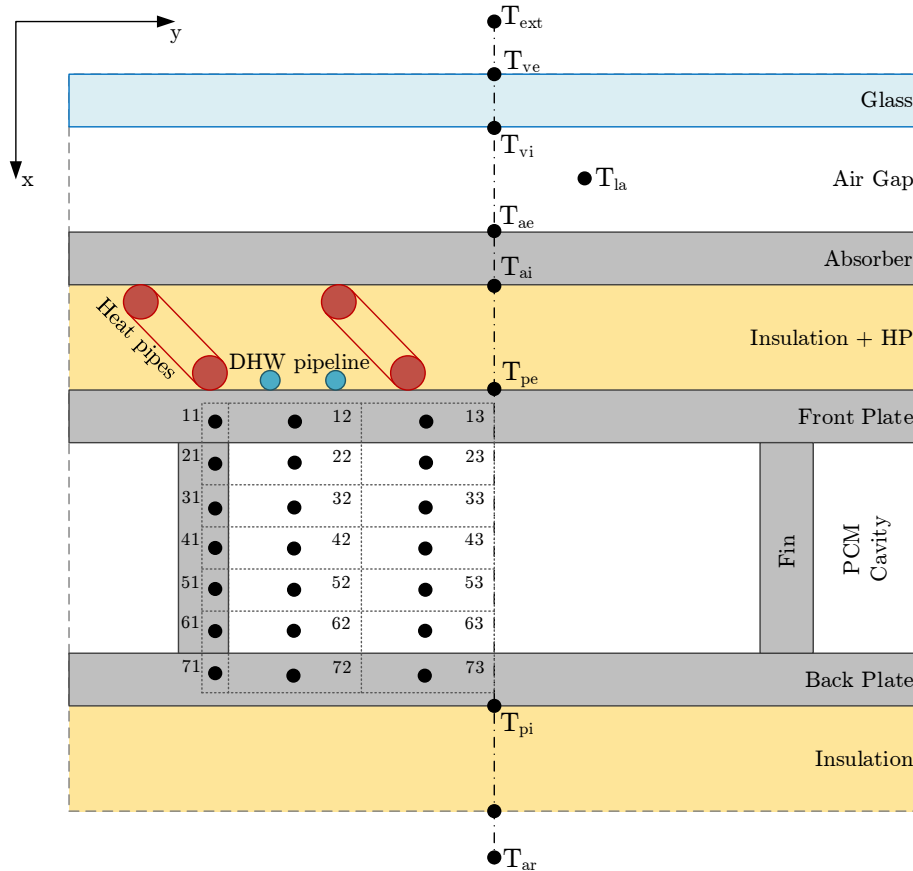


Figure 5-2. ICS model scheme with sections and temperature nodes (black dots)

Each of the following sections has been dedicated to one or more individual components of the model, explaining the physical parameters adopted to develop the model and the governing equation involved. The modelling approach was the electrical analogy, where temperatures, heat flows and thermal resistances and heat capacity take the place of voltage, current, resistors and capacitor respectively. Furthermore, Fourier's law replaces Ohm's law and heat capacity equation takes the place of capacitor equation. Several electrical schemes will be presented step by step separately to make them easier to understand. However, the union of all these will then compose the final model implemented in EES.

The model has been studied according to different timesteps, depending on the function performed. Generally, temperature changes in the prototype are very slow. However, faster changes occur during the water withdrawals, when the internal component are subjected to large temperature variations.

5.1.1 Solar thermal absorber

This first component is considered as the merging of the glass cover, the absorber plate and the air gap in between. The main design parameters, such as

thermal conductivity, thickness and properties coefficients were provided by the manufacturer or evaluated from the literature and are collected in Table 5-1.

Table 5-1. Glass, air and absorber properties

<i>Category</i>	<i>Parameter</i>	<i>Nomenclature</i>	<i>Value</i>	<i>Unit</i>
<i>Glass</i>	Transmission coefficient (direct)	τ_{DIR}	0,8	-
	Transmission coefficient (diffuse)	τ_{DIF}	$\tau_{DIR} * 0,849$	-
	Absorption coefficient	α_{glass}	0,07	-
	Conductivity	λ_{glass}	1,2	W/(mK)
	Thickness	e_{glass}	0,004	M
<i>Air gap</i>	Laminar convective coefficient	h_c	4	W/(m ² ·K)
	Radiative coefficient	h_r	$4 \cdot \epsilon_{abs} \cdot \sigma$	W/(m ² ·K ⁴)
	External global heat coefficient	h_e	16	W/(m ² ·K)
<i>Absorber</i>	Absorption coefficient	α_{abs}	0,8	-
	Emissivity coefficient	ϵ_{abs}	0,2	-
	Thickness	e_{abs}	0,0002	m
	Conductivity	λ_{abs}	380	W/(mK)
	Azimuth angle	Az	0	°
	Slope angle	β	30	°

Therefore, some geometrical parameters have been defined, in order to compute the solar radiation incidence angle:

$$\begin{aligned} \cos\theta_i &= \cos\delta\cos(\phi - \beta)\cos\omega + \sin\delta\sin(\phi - \beta) \\ I &= \arccos(\cos(H_S) * \sin(\beta) * \cos(A_{zs} - A_z) + \sin(H_S) * \cos(\beta)) \end{aligned}$$

Where H_S is height of the sun, H_S the absorber slope, A_{zs} ad A_z the solar and the absorber azimuth respectively.

By the evaluation of the incidence angle I , the direct (E_{dir}) and diffuse (E_{dif}) radiation, together with their glass transmission coefficient (τ_{DIR} and τ_{DIF}) have been computed, starting from the total radiation collected by the in-site pyranometer. Afterwards, the main solar fluxes are computed as follows:

$$\begin{aligned} \varphi_{solt} &= \tau_{DIR} * E_{dir} + \tau_{DIF} * E_{dif} \left[\frac{W}{m^2} \right] \\ \varphi_{abs} &= \varphi_{solt} * \alpha_{abs} \left[\frac{W}{m^2} \right] \\ \varphi_{absV} &= E * \alpha_{glass} \left[\frac{W}{m^2} \right] \end{aligned}$$

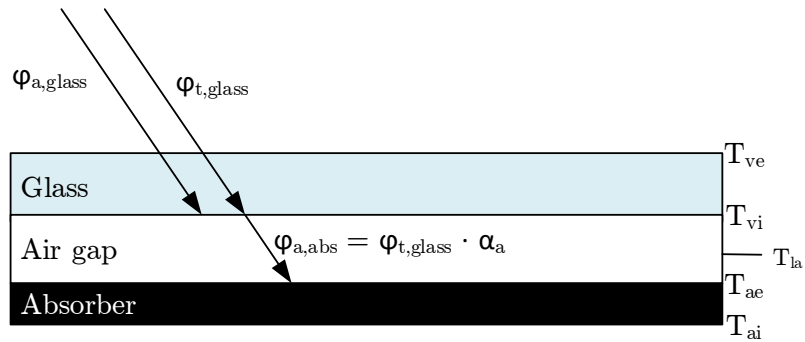


Figure 5-3. Solar fluxes on the collector

Where φ_{solt} is the solar flux through the glass, while φ_{abs} and φ_{absV} are the absorbed fluxes by the absorber and the glass layer respectively.

Once the external solar fluxes are defined, the collector has been modelled following a one-dimensional electrical analogy, as shown in Figure 5-4. For this first component 6 different temperature nodes are set: starting from the outside we face the external ambient air (T_{ext}), the external glass surface (T_{ve}), the internal glass surface (T_{vi}), the air gap (T_{la}), the external absorber (T_{ae}) and the internal absorber (T_{ai}). 5 corresponding energy balances, normalized for the collector area, are set at each temperature notes and they are collected in Table 5-2.

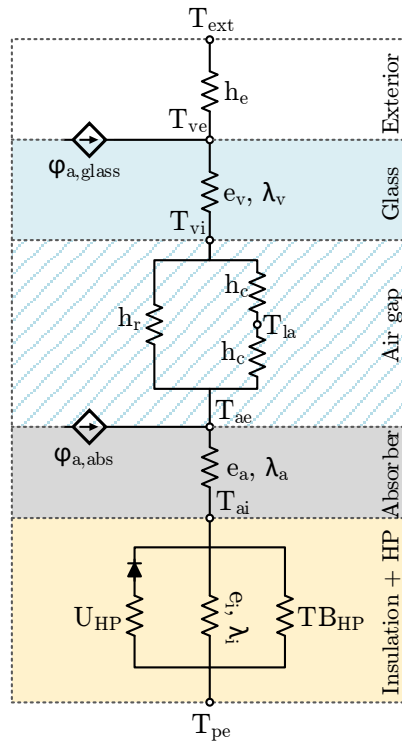


Figure 5-4. Collector electrical scheme

Table 5-2. Temperature nodes balances (part 1)

<i>Temperature node</i>	<i>Description</i>	<i>Energy balance</i>
T_{ve}	Glass surface external	$h_e \cdot (T_{ext} - T_{ve}) + \alpha_{glass} \cdot E = \frac{T_{ve} - T_{vi}}{\frac{e_{glass}}{\lambda_{glass}}}$
T_{vi}	Glass surface internal	$\frac{T_{ve} - T_{vi}}{\frac{e_{glass}}{\lambda_{glass}}} = h_r \cdot (T_{vi} - T_{ae}) + h_c \cdot (T_{ve} - T_{la})$
T_{la}	Air gap	$h_c \cdot (T_{vi} - T_{la}) = h_c \cdot (T_{la} - T_{ae})$
T_{ae}	Absorber surface external	$h_r \cdot (T_{vi} - T_{ae}) + \frac{\varphi_{abs}}{S} + h_c \cdot (T_{la} - T_{ae}) = \frac{T_{ae} - T_{ai}}{\frac{e_{abs}}{\lambda_{abs}}}$
T_{ai}	Absorber surface internal	$\frac{T_{ae} - T_{ai}}{\frac{e_{abs}}{\lambda_{abs}}} = \frac{T_{ai} - T_{pe}}{\frac{e_i}{\lambda_i}} + \#_{HP} \cdot \frac{\dot{Q}_{HP}}{S}$

As can be seen, all the thermal resistances are taken into account for each layer. Regarding the air gap, both the convective and radiative heat transfer coefficients are considered in the energy balance, while its temperature is supposed to be the mean value between the two adjacent surfaces. It is also important to notice that the internal absorber temperature node is also influenced by the layer below, where the insulation material and the heat pipes take place.

5.1.2 Heat pipes

Six copper U-shaped heat pipes are installed in the prototype analysed and placed inside the insulation layer that separates the absorber plate from the storage cavity. Heat pipes play the role of the main heat transfer carrier as well as thermal diode to allow the heat flow just in one direction, from the absorber to the cavity. The heat flux provided by heat pipes is modelled from their conductance U_{HP} , according to the relation:

$$\varphi_{HP} = U_{HP} * \Delta T_{HP} [W]$$

Where ΔT_{HP} is the temperature difference between the evaporator and the condenser. To simplify the model those temperatures are supposed to be equal to the contact surface where they are installed. According to this hypothesis, the evaporator temperature is equal to T_{ai} (absorber backside temperature) whereas the condenser temperature equals T_{pe} . Regarding the conductance coefficient

U_{HP} , a constant value for the model has been chosen after the appropriate experimental data analysis carried out in Chapter 4. A constant U_{HP} value is a significant approximation for the model. However, this hypothesis allows to save a considerable computational cost, without compromising the simulation results, especially during large simulation time scenarios. A more detailed model, considering a variable conductance as a function of the heat pipe wall temperature was studied (Rudy, et al., 2016). Starting from this advanced model, a characteristic table describing the heat pipe operation as a function of T_{ai} and T_{pe} was carried out. Nevertheless, even though this model takes into account several operating regimes as well as heat pipe thermal limits, implement such a precise model is not always worth it, mainly because of its detrimental effect over the computational time.

Besides the useful flux provided from the heat pipes, losses have been considered too. According to the heat pipe geometry, another heat transfer coefficient was computed to take into account thermal bridges across the heat pipe profile.

$$TB_{HP} = \lambda_{copper} * \pi * \left(\frac{D_e^2 - D_i^2}{4 * e_i} \right) \left[\frac{W}{K} \right]$$

Where D_e and D_i are the external and internal pipe diameters and lambda is the copper thermal conductivity. The heat flux lost by the heat pipe due to the thermal bridges is therefore:

$$\varphi_{HP,TB} = TB_{HP} * \Delta T_{HP} [W]$$

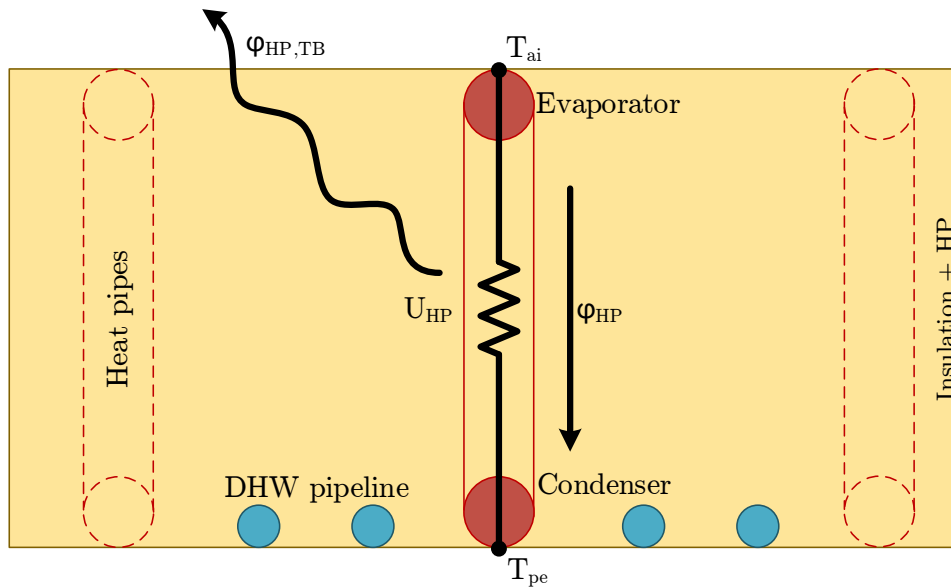


Figure 5-5. Heat pipes section: 2D scheme

The following table collects all the design parameters used to define the heat pipes model.

Table 5-3. Heat pipe properties

<i>Category</i>	<i>Parameter</i>	<i>Nomenclature</i>	<i>Value</i>	<i>Unit</i>
<i>Heat pipe</i>	Global heat transfer coefficient	U_{HP}	1,6	W/K
	External diameter	D_e	0,012	m
	Internal diameter	D_i	0,011	m
	Conductivity	λ_{HP}	350	W/(mK)
	HPs installed	$\#_{HP}$	6	-
	HP length	L_{HP}	1	m
	HP width	$W_{HP} (=e_i)$	0,08	m

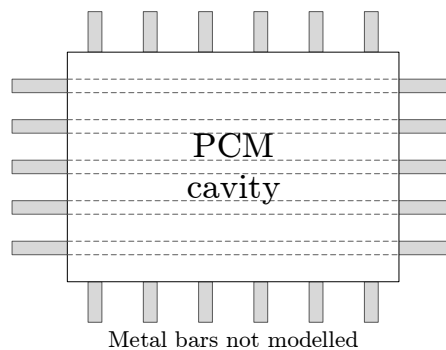
5.1.3 Insulation layer

Since a one-dimensional modelling approach was preferred, only two different insulation layers were modelled, even though the insulation material inside the prototype surrounds the entire cavity surface in each of its sides. Rockwool was used as insulator, and its thermal properties implemented in the model are collected in the table below.

Table 5-4. Insulation properties

<i>Category</i>	<i>Parameter</i>	<i>Nomenclature</i>	<i>Value</i>	<i>Unit</i>
<i>Insulation</i>	Thickness – front	$e_{i,front}$	0,08	m
	Thickness – back	$e_{i,back}$	0,02	m
	Conductivity	λ_i	0,04	W/(mK)

As you can notice, the insulation thickness for the layer at the back of the model does not respect the actual measures, supposed to be around 7cm. Such a lower value was used to take into account the thermal losses all around the cavity, due mainly to the metallic supports holding the PCM cavity. The latter were not considered in development of the model and their negative contributions affects the modelled value of the insulation thickness.

**Figure 5-6. Metal bars holding the cavity: not modelled**

5.1.4 Plates and cavity

The PCM cavity is composed by the external aluminium structure and by the PCM limited inside. The interior of the cavity also presents a honeycomb structure to keep the PCM spaced in several cells. As already said, the cavity has been modelled following a two-dimensional approach in both x and y directions. The spatial discretization of the cavity is based on a sample cell, and its thermal behaviour has been normalized to the honeycomb cell section. The 2D mesh counts 21 temperatures nodes (3 in the y direction and 7 in the x direction) including the front cavity aluminium plate, the PCM itself, the aluminium fin that spaces the honeycomb structure and the aluminium plate at the back. The aluminium plates at the front and the back fill the first and last layers of the mesh in y direction, while the fin develops just along the x direction. The rest is filled by the PCM.

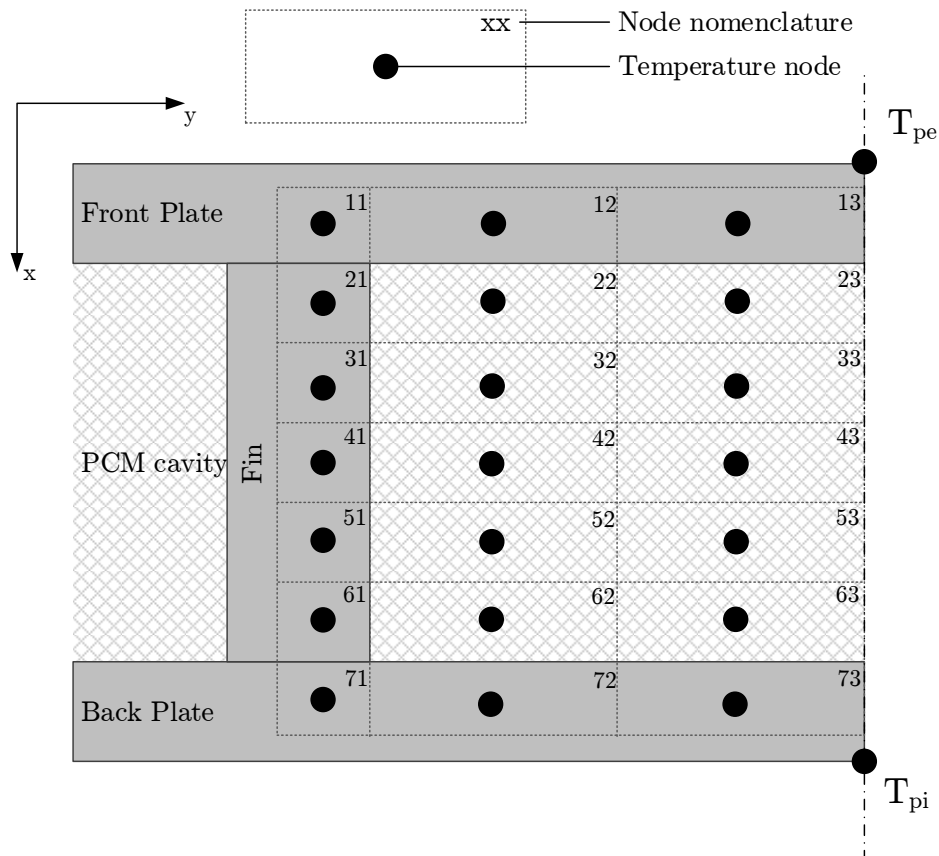


Figure 5-7. PCM cavity mash

Following this scheme, it was possible to evaluate the PCM temperature at each volume in the mesh, in such a way that the specific heat capacity was better evaluated, especially during the phase change region around 60°C . The honeycomb filling ratio, as declared by the manufacturer, is 75%, allowing the PCM to expand when it melts. Since the single cell is not completely filled by PCM an air layer has been considered at the top of the honeycomb cell. Its

thickness equals 25% of the cell height. The filling ratio has been also taken into account in the specific heat evaluation. Regarding the honeycomb dimensions, its surfaces was approximated to a cylindrical shape with an equivalent diameter. All the main design parameters are collected in the next table.

Table 5-5. Cavity plate, metal fins and honeycomb structure properties

<i>Category</i>	<i>Parameter</i>	<i>Nomenclature</i>	<i>Value</i>	<i>Unit</i>
<i>Plates</i>	Thickness	e_{pl}	$0,81e^{-3}$	m
	Density	ρ_{pl}	2699	kg/m ³
	Specific heat	$c_{p,pl}$	897	J/(kgK)
	Conductivity	λ_{pl}	180	W/(mK)
<i>Fin</i>	Thickness	e_{fin}	$0,71e^{-3}$	m
	Density	ρ_{fin}	2699	kg/m ³
	Specific heat	$c_{p, fin}$	897	J/(kgK)
	Conductivity	λ_{fin}	180	W/(mK)
	Length	L_{fin}	0,04	m
<i>Honeycomb (HC)</i>	Equivalent diameter	D_{HC}	0,00971	m
	Surface	S_{HC}	$0,74e^{-4}$	m ²
	Filling ratio	fr	0,75	-
	Air layer thickness	$e_{air,PCM}$	0,01	m

The cavity model was linked to the rest of the components by setting two energy balances either at the front and the back of the aluminium plate layers, placed right after the insulation layers. As for the previous components, balances are set using an electrical analogy. Their solution will lead to the cavity temperature at the front and the back, respectively T_{pe} and T_{pi} . These two temperatures have a singular meaning because they will be used to validate the model, giving comparable values with the experimental data. As previously discussed, in the experimental setup, thermocouples have been installed right in both locations to monitor the cavity temperature, since the PCM itself was sealed inside it. The plate temperatures are therefore the best comparison method that we have between the numerical model and the experimental data. In the next picture the energy balance at both the nodes is pointed out.

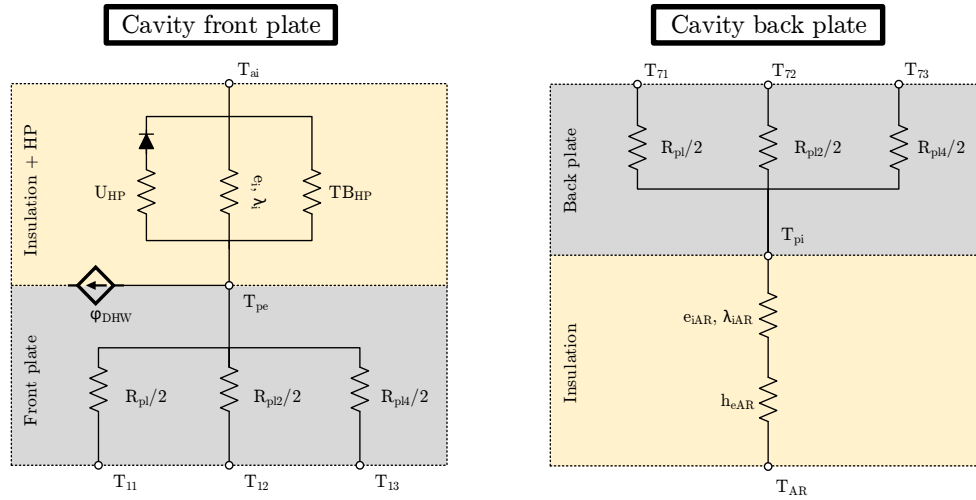


Figure 5-8. Electrical analogy of T_{pe} and T_{pi} nodes

Table 5-6. Temperature node balances (part 2)

Temperature node	Description	Energy balance
T_{pe}	Cavity plate External	$\frac{T_{ai} - T_{pe}}{\frac{e_i}{\lambda_i}} \cdot S_{HC} + [\#_{HP} \cdot \dot{Q}_{HP} + \#_{HP} \cdot TB_{HP} \cdot (T_{ai} - T_{pe}) - \varphi_{DHW}]$ $\cdot \frac{S_{HC}}{S} = \frac{T_{pe} - T_{11}}{\frac{R_{pl}}{2}} + \frac{T_{pe} - T_{12}}{\frac{R_{pl2}}{2}} + \frac{T_{pe} - T_{13}}{\frac{R_{pl4}}{2}}$
T_{pi}	Cavity plate Internal	$S_{HC} \cdot \left[\frac{T_{pi} - T_{AR}}{\frac{e_i}{\lambda_i} + \frac{1}{h_{eAR}}} \right] = \frac{T_{pi} - T_{71}}{\frac{R_{pl}}{2}} + \frac{T_{pi} - T_{72}}{\frac{R_{pl2}}{2}} + \frac{T_{pi} - T_{73}}{\frac{R_{pl4}}{2}}$

We can move now to the inside of the cavity, where the PCM is stored in the honeycombs. As you can notice from the plates energy balances, the inside of the cavity takes into account a 2-dimensional modelling scheme, structured into 21 different nodes divided in 7 layers. The first and last nodes layers take into account the aluminium plate thickness. The remaining ones simulate the aluminium fin and the PCM. Taking advantage of the symmetrical shape of the honeycomb, the modelled volume includes just half of a cell, for reasons of simplicity. Inside the cavity, the stored heat into the PCM is simulated by a capacitor, that takes into account the specific heat. In addition to this, thermal capacity is also considered for the aluminium plates, while has been neglected for the fin. Energy balances are set at each of the 21 nodes to solve the temperature pattern inside the cavity. Between each cell composing the mesh, specific thermal resistances have been computed to better simulate the actual thermal behaviour. According to the cylindrical geometry of the honeycomb, several radii were set to describe the cell distance from the symmetry axes (Figure 5-9).

Therefore, thermal resistances in y (r) direction are:

$$R_{th,r} = \frac{\ln\left(\frac{r_o}{r_i}\right)}{2 * \pi * L * k} \left[\frac{K}{W} \right]$$

On the other hand, thermal resistances following x axes direction are:

$$R_{th,x} = \frac{L}{k * A} \left[\frac{K}{W} \right]$$

Where, in both cases, L is the length, k is the thermal conductivity (PCM or aluminium) and A is the surface considered. The following picture shows the main geometry parameters involved in the cavity mesh, as well as the main thermal resistance computation.

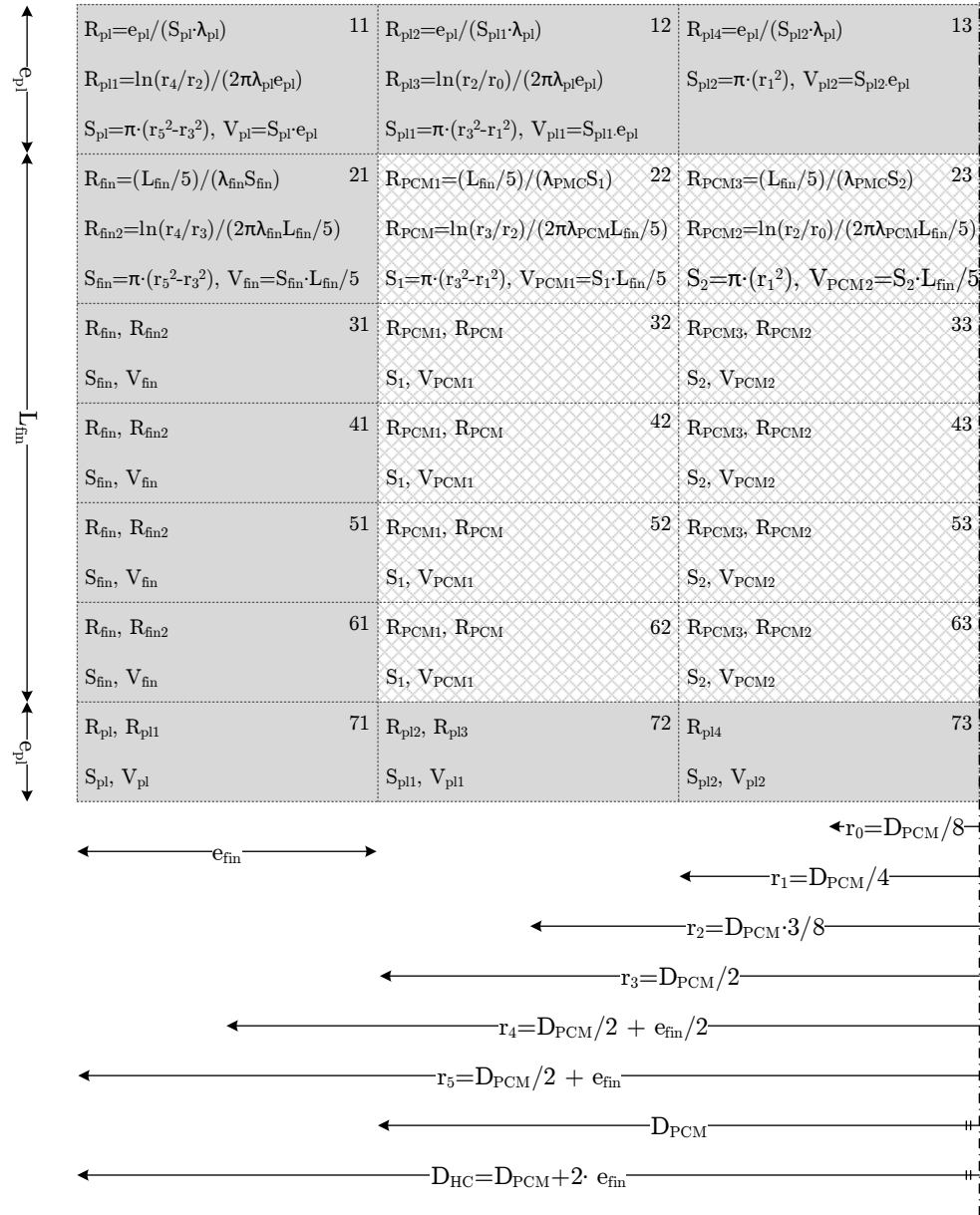


Figure 5-9. Radii, surfaces, volumes and main thermal resistances adopted in the cavity model

Figure 5-9 points out surfaces S , volume V and thermal resistances R connected to each of the cell's temperature nodes. In the first nodes these parameters have been computed in the picture. The same values are than repeated for the rest of the nodes, depending on their position in the mesh. Surfaces and volumes take into account the cylindrical shape of the honeycomb and they were used to compute thermal resistances and heat capacity respectively.

Figure 5-10 translates into electrical analogy what has just been said, placing the thermal resistances and the capacitors in the mesh.

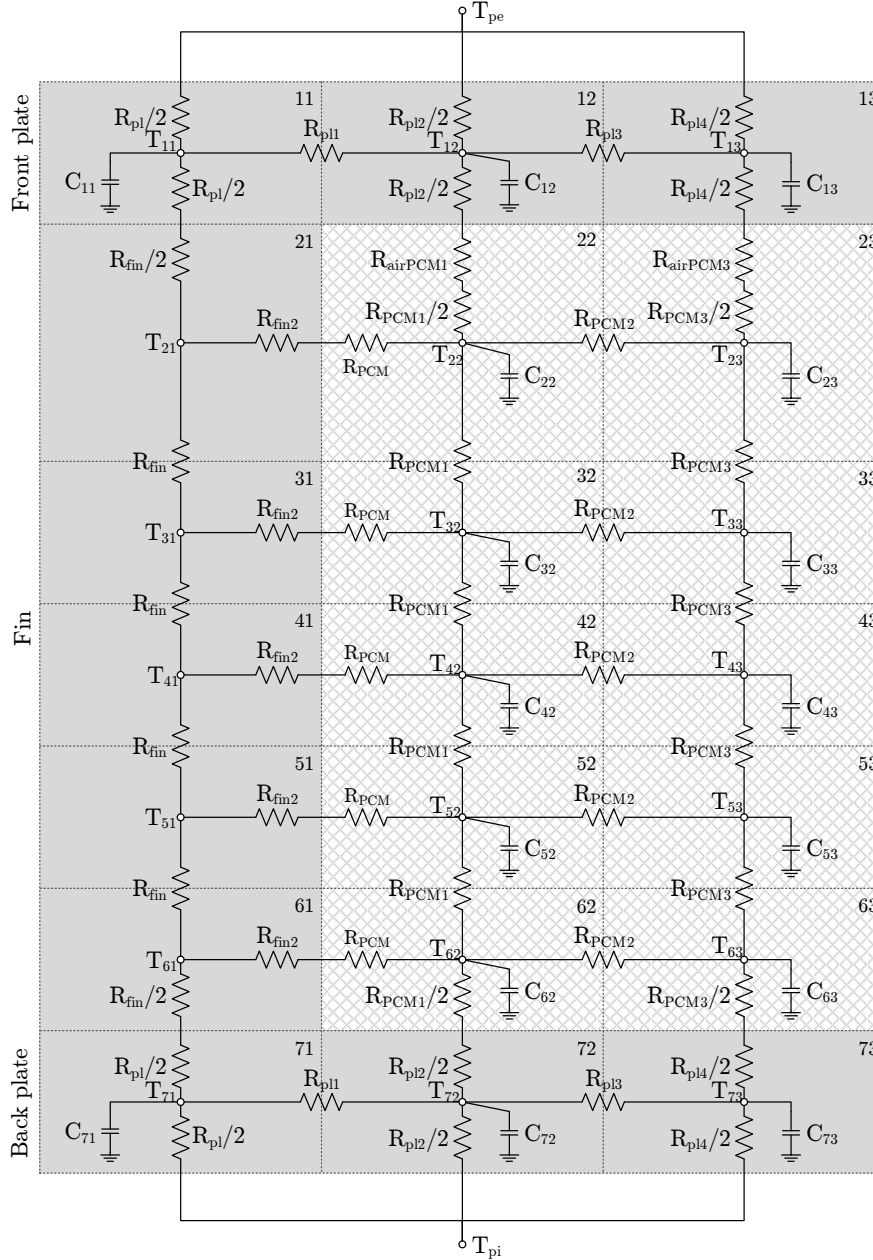


Figure 5-10. Cavity: electrical analogy model

Finally, energy balances can now be solved. The next formulas show 4 balances out of 21, in order to present the typical energy balance formulation.

Table 5-7. Temperature node balances (part 3)

<i>Temperature node</i>	<i>Description</i>	<i>Energy balance</i>
-------------------------	--------------------	-----------------------

T_{12}	Aluminium plate layer	$C_{12} \cdot \frac{dT_{12}}{dt} = \frac{T_{11} - T_{12}}{R_{pl1}} + \frac{T_{13} - T_{12}}{R_{pl3}} + \frac{T_{22} - T_{12}}{\frac{R_{pl2}}{2} + \frac{R_{PCM1}}{2}} + \frac{T_{pe} - T_{12}}{\frac{R_{pl2}}{2}}$
T_{22}	PCM layer with air	$C_{22} \cdot \frac{dT_{22}}{dt} = \frac{T_{21} - T_{22}}{R_{PCM} + R_{ail2}} + \frac{T_{23} - T_{22}}{R_{PCM2}} + \frac{T_{12} - T_{22}}{\frac{R_{PCM1}}{2} + \frac{R_{pl2}}{2}} + R_{air,PCM1} + \frac{T_{32} - T_{22}}{R_{PCM1}}$
T_{42}	PCM layer	$C_{42} \cdot \frac{dT_{42}}{dt} = \frac{T_{41} - T_{42}}{R_{PCM} + R_{ail2}} + \frac{T_{43} - T_{42}}{R_{PCM2}} + \frac{T_{32} - T_{42}}{R_{PCM1}} + \frac{T_{52} - T_{42}}{R_{PCM1}}$
T_{41}	Fin cell	$0 = \frac{T_{31} - T_{41}}{R_{ail}} + \frac{T_{51} - T_{41}}{R_{ail}} + \frac{T_{42} - T_{41}}{R_{ail2} + R_{PCM}}$

Where C is the heat capacity, computed as:

$$C = c_p \cdot \rho \cdot V \left[\frac{J}{^\circ C} \right]$$

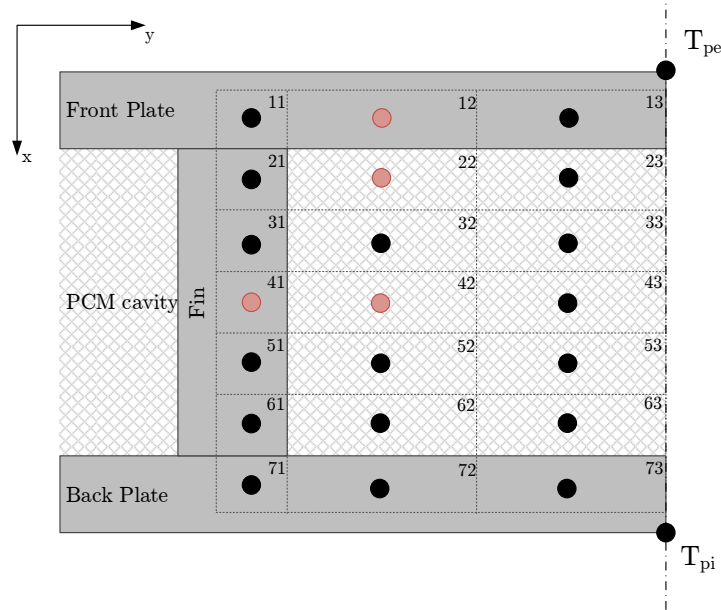


Figure 5-11. Temperature nodes (red dots) corresponding to the energy balances in Table 5-7

An overview of the model developed following the approach of the electrical analogy can be found in Appendix C, where all the components described above have been combined into a single exemplary figure.

5.1.5 PCM modelling

A deeper understanding is deserved by the phase change material model and especially by its thermal properties, collected in Table 5-8.

Table 5-8. PCM properties

<i>Category</i>	<i>Parameter</i>	<i>Nomenclature</i>	<i>Value</i>	<i>Unit</i>
<i>PCM</i>	Melting region	T_{fus}	53-64	°C
	Crystallization region	T_{cri}	43-51	°C
	Density	ρ_{pl}	1210	kg/m ³
	Specific heat capacity – liquid	$c_{\text{p,PCM,l}}$	2466	J/(kgK)
	Specific heat capacity – solid	$c_{\text{p,PCM,s}}$	2161	J/(kgK)
	Conductivity	λ_{pl}	0,2	W/(mK)
	Equivalent diameter (HC placement)	D_{PCM}	0,009	m

The melting and crystallization temperatures range might vary depending on the heating and cooling rate adopted. For this study purpose those ranges were defined using the same heating and cooling rate of 1 °C/min, that was the closest possible to real operation condition (around 0,5 °C/min).

All these parameters, some provided by the manufacturer, other proceeds from previous studies, have been implemented in the model definition. However, a more careful description must be given during the double phase region, where the PCM specific heat is not constant anymore. Therefore, the previous experimental DSC analysis performed over a PEG 6000 sample is now integrated inside the model parameters, to describe the specific heat trend during the melting phase. In this way, the model is able to read a c_p value depending on the simulated temperature at each node in the cavity. The specific heat curve, dependent from the temperature, was already pointed out in Figure 4-26, and it is nothing but a fitting curve from the literature formula considered the best one to describe the PCM behaviour (Kuznik, et al., 2008):

$$c_p = \begin{cases} a + b \cdot e^{-\left(\frac{T_f - T}{4}\right)^2} & \text{if } T \leq T_f \left[\frac{J}{g \cdot ^\circ C} \right] \\ a + b \cdot e^{-\left(\frac{T_f - T}{3}\right)^2} & \text{if } T > T_f \left[\frac{J}{g \cdot ^\circ C} \right] \end{cases}$$

Where a and b are two characteristic parameters and T_f is the mean temperature to which fusion occurs. The same formula, with different parameters is also applied to the cooling procedure, when the liquid PCM solidifies.

Once the best fitted curves for both melting and freezing were defined, interrupted cooling and heating phenomena were addressed, especially when they occur during the double phase temperature range. In other words, a specific model description is required when the PCM inside the cavity starts to melt and then is cooled down without reaching the 100% liquid phase. In this case, as well as in the opposite one, when the solidification procedure is interrupted, the c_p behaviour may be ambiguous. For this reason, a specific approach has been used to describe interrupted cooling and heating phenomena based on the studies

carried out by (Delcroix, et al., 2015) and (D'Avignon, et al., 2016). According to them, when heating or cooling is stopped during a double phase region, the specific heat curve (as well as the enthalpy curve) lays in between the melting and freezing ones.

Figure 5-12 and Figure 5-13 show the c_p and enthalpy curves implemented in the model when the melting or crystallization phases are interrupted. The red line describes the melting process, the blue one represents the freezing process and the dashed line describes the PCM c_p (or h) values during an interrupted heating or cooling process. For instance, as shown in Figure 5-12, if PCM starts melting until reaching 60°C (point 2 in the picture) without reaching the complete liquid phase (over 65°C approximately) and then is cooled down to 40°C (point 4 in the picture), its specific heat curve does not lay neither on the melting curve nor on the freezing one, but “jumps” on an average curve (point 3). While cooling continues, specific heat follows the mean c_p curve (dashed line) until the PCM is completely solid (point 4). From solid state, when heating conditions are applied again and the material starts melting, it will follow the standard melting red line.

The same phenomenon happens in the opposite way when we are dealing with interrupted cooling (Figure 5-13). In this case, PCM is cooled down from liquid condition, starting the solidification process. When cooling is interrupted without reaching the solid state (point 2) and the PCM is heated, its specific heat value will move on the dashed mean curve, until the liquid state is reached again (point 4).

For the sake of clarity, it is important to stress that a normal melting or freezing process, without any interruptions, only involves one single c_p or h curve, from the beginning to the end. The mean curve is called into question only when a phase change is interrupted.

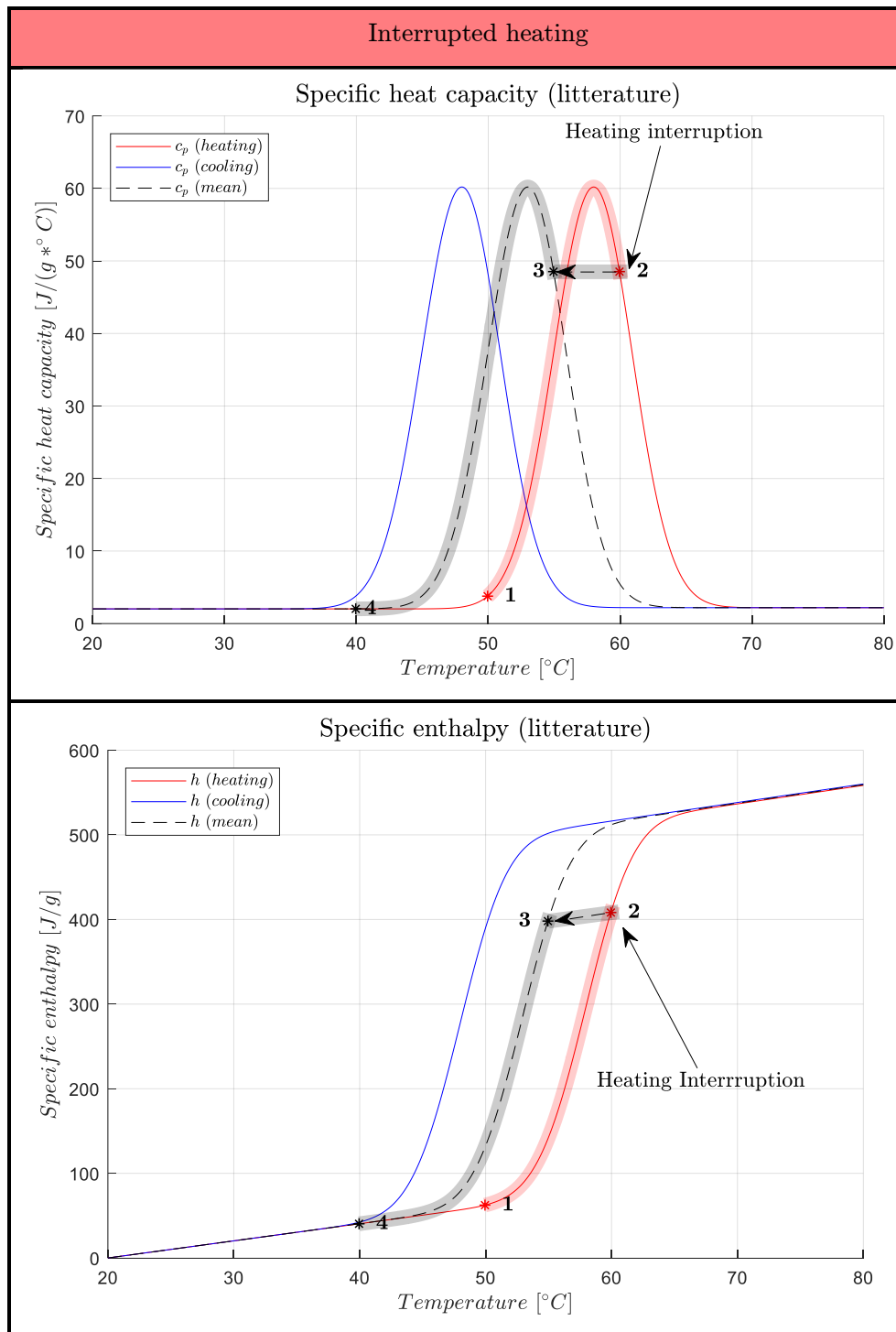


Figure 5-12. Interrupted heating: assumption implemented in the model

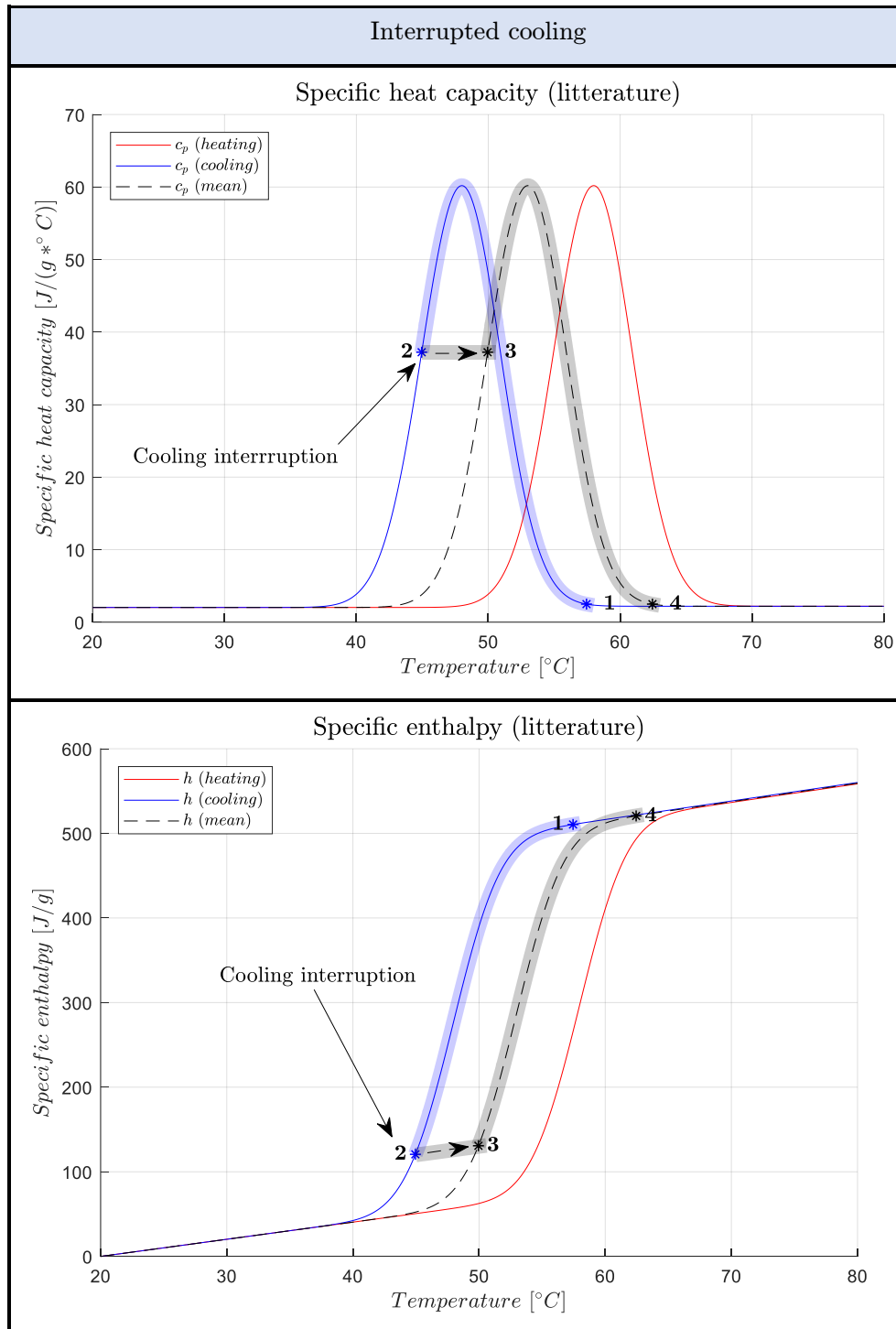


Figure 5-13. Interrupted cooling: assumption implemented in the model

5.1.6 DHW heat exchanger

Another fundamental component is the domestic hot water pipeline, in charge of providing hot water to the user. The DHW pipeline has been modelled following its geometry and considering a mean temperature for the water flowing inside. Moreover, for simplicity's sake, the external surface temperature of the pipeline corresponds to the front plate temperature (T_{pe}), since these two components are stuck together. The heat flux exchanged by forced convection is linked to the pipeline internal temperature and the water temperature flowing inside, according to the formula:

$$\varphi_{DHW} = \pi \cdot D_{i,DHW} \cdot L_{DHW} \cdot h_{c,DHW} \cdot (T_{si,DHW} - T_{mean,w})$$

Where D_i and L are respectively the internal diameter and the pipeline length, h_c is the heat transfer coefficient. The latter was computed from the Nusselt number, according to the type of state, turbulent or laminar:

$$h_{c,DHW} = \lambda_w \cdot \frac{Nu}{D_{i,DHW}}, \text{ where}$$

$$Nu = \begin{cases} Nu_{lam} = 3,66 + 0,0668 \cdot \left[\frac{Re \cdot Pr \cdot \frac{D_{i,DHW}}{L_{DHW}}}{1 + 0,04 \cdot \left(Re \cdot Pr \cdot \frac{D_{i,DHW}}{L_{DHW}} \right)^{2/3}} \right] \\ Nu_{turb} = 0,023 \cdot Pr^{1/3} \cdot Re^{0,8} \end{cases}$$

The same heat exchanged by conduction throughout the pipeline walls is:

$$\varphi_{DHW} = \frac{(T_{se,DHW} - T_{si,DHW})}{\frac{\ln \left[\frac{D_{e,DHW}}{D_{i,DHW}} \right]}{2 \cdot \pi \cdot \lambda_{DHW} \cdot L_{DHW}}}$$

Where $T_{se} - T_{si}$ is the temperature difference across the pipeline walls. Finally, the heat provided to the water flow it can be expressed by means of the mass flow and water temperature increase:

$$\varphi_{DHW} = \dot{m}_w \cdot c_{p,w} \cdot (T_{w,out} - T_{w,in})$$

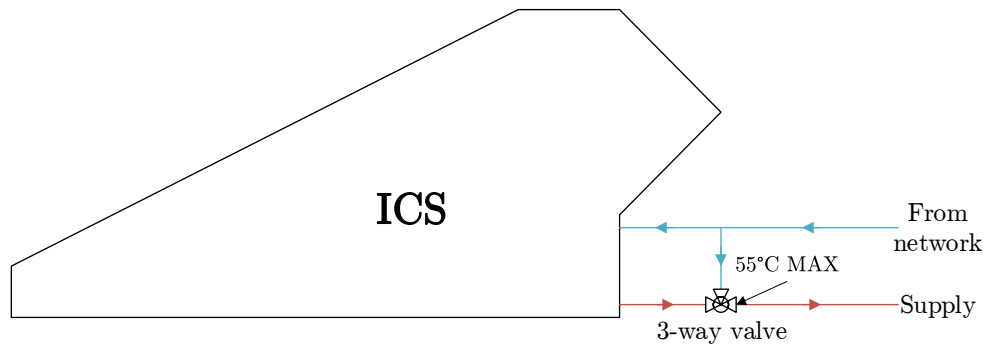
Where $T_{w,out} - T_{w,in}$ is the water temperature difference between the pipeline inlet and the outlet.

All the parameters used to model this section are now collected in the following table, representing both the geometric quantities and the physical properties of water.

Table 5-9. DHW pipeline and water properties

<i>Category</i>	<i>Parameter</i>	<i>Nomenclature</i>	<i>Value</i>	<i>Unit</i>
<i>DHW pipeline</i>	External diameter	D_e	0,008	m
	Internal diameter	D_i	0,006	m
	Length	L_{DHW}	10	m
	Section	S_{DHW}	0,28e-4	m ²
	Conductivity	λ_{DHW}	350	W/(mK)
<i>Water</i>	Dynamic viscosity	μ_w	5,7e-4	Pa*s
	Density	ρ_w	986	Kg/m ³
	Conductivity	λ_w	0,6525	W/(mK)
	Specific heat capacity	$c_{p,w}$	4213	J/(kgK)

In order to improve the model performance and simulate a real behaviour for a possible building implementation, a 3-way valve was added to the model with the task to keep the outlet water temperature below 55°C, mixing the water coming out from the solar collector with by-passed cold water from the main network. This simple hydraulic scheme, pointed out in Figure 5-14 was adopted to have a better energy economy in the system and improve its performance since a water production over 55°C is not the purpose of this study.

**Figure 5-14. Hydraulic scheme with 3-way mixing valve**

The 3-way valve regulates the water flow flowing through the collector pipeline ensuring an outlet temperature of 55°C during a scheduled withdrawal.

5.1.7 Input and boundary conditions

Now that all the main model components are reviewed, a brief explanation about input parameters is needed. First of all, two types of simulation have been performed, requiring slightly different input data between each other. Initially the model was validated according to real experimental data collected on site. For this experience the external temperature, solar radiation, cold water temperature and water flow were used as direct inputs for the model, running short time simulations corresponding to the experimental data collection. In addition, the starting temperature for the PCM cavity was set equal to the

experimental one. A second simulation cluster was later focused on long-time performance, simulating the prototype energy performances during different times of the year. The latter simulation set was then performed using meteorological data from a nearby weather station for solar radiation and external temperature, while the cold-water temperature, used for the withdrawals, was given by average values depending on the season.

5.2 Model validation

Model validation is a process of great importance to verify the reliability of the assumptions made with the aim of giving a powerful tool to perform further analysis. Different experimental conditions have been considered to validate the model. As already said, the actual experimental data were used as input parameters for the model. The validation process involved the on-site operation during two different periods of the year. The first one was during summer season, from June 2017 to August 2017. Later, in February 2018, the model was validated in winter condition. During both periods, normal operation was tested, allowing the cavity to perform standard heating and cooling cycles. Typical water withdrawals were subsequently tested, focusing on the cavity behaviour and its temperature drop. In order to get better results, different simulation timesteps were used depending on the experiment performed. Normal operation was studied with a 30 seconds timestep, while for the withdrawals, requiring a faster-time comprehension, the timestep was reduced to 5 seconds. The same timesteps used for simulating the model were adopted by the data acquisition system in the experimental bench.

During the course of the validation process temperature trends were compared between real data and simulation results. To test normal operation conditions special attention was focused to the absorber and cavity temperature, considered as the most relevant temperature nodes to prove model's reliability. On the other hand, water withdrawal simulation moved the attention to water outlet temperature, as well as cavity temperature drop.

Starting from summer period, a typical week in august 2017 was analysed in Figure 5-15, showing normal operation for a week. Absorber (T_{abs}) and inferior cavity plate were simulated (T_{pi}) and compared with the experimental data (solid line). Last picture points out the actual solar radiation during the week (red solid line), showing an ordinary radiation behaviour. However, last day was mostly cloudy, having a considerable impact on the model. Looking at the absorber temperature, the simulated trend faithfully reflects the experimental data, even when solar radiation has not a smooth behaviour. Regarding the temperature at the back of the cavity (T_{pi}), simulated results describe quite well real data, despite having some issues when solar radiation does not follow a typical daily trend.

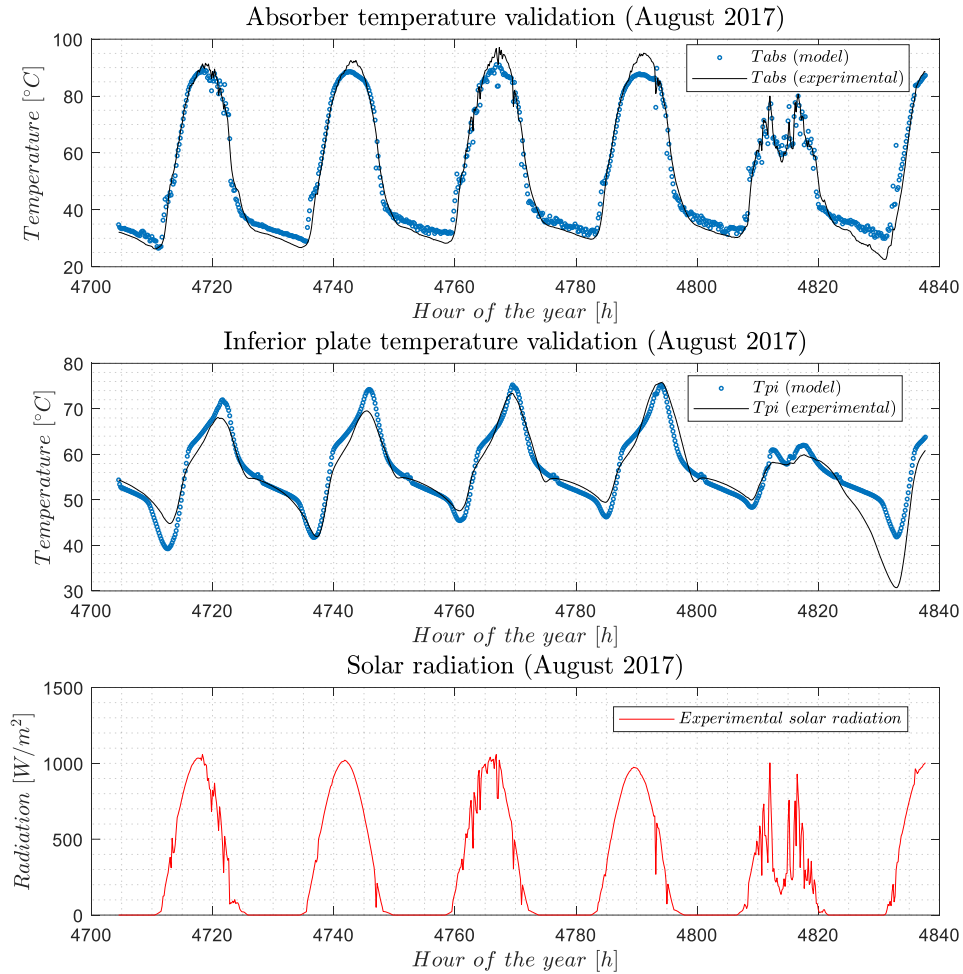


Figure 5-15. Absorber (T_{abs}) and inferior cavity plate (T_{pi}) temperature simulation in August 2017

Focusing now on the cavity temperature, the first simulated day is shown in Figure 5-16. Even though the model does not meet properly the real data at the beginning of the day (most likely because it has not yet reached steady state conditions), the cooling phase overnight produces satisfactory results, describing PCM temperature trend with considerable accuracy. The red area highlighted in the picture emphasises the sub-cooling region that occurs in the PCM and has been taken into account for the model definition.

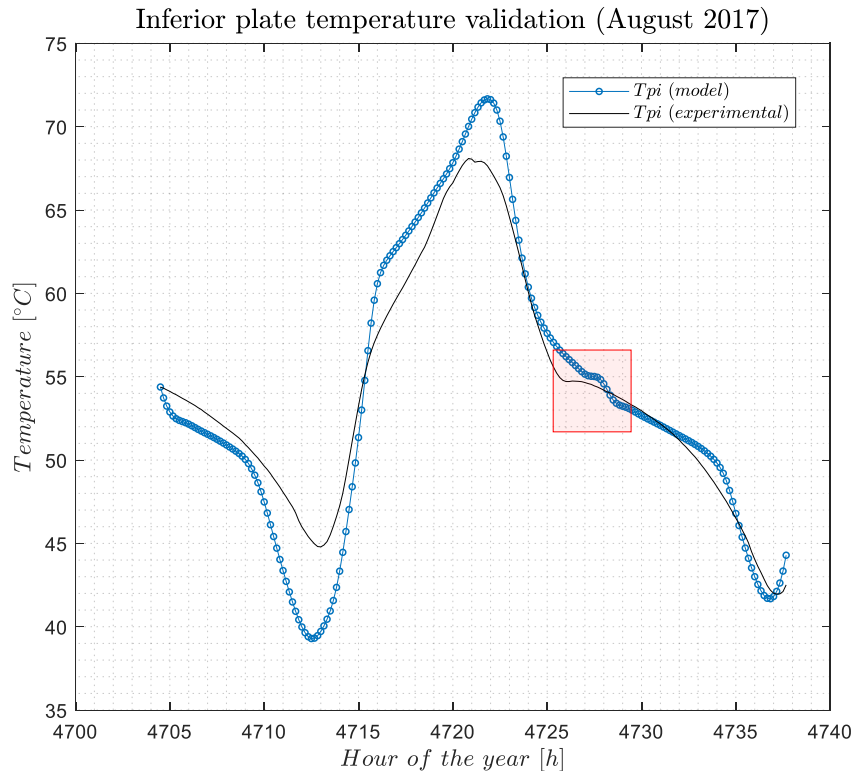


Figure 5-16. Cavity temperature simulation (T_{pi}): sub-cooling detail

During July 2017, the ability to produce hot water has been tested with simple water withdrawals from the collector pipeline. A water flowrate of 3.3 l/min was extracted from the collector at 3:00 a.m., for three following days from July 4th. In Figure 5-17 the experimental data collected during the first day are compared to the simulated ones. Again, absorber and cavity temperature are shown. The absorber temperature trend suggests a rather reliable behaviour: the water withdrawal is described quite well, having a considerable impact on the absorber temperature. In contrast, the cavity temperature is affected by a drastic temperature drop in the model, that is not completely realistic if compared to the actual temperature. This phenomenon could mean that the physical inertia of the simulated system should be reconsidered, especially in the cavity component when the water flow is of this magnitude. Further simulations will show how the model's response changes when the water flow decreases.

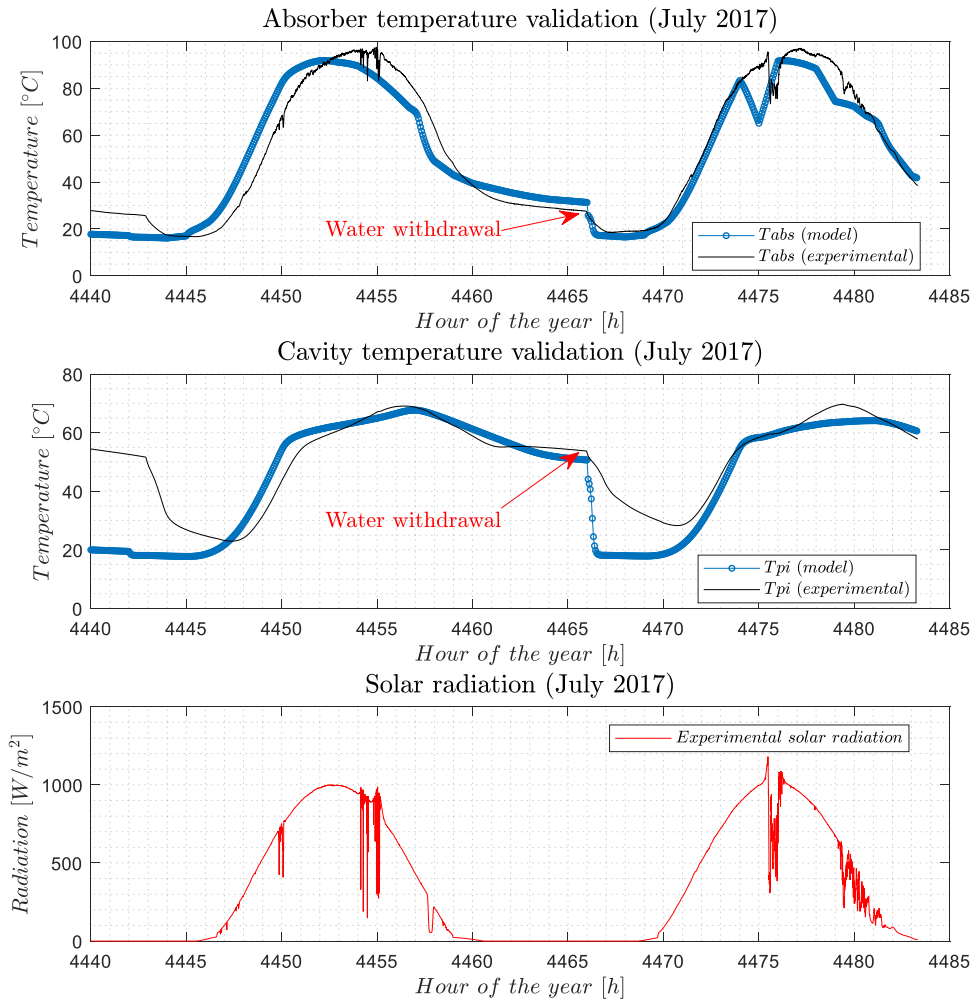


Figure 5-17. Absorber (T_{abs}) and cavity (T_{pi}) temperature during water withdrawal

However, having a look to the water temperature at the pipeline outlet (Figure 5-18), the model simulation is pretty close to reality. The withdrawal period is highlighted by the red rectangle, inside which actual and simulated temperature are similar. It is important to point out that outside the withdrawal region the two temperatures greatly differ due to a simulation issue that does not allow to have a constant water flow in the pipeline equal to zero during the day. For this reason, the system was modelled having a constant water withdrawal flowing in the pipeline very close to zero (around $10e^{-4}$ l/min) even when an actual withdrawal was not scheduled, in order to avoid computational issues. It has been verified that the result of this choice does not affect the global energy performance of the model but is obviously produces very high water temperatures at the outlet, as you can notice from the picture below. Therefore, what is relevant for our model validation is just the temperature trend inside the red area, where the simulated waterflow faithfully reflects the real one. Focusing on that region simulated results are quite satisfactory and very close to reality.

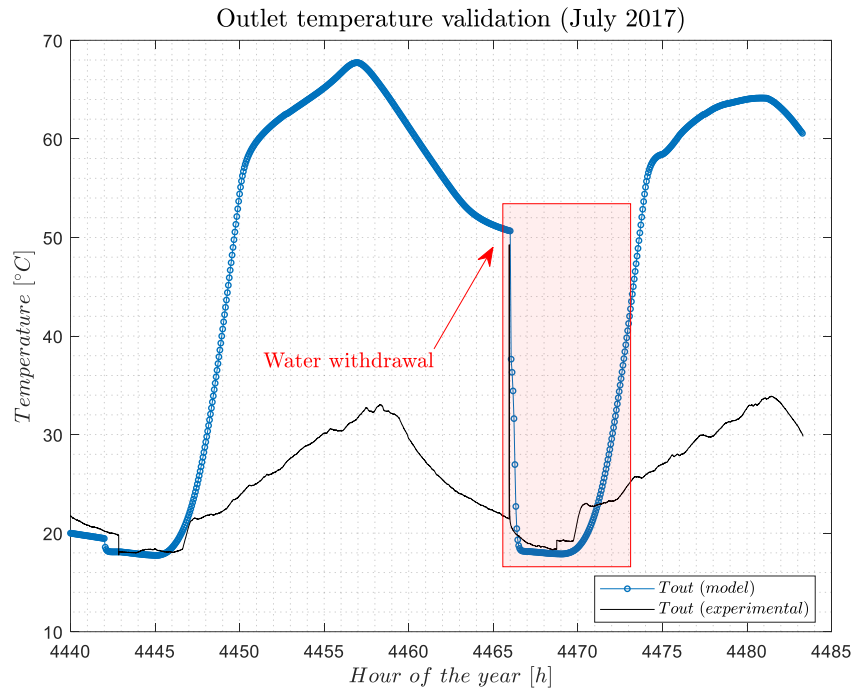


Figure 5-18. Water temperature at the outlet

Same set of validation experiments was carried out for a different period of the year, during winter condition in February 2018. Figure 5-19 shows again absorber (T_{abs}) and cavity (T_{pi}) temperature comparison between simulated and real data. A typical week has been taken into consideration, partly sunny and sometimes cloudy. As can be seen from the results obtained, due to very low external temperature condition, the PCM cavity never reaches the double phase region, involving just sensible heat stored in the cavity. Moreover, keeping the storage in the solid phase, heat transfer involves only conduction, with an almost constant value of specific heat. In these simplified conditions the model seems to provide results very similar to the real ones, especially for the cavity temperature, where simulated and real temperature are almost the same. Model's response to the solid phase state is very accurate, both with constant and discontinuous solar radiation, suggesting a reliable response during interrupted heating and cooling phases. Comparing the results obtained during previous simulations in summer conditions is clear that the main weak point of the model is the phase change region, where the thermal behaviour of the cavity is harder to describe. Surely, further investigations must be dedicated to this aspect.

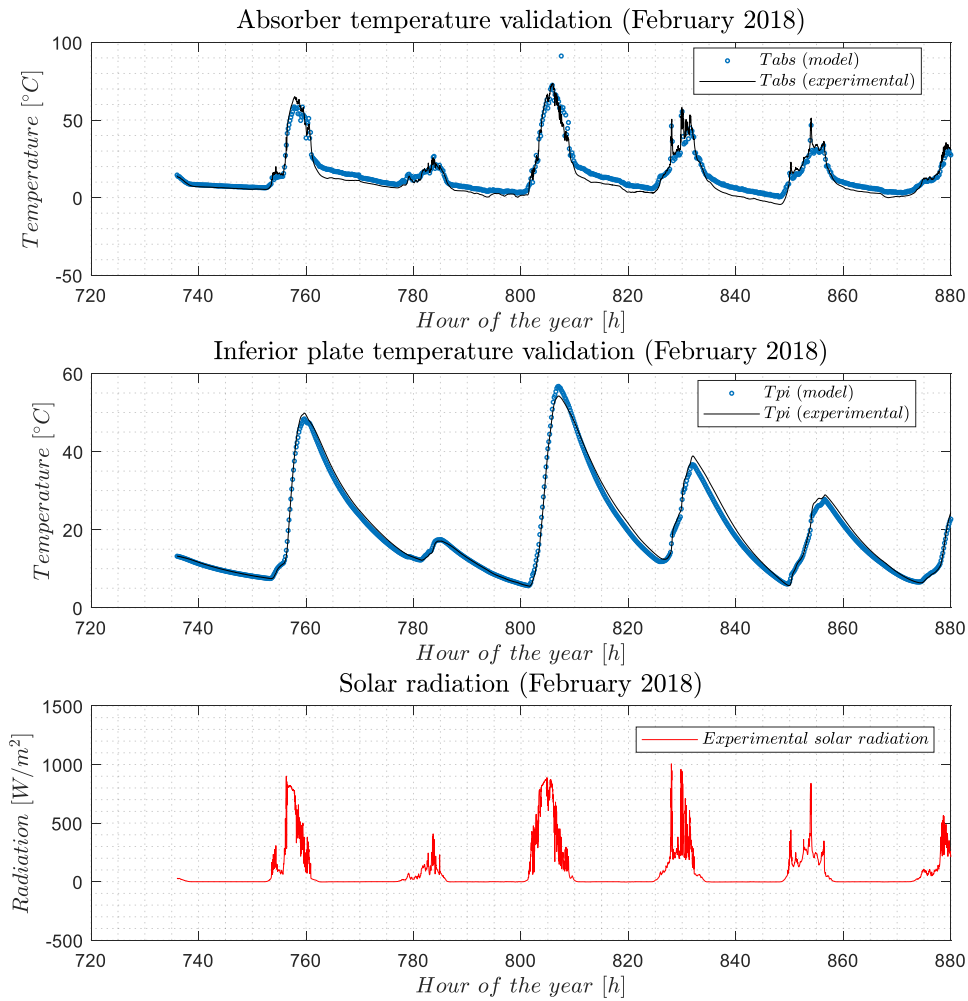


Figure 5-19. Absorber (T_{abs}) and inferior cavity plate (T_{pi}) temperature simulation in February 2018

Later, a short water withdrawal was experimentally tested and then simulated. Unlike what was done during the summer, a smaller flowrate was preferred, since the availability of stored heat was considerably smaller. Also, the withdrawal time has been reduced to around 30 minutes in the middle of the day, when the cavity reaches relatively high temperatures to carry out the withdrawal of water. Figure 5-20 summarizes the simulated trends for absorber and cavity temperature, providing a good model response in withdrawal conditions too. Water flowrate is also depicted in the picture by the dashed black line. Its trend comes from the real data collected in the acquisition system that have been implemented in the model as an input parameter, providing the actual flowrate to perform calculations. As already mentioned above for normal operation simulation, even in this case February simulation results better describe the real system operation.

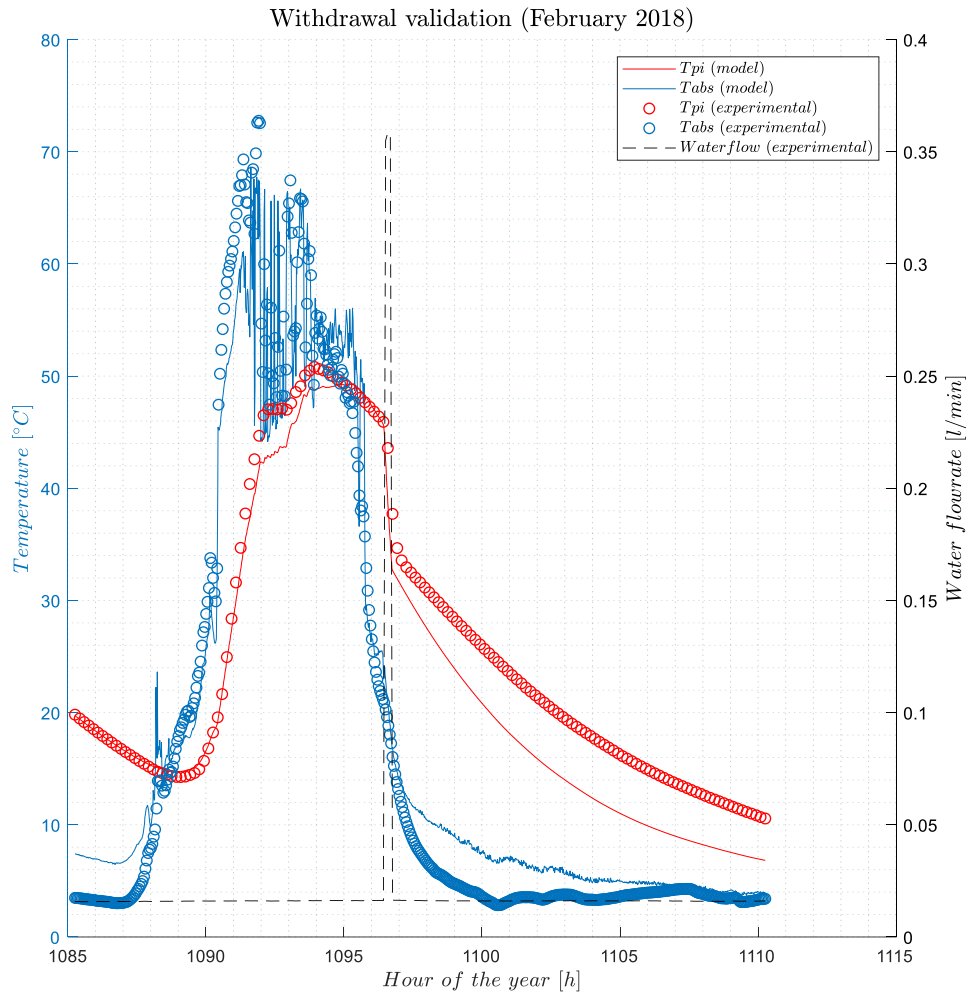


Figure 5-20. Water withdrawal simulation detail during February 2018

To conclude this validation section, we could say that the mathematical model represents quite well the real system operation, both in normal condition and during water withdrawal. Some inaccuracies may occur during the double phase region, when the phase change material inside the cavity passes through the melting phase. However, sub cooling phenomenon as well as interrupted heating and cooling seem to have been considered pretty well in the development of the model, giving reasonable results when they occur. As mentioned before, a better understanding must be dedicated to the phase change material thermal properties, not just from the performance characterization point of view, since they have already been largely studied, but in relation with the geometrical case where it has been placed.

5.3 Model energy performance

Once the model has been validated and its stability proved, an annual simulation was run, with the aim of evaluating global energy performances of the

prototype along the year. To perform this simulation different inputs data were required. For instance, the actual solar radiation as well as the external temperature, collected on-site by the data acquisition system and used in the validation process as input values are now replaced by typical mean meteorological data from a weather station close to Chambéry, France, where the experimental study was carried out. Furthermore, the cold water temperature at the DHW inlet is no longer supplied by the thermocouple placed in the prototype and used for the experimental session. The new input value is provided by the following table, that considers a monthly mean value for water coming from the French national network.

Table 5-10. Cold water monthly temperatures from the network

<i>Month</i>	<i>Temperature [°C]</i>
<i>January</i>	7,20
<i>February</i>	7,20
<i>March</i>	8,50
<i>April</i>	10,70
<i>May</i>	13,30
<i>June</i>	15,50
<i>July</i>	16,80
<i>August</i>	16,80
<i>September</i>	15,50
<i>October</i>	13,30
<i>November</i>	10,70
<i>December</i>	8,50

Finally, the daily DHW requirements are defined by two 30 l/h withdrawals during the day: the first from 6 a.m. to 8 a.m., and the second between 3 p.m. and 5 p.m. The waterflow is therefore set to the constant value of 0,5 l/min providing the total amount of 120 litres per day. A three-way valve, already mentioned in “*DHW heat exchanger*” section, limits the water outlet temperature to 55°C mixing the hot water produced by the ICS with cold water from the network. This simple solution provides considerable energy savings avoiding hot water production over 55°C, unusable for domestic purposes.

The time step used for the annual simulation is 30 seconds.

5.3.1 Evaluation parameters

Some energy parameters were used to evaluate the ICS performances along the year. Two most representative dimensionless parameters have been used to give an overall view of the prototype performances. The first one is represented by the solar saving fraction f_{SOLAR} , defined by the ratio between the amount of

useful energy provided by the solar system and the total energy demanded by our DHW application:

$$f_{SOLAR} = \frac{E_{USEFUL}}{E_{DEMAND}}$$

Being a seasonal parameter, solar fraction has been computed monthly, in order to show the performance trend during the year. Useful energy has been calculated from the temperature difference across the inlet and outlet of the DHW pipeline, considering the proper waterflow in related to the 3-way valve operation:

$$E_{USEFUL} = \int_{t_{in}}^{t_{end}} (\dot{m}_w \cdot c_{p,w} \cdot (T_{out} - T_{in})) dt$$

In contrast, the amount of demanded energy was computed taking into account a supply temperature equal to 55°C with the total flowrate (50 litres per hour for a total daily duration of 4 hours):

$$E_{DEMAND} = \int_{t_{in}}^{t_{end}} \left(\frac{\dot{m}_w}{c_{3WV}} \cdot c_{p,w} \cdot (55 - T_{in}) \right) dt$$

In this case, water flowrate considered is divided by the coefficient c_{3WV} that regulates the 3-way valve operation: it is equal to 0 when there is no water flowing inside the collector pipeline and equal to 1 when all the flowrate supplied to the user is going through the collector.

The second parameter chosen is the stored energy rate, defined as the energy stored in the cavity divided by the incident solar radiation on the absorber surface:

$$f_{STORED} = \frac{E_{STORED}}{E_{SOLAR}}$$

Where the stored energy has been computed ad-hoc for the project as the energy transferred from the absorber to the cavity by means of the heat pipes:

$$E_{STORED} = \int_{t_{in}}^{t_{end}} (\#_{HP} \cdot U_{HP} \cdot \Delta T_{HP}) dt$$

With $\#_{HP}$ indicates the number of heat pipes installed and U_{HP} represents the global heat transfer coefficient [W/K], whose properties have already been discussed. Regarding ΔT_{HP} , it is supposed to be the temperature difference between the evaporator and condenser section of the heat pipes. However, for simplicity reasons, those temperature have been set equal to the absorber and front cavity temperatures, respectively:

$$\Delta T_{HP} = (T_{eva} - T_{cond}) = (T_{abs} - T_{pi})$$

Finally, the incident solar radiation energy is computed from the solar radiation and the absorber surface:

$$E_{SOLAR} = \int_{t_{in}}^{t_{end}} (E \cdot S) dt$$

5.4 Annual performance of the prototype

After validating the numerical model through the use of experimental data and after having defined the main parameters for the evaluation of its performances in the previous paragraph, a series of numerical simulations were launched simulating the prototype's behaviour over a whole year. To complete this simulation, new input parameters have been defined that are slightly different from those selected for model validation simulations.

5.4.1 Annual boundary conditions

First of all, the city of Chambéry was set up as the location of the simulation, through the implementation of the corresponding climatic data coming from a nearby climate station. Among the climatic data used as inputs are the external temperature, the direct and diffused radiation, the height and the solar azimuth. Table 5-11 collects the data used by the model, recorded with an hourly rate starting from the first of January until December 31st. The climatic data are represented by average values relative to previous years.

Table 5-11. Climatic annual input data

<i>Data</i>	<i>Unit</i>
<i>External temperature</i>	°C
<i>Direct radiation</i>	W/m ²
<i>Diffuse radiation</i>	W/m ²
<i>Solar height</i>	°
<i>Solar azimuth</i>	°
<i>Data timestep</i>	1 h
<i>Starting hour</i>	1:00 1 st January
<i>Final hour</i>	24:00 31 st December

Subsequently, a daily water withdrawal profile was defined for a total of 120 liters, divided into two withdrawal period, in the morning and in the evening, each for a duration of 2 hours. In this way, a maximum volumetric waterflow of around 0.5 l/min was ensured. Despite being a rather low value, this choice allowed first of all to have a simulation value similar to the one used in the model validation phase and secondly to extend the timestep of the simulation, which was set at 10 minutes, with a significant savings in terms of computational cost. Furthermore, the total amount of DHW produced, i.e. 120 liters, seems to be a reasonable value, keeping in mind that in a possible future installation the number of collectors should be at least 3 units in order to meet the daily needs of a single-family home. Fig shows the daily water withdrawal over the whole year.

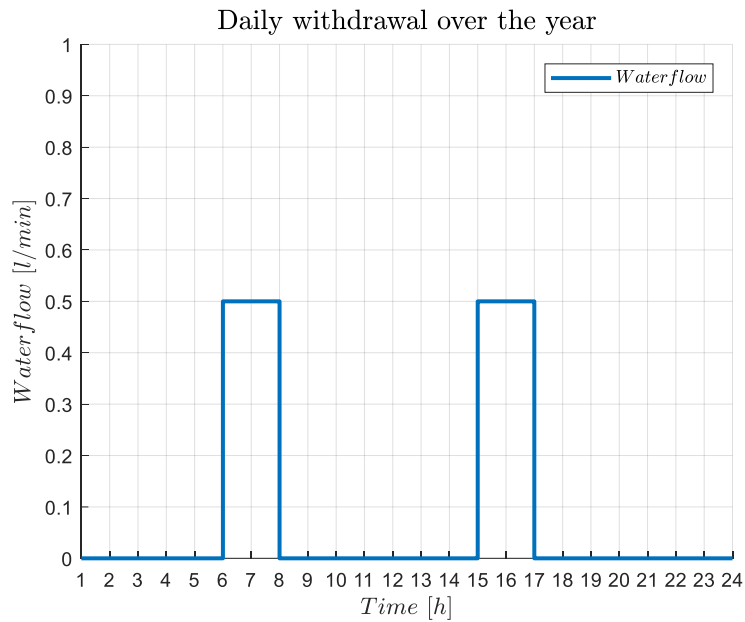


Figure 5-21. Daily water withdrawal for the annual simulation

Finally, as already mentioned in the previous paragraphs, the maximum DHW production temperature has been set at 55 °C, simulating the installation of a three-way valve able to mix the heated water from the collector with the colder one coming from the network, thus avoiding any energy waste due to the production of excessively hot water, unusable for domestic applications. Water withdrawn from the network had the average temperature provided in Table 5-10.

The timestep adopted for the annual simulation was 10 minutes.

5.4.2 Annual simulation results

Figure 5-22 shows the cumulative values of the main energy vectors involved in the system as defined in the section 5.3.1: the useful energy, the energy demanded, the stored energy and the solar energy.

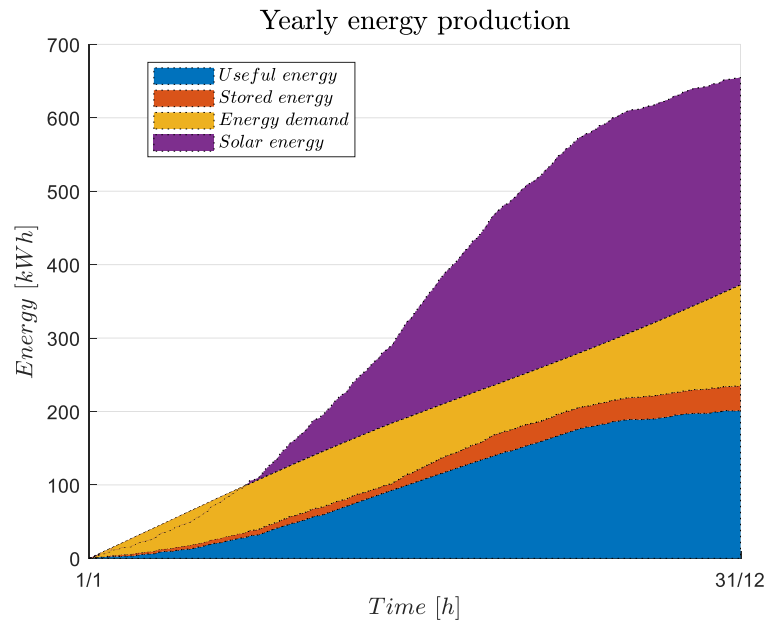


Figure 5-22. Yearly energy production

The values shown are referred to a single collector with an absorber surface equal to 0.5 m^2 . It can immediately be noted that the useful energy produced by the prototype (blue area) is not able to fully meet the annual demand (yellow area). However, it is interesting to note that the gap between stored and useful energy is relatively small (orange area), indicating that most of the stored energy is used for the actual production of DHW.

From this annual simulation it can also be estimated the annual productivity of the prototype, equal to 402.2 kWh/m^2 . This result indicates that the collector in question is relatively well placed in terms of productivity compared to conventional solar water heaters.

Starting from these values, referring to the entire year, the monthly values were extrapolated. Figure 5-23 shows the trend of the useful energy, the stored energy and demanded energy for all the months of the year.

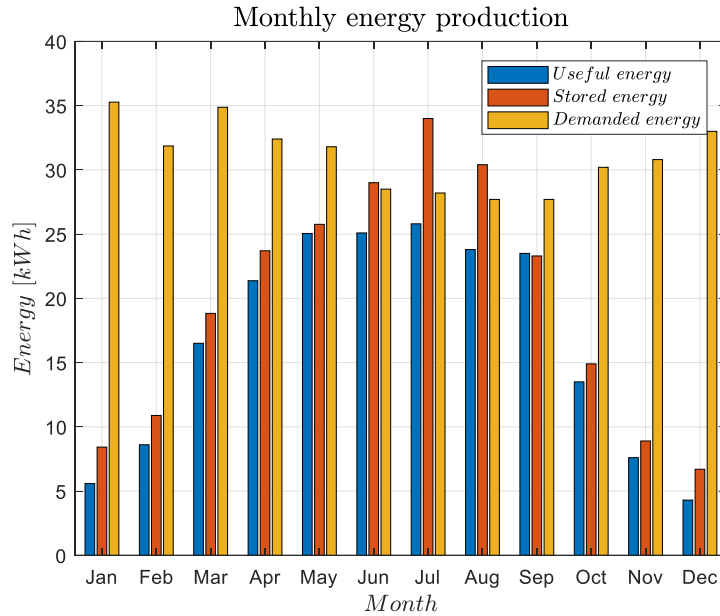


Figure 5-23. Monthly energy values

As you can see, the useful and the stored energy increase during the summer months, while the energy demanded has an opposite trend.

Referring to these monthly values, the solar fraction f_{SOLAR} was evaluated and shown in Figure 5-24, as defined in the previous section.

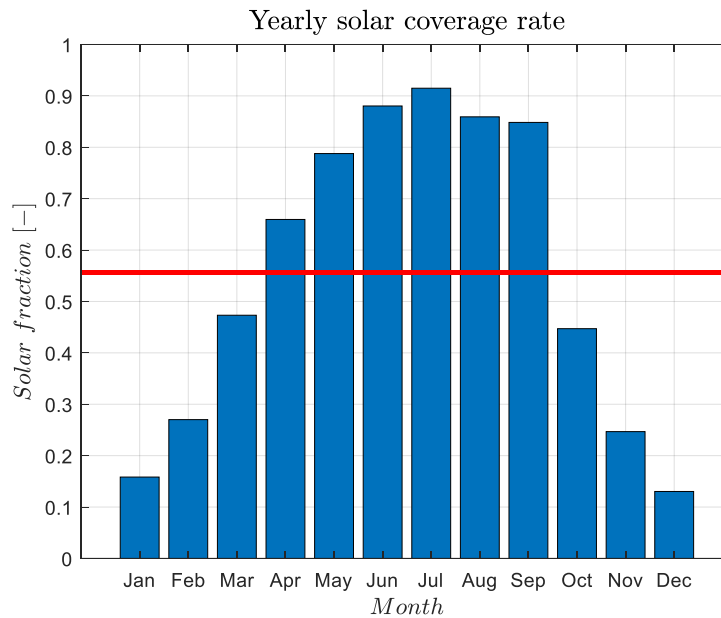


Figure 5-24. Solar fraction

The average solar coverage rate (red line) is equal to 56% and reaches a maximum value of about 90% in July, during which the collector is able to satisfy

almost entirely the demand for DHW. The lowest value is instead recorded in the month of December, where the solar fraction does not exceed 15%.

With the same monthly approach, the stored fraction f_{STORED} was evaluated. Figure 5-25 collects the monthly trend of f_{STORED} .

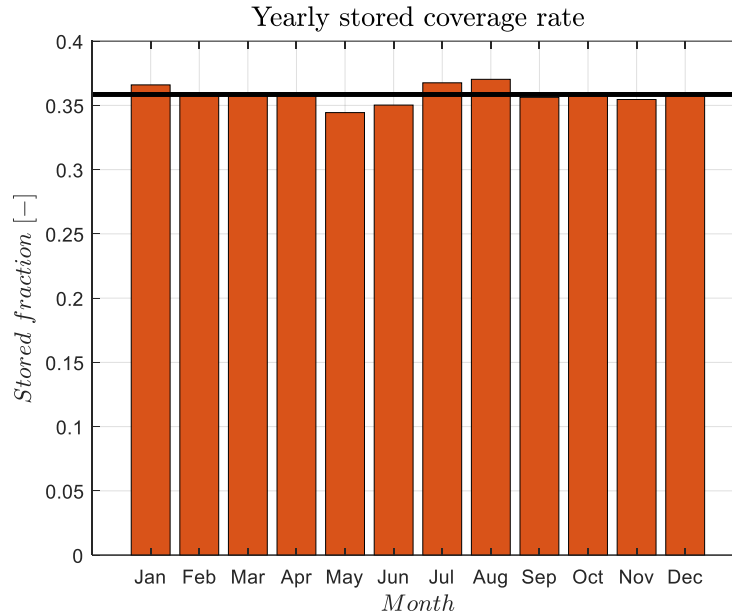


Figure 5-25. Stored fraction

From this graph we can see how the fraction of energy accumulated during the year is rather constant, indicating that this value does not depend on solar activity. However, the average value, equal to 35.9% (black line), indicates that only one third of the solar radiation is effectively stored inside the prototype. This value shows that the prototype still has room for improvement, especially regarding the absorber and the storage section.

Finally, by shifting attention to the dynamic behaviour of the model, two days belonging to the winter season and the summer season were taken into consideration. The model variable that has been analysed is the front plate cavity temperature (T_{pe}), that is the surface of the PCM storage in direct contact with the domestic hot water exchange coil. The trend of this temperature is interesting since it is very variable when a water withdrawal occurs.

Figure 5-26 represents the trend of the T_{pe} temperature during June 4th, a typical day of the summer season. The two DHW withdrawals, manually set between 6:00 and 8:00 and 15:00 and 17:00 are clearly visible in the graph, causing a lowering of the temperature of the front plate. In the figure it can also be noticed the areas where the PCM phase change occurs, at different temperatures depending on how the process takes place (solidification or liquefaction). Moreover, it can be seen how the morning withdrawal occurs when the PCM is in the solid phase, while during the afternoon the PCM is in the liquid phase. As already discussed previously, the physical state of the PCM

affects the heat exchange between the cavity and the water, undergoing a greater temperature drop when the material exchanges in the liquid phase.

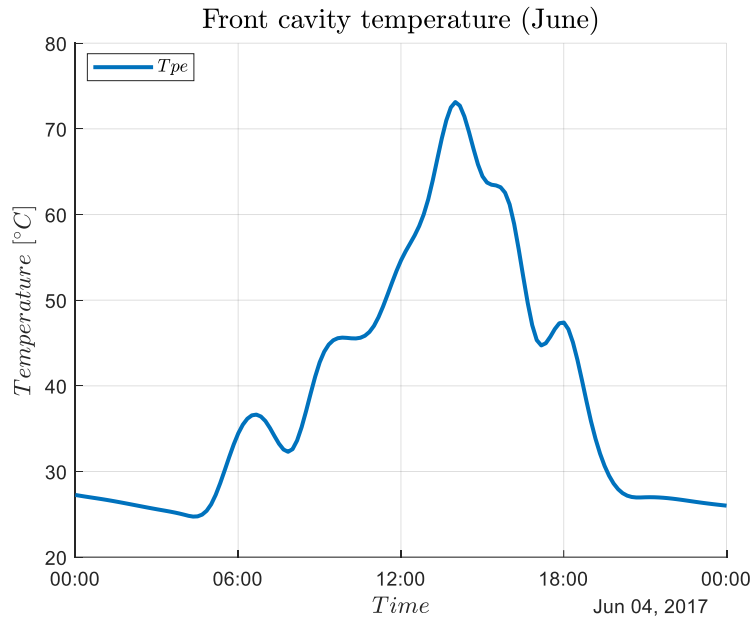


Figure 5-26. T_{pe} trend on June 4th (model simulation)

On the other hand, taking into consideration a typical winter day like January 13th (Figure 5-27), the T_{pe} trend undergoes some modifications. At 6:00 am, in fact, the PCM is not yet able to provide useful energy for DHW production, since its temperature is lower than 10 °C. However, the afternoon withdrawal can provide a fair amount of energy, even if the poor presence of solar energy does not allow the cavity to maintain temperatures above 20 °C at the end of the day.

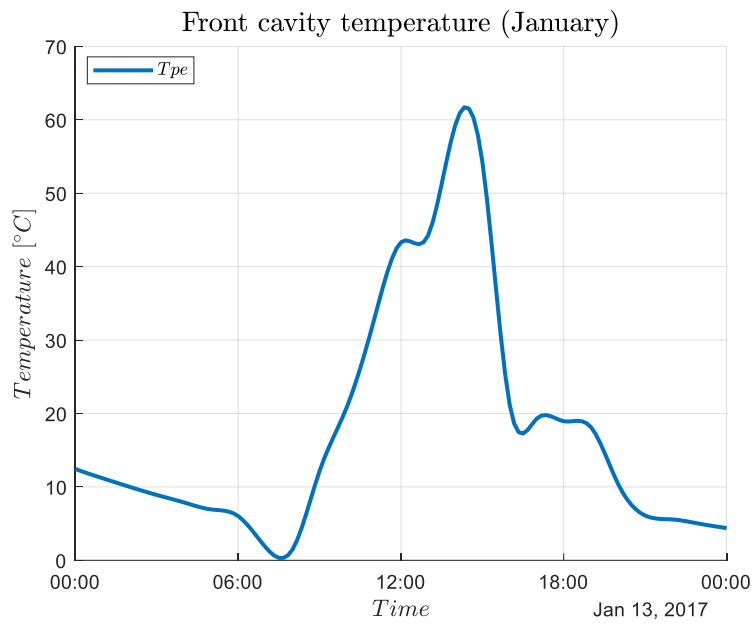


Figure 5-27. T_{pe} trend on January 13th (model simulation)

Chapter 6

6 Conclusion

In the previous chapters an innovative integrated collector storage (ICS) with a PCM storage has been examined. Starting from a detailed literature analysis, included in Chapter 1, a prototype of ICS has been realized with unique characteristics, combining a flat plate absorber, heat pipes and a storage section with phase change material (PCM) inside the same casing. From the analysis of the state of the art, a system that is currently the subject of scientific research combining all these elements within it has not been found. For this reason, the results contained in this work are unique in their kind, even if comparable with systems that adopt similar engineering solutions.

The aim of the project was to study the effectiveness of this system in the production of domestic hot water (DHW). Given the rather small size of the prototype under examination (0.5 m^2 of absorber surface), the device is aimed at a medium-small user, possibly domestic.

After explaining the working principle of the prototype and analysing in detail the roles performed by the individual components (Chapter 2), a test bench was created to test the energy performance of the device in an external environment. Several tests have been developed to verify the correct functioning of the prototype, both in terms of standard working conditions and under thermal stress conditions. The prototype showed no major signs of malfunction such as PCM leakages. After being normally daily loaded, the temperatures reached in the cavity are limited, which is good for the durability of the system (including periods without any water withdrawals). Incident solar energy is well transmitted to the storage: the heat pipes play their role as expected and the thermal diode effect is also validated (the absorber temperature does not rise abnormally during the night). A small difference in temperature is observed between the two sides of the cavity, confirming a good efficiency of the honeycomb structure to transfer heat.

The results of this first experimental phase, which was conducted during the spring and summer months of the year 2017, were collected in Chapter 3 and showed a behaviour in operation as expected. It has been shown that the temperature rise of such a storage is comparable and sometimes even faster than conventional water storage, reaching $7.65 \text{ }^\circ\text{C/h}$ when the PCM is in a solid state. However, the analysis of the results has revealed some problems related to thermal losses of the prototype, due to design errors. As discussed in Section 3.3.4, thermal losses due to external dispersion reach 80 W/m^2 .

A careful analysis of this problem has been the subject of Chapter 4, where the prototype has gone through a series of experimental tests inside an indoor laboratory to make some changes and improve its performance. From a thermographic analysis (section 4.1) some metallic supports in the casing have been identified responsible for the rather high thermal losses. Therefore, by

modifying some structural components it was possible to reduce thermal losses by about 50%. These changes were followed by a second series of experimental outdoor tests that confirmed the effectiveness of the changes made and also gave the opportunity to test the prototype in winter conditions, between January and March 2018.

The whole experimental phase was also associated at the same time by the development of a mathematical model through the use of the EES simulation software. The prototype was modelled using an electrical analogy approach (Chapter 5). Furthermore, with regard to phase-change material, following a differential scanning calorimetry (DSC) analysis, a model based on a mathematical relation presented in the literature was implemented. The model was then validated by means of the experimental data collected and finally allowed to simulate the annual behaviour of the prototype. The results obtained show an average solar fraction of 56%, totally in line with what offered by commercial products. Considering the annual performance, the model simulation registered a productivity equal to 402.2 kWh/m², a comparable result with traditional systems. The dynamic behaviour of the prototype is well predicted by the model, even if some improvements can be made, especially on the model response when a water withdrawal occurs. Other particular cases such as sequences of days with strong variations in solar radiation lead to large errors. Furthermore, the heat pipe section might be modelled dynamically allowing a more detailed phenomena simulation.

From the analyses carried out in this study, an innovative and certainly very versatile solar collector has emerged. The great advantage of this ICS is the simplicity of use and installation, which does not require any auxiliary elements. The system is presented as a “ready-to-use” solution whose only need is to be connected to a water network. The experimental results, supported by mathematical simulations, have shown on the one hand the effectiveness of the engineering choices adopted, on the other hand a high potential for a future improvement and optimization of the prototype.

The energy efficiency of the system is still slightly lower than that recorded in similar systems (Figure 3-9) and the solar contribution is not exploited to its full potential, especially when the radiation involved is high (Figure 3-8). In general, being the first of its kind, this type of ICS has all the characteristics to be compared with traditional systems.

6.1 Possible implementations

As already anticipated in section 2.3, the ICS studied represents a special case study mainly made for experimental purposes. During all the experiments that involved withdrawals of water from the network for DHW production, the hot water was discharged without being effectively used by a user. For experimental purposes related to the purpose of this study, the prototype was subjected to individual tests that verified its correct operation and performance. However,

what is expected from possible future applications is the implementation of the prototype in a more complex system.

First of all, it must be integrated into a building's water network, so that it can work in combination with the traditional systems installed and increase the percentage of energy supplied by renewable sources. Many regulations of European states are in fact increasing the share of renewable energy produced within buildings. As for Italy, Legislative Decree 28/2011, extended by Decree Law 244/2016, established that the energy needs for DHW production should be 50% covered by renewable sources. For this reason, the integration of new technologies such as the prototype studied within traditional systems is of fundamental importance and could be considered for future developments. Moreover, controlling and regulating a single device inside a complex HVAC system might lead to very different performance from those just studied, referred to the single disjointed element.

Secondly, what distinguishes a possible future implementation by the case examined is a larger installation with more than one ICS. As for a typical single-family home, the absorber surface should be at least 1.5 m². This therefore entails having a DHW generation system made up of two or more collectors grouped together in the same system, as already shown in figure Figure 2-11.

All these considerations, which shift the focus no longer on the single ICS, but on a larger and more complex system, certainly represent an equally vast subject of study that would however be necessary in order to validate the prototype from the commercial point of view. The object of the study just proposed was purely energetic and addressed to the single element, but in the future the implementation of such a prototype will have to be validated within a more complex system.

6.2 Future improvements of the ICS

From this study, many choices made during the design phase have been validated in a positive way. For example, the behaviour of heat pipes as a thermal diode has been confirmed experimentally by the tests in section 3.3.1. The decision to use the PEG6000 as a phase change material was also perfectly in line with what was expected. On the other hand, some choices turned out to be rather disadvantageous. This was certainly the case of metal supports that connected the storage cavity with the external casing, generating a detrimental heat loss.

Overall, the prototype has met most of the expectations, revealing itself as a reliable and efficient ICS. At the same time, however, the experiments carried out have highlighted numerous aspects on which further analyses and possible improvements can be carried out.

First of all, some considerations should be made on the heaviness of the prototype. Although it has initially been designed as a lightweight and easily integrable device, the weight of the prototype is quite high. This does not make it absolutely easy to handle and could also negatively affect possible future architectural installations. The main cause is surely due to the use of metal for the external casing and for most of the internal supports. In addition to weighing

down the prototype, this choice penalizes the heat loss, as previously studied. A possible improvement therefore foresees the use of lighter materials, where possible.

A second aspect that deserves a possible redesigning process is the flat-plate absorber. In fact, comparing the thermal performances of the absorber used with those on the market, the results are rather poor. As can also be seen from the efficiency curve of the collector shown in Figure 3-9, the optical efficiency of the glass panel, around 0.6, is quite low. The replacement with a more performing glass cover and a high efficiency absorber could make the prototype even more competitive with those on the market, reaching absorber temperatures around 130-140 °C.

A similar consideration can also be applied to the DHW exchanger, constructed as a classic copper coil soldered directly onto the front plate of the storage cavity. The thermal exchange between water and PCM could be improved with the installation of a coil that wraps the storage cavity on all sides, not only on the front. In this way, in addition to having a larger exchange surface, a temperature gradient of the PCM inside the cavity is avoided, since the heat is extracted more evenly. The problem of creating strong differences in temperature inside the cavity could in fact lead to structural deformations of the cavity in the long run, since some areas of the cavity might have PCM in solid state and others in liquid state, especially with temperatures around the transition phase.

Lastly, even the heat pipes, although performing the effect of a thermal diode, could be revisited and replaced with more performing ring heat pipes and no longer U-shaped. The solution of tubular U-shaped heat pipes is also difficult to implement. It may be easier to use “roll-bond” heat pipes to achieve better performances and a global cost certainly lower. Furthermore, a vertical ICS might be considered, because it could be easier to implement (evaporator below the condenser) compared to the actual prototype, especially when considering wall installations. This configuration can be quite relevant in order to free up the rooftop space for photovoltaic production.

Another solution of possible interest could be represented by the coupling of a vacuum tube absorber in direct contact with the storage cavity, bypassing the heat pipe section. Also, a configuration that does not involve the insulation layer on the front face seems relevant because of its simplicity compared to our configuration with heat pipes. Nevertheless, this option seems oriented for areas with warm climates. It is also possible to use transparent insulation to reduce the heat losses between the front face of the storage cavity and the outside environment.

The solutions that can be adopted to further improve this new concept of ICS studied are many and at the same time stimulating. Starting from this work, there are real prospects that can lead to the manufacturing of commercially achievable ICS.

References

- Anant, Shukla, Buddhi, D. and Sawhneya, R.L. 2009.** Solar water heaters with phase change material thermal energy storage medium: A review. *Renewable and Sustainable Energy Reviews*. 2009, Vol. 13, 8.
- Beamex. 2007.** Thermocouple Cold (Reference) Junction Compensation. *Calibration White Paper*. 2007.
- Colombo, Diego. 1984.** Le Termocoppie: principio di funzionamento, produzione e impiego. *Università degli Studi di Trento*. [Online] 1984. [Cited: 16 2018.]
[http://www.ing.unitn.it/~colombo/Termocoppie/3\)Funzionamento.htm](http://www.ing.unitn.it/~colombo/Termocoppie/3)Funzionamento.htm).
- D'Avignon, Katherine and Kummert, Michaël. 2016.** Experimental assessment of a phase change material storage tank. *Applied Thermal Engineering*. 2016, 99.
- De Winter, F. 1991.** *Solar collectors, energy storage, and materials*. Massachusetts : The MIT press, 1991.
- Delcroix, Benoit and Michaël Kummert, Ahmed Daoud. 2015.** Thermal behavior mapping of a phase change material between the heating and cooling enthalpy-temperature curves. *Energy Procedia*. 2015, 78.
- Ditmars, D.A., et al. 1982.** Enthalpy and Heat-Capacity Standard Reference Material: Synthetic Sapphire from 10 to 2250 K. *Journal of Research of the National Bureau of Standards*. 1982, Vol. 87, 2.
- Esen, Mehmet and Esen, Hikmet. 2005.** Experimental investigation of a two-phase closed thermosyphon solar water heater. *Solar Energy*. 2005, 79.
- Fraisse, Gilles, et al. 2017.** *Etude numérique et expérimentale d'un nouveau concept de capteur solaire thermique auto-stockeur à changement de phase*. 2017.
- Haillot, D., et al. 2011.** High performance storage composite for the enhancement of solar domestic hot water systems - Part 1: Storage material investigation. *Solar Energy*. 2011, Vol. 85.
- Haillot, D., et al. 2012.** High performance storage composite for the enhancement of solar domestic hot water systems - Part 2: Numerical system analysis. *Solar Energy*. 2012, Vol. 86.
- IEA. 2018.** *Energy and CO2 emissions in the OECD*. 2018.
- . 2018.** *Energy Storage with Energy Efficient Buildings and Districts: Optimization and Automation*. 2018.
- Instruments, TA. 1998.** Guidelines for Quantitative Studies. *DCS 2920 Operator's Manual*. New Castle, DE : s.n., 1998.
- Kalogirou, Soteris A. 2006.** *Solar Collectors and Applications*. 2006.
- Komarnicki, P., Lombardi, P. and Styczynski, Z. 2017.** *Electric Energy Storage Systems: Flexibility Options for Smart Grids*. s.l. : Springer, 2017.
- Kousksou, T., et al. 2011.** PCM storage for solar DHW: From an unfulfilled promise to a real benefit. *Solar Energy*. 2011, Vol. 85, 9.

- Kuznik, Frédéric, Virgone, Joseph and Roux, Jean-Jacques. 2006. Energetic efficiency of room wall containing PCM wallboard: A full-scale experimental investigation. *Energy and Buildings*. 2006.
- . 2008. Energetic efficiency of room wall containing PCM wallboard: A full-scale experimental investigation. *Energy and buildings*. 2008, pp. 148-156.
- Nemec, Patrik, Čaja, Alexander and Malcho, Milan. 2011. Thermal Performance Measurement of Heat Pipe. 2011.
- REN21. 2014. *Renewables 2014 - Global Status Report*. Paris : s.n., 2014.
- Robinson, Brian S. and Sharp, M. Keith. 2015. Reducing unwanted thermal gains during the cooling season for a solar heat pipe system. *Solar Energy*. 2015, 115.
- Robinson, Brian S., et al. 2013. Heating season performance of a full-scale heat pipe assisted solar wall. *Solar Energy*. 2013, 87.
- Robinson, Brian, et al. 2013. Heating season performance of a full-scale heat pipe assisted solar wall. *Solar Energy*. 2013, 87.
- Rudy, Julie and Manuse, Cindy. 2016. *Modélisation numérique d'un caloduc pour un prototype de capteur solaire thermique à changement de phase*. s.l. : Ecole d'Ingénieurs Polytech Annecy Chambéry , 2016.
- Sadhishkumar, S. and Balusamy, T. 2014. Performance improvement in solar water heating systems — A review. *Renewable and Sustainable Energy Reviews*. 2014, 37.
- Serale, Gianluca, Fabrizio, Enrico and Perino, Marco. 2015. Design of a low-temperature solar heating system based on a slurry Phase Change Material (PCS). *Energy and Buildings*. 2015, Vol. 106.
- Smil, V. 1991. *General energetics: energy in the biosphere and civilization*. New York : John Wiley & Sons, 1991.
- Smyth, M., Eames, P.C. and Norton, B. 2006. Integrated collector storage solar water heaters. *Renewable and Sustainable Energy Reviews*. 2006, Vol. 10.
- Souza, Jeronimo V.D., et al. 2014. Experimental study of a partially heated cavity of an integrated collector storage solar water heater (ICSSWH). *Solar Energy*. 2014, 101.
- Susheela, Narasimhan and Sharp, M. Keith. 2001. Heat Pipe Augmented Passive Solar System for Heating of Buildings. *Journal of Energy Engineering*. 2001.
- TA Instruments. *DSC 2920 Differential Scanning Calorimeter*. New Castle : s.n.
- Tian, Y. and Zhao, C.Y. 2013. A review of solar collectors and thermal energy storage in solar thermal applications. *Applied Energy*. 2013, Vol. 104.
- United Nations, Department of Economics and Social Affairs, Population Division. 2017. *World Population Prospects*. New York : s.n., 2017.
- Vikram, D., et al. 2006. An improvement in the solar water heating systems using phase change materials. *Solar Energy*. 2006.

Appendix A

Thermocouples calibration

This paragraph will explain how the thermocouples installed in the prototype have been calibrated. Nevertheless, for sake of completeness, is better to explain the basic principles behind a thermocouple operation. Thermocouples installed in the prototype belong to the very common type K, made of Alumel and Chromel conductors. In a thermocouple, different conductive wires form an open circuit with two junctions at different temperatures. Having different temperatures at the junctions, an electromotive force is generated, due to Seebeck effect (Colombo, 1984). Thus, we will have an end of the thermocouple with a certain temperature T_1 , called hot junction, and another end at T_2 , cold junction. The electromotive force created at the cold junction is strictly related with the temperature difference between the junctions (Figure A-1).

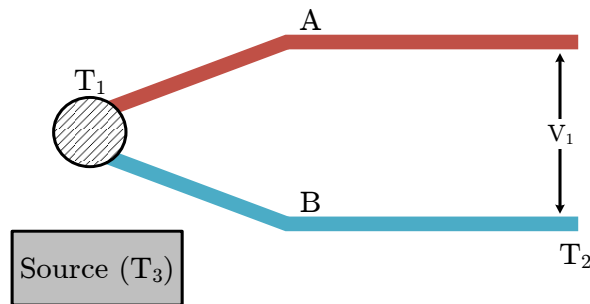


Figure A-1. Thermocouple simple scheme

However, to easily measure a voltage, the cold junction just described is connected to a pair of wires, usually made by copper, used to link the thermocouple with the voltmeter. Therefore, one of the junction is at the temperature that we want to measure, whereas the second one represents the reference junction with a different temperature (Figure A-2). The presence of copper wires does not affect the electromotive force by Seebeck effect. To move from the voltage value to the temperature measured at the hot junction, several tables with polynomial expression are usually provided by manufacturers. However, those tables refer to a standard cold junction temperature equal to 0°C .

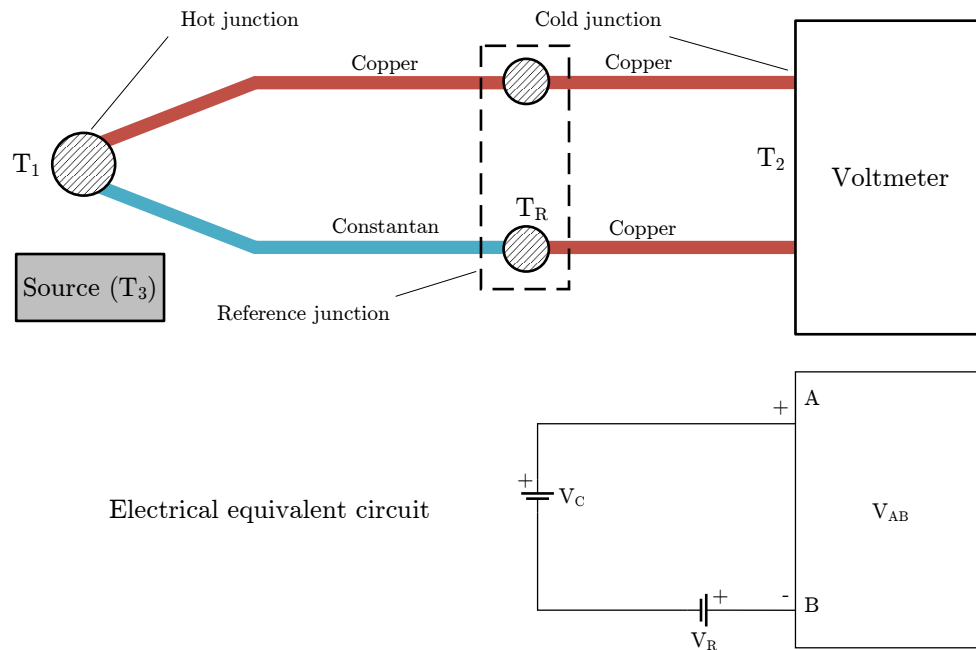


Figure A-2. Extra wires

In most cases, during standard measurement, the cold junction temperature is not equal to 0°C , making useless the use of manufacturers' tables. To solve this problem, we need to make a compensation, meaning that we have to know how the cold junction condition affects the electromotive force read by the voltmeter. To this end, three methods are possible (Beamex, 2007):

- 1) Keeping the cold junction at a known temperature;
 - 2) Introducing a new voltage balancing the fact that the cold junction temperature is different from 0°C .
 - 3) Evaluating the reference junction temperature.
- 1) In this specific case particular environmental conditions are set to maintain the cold junction temperature equal to the reference temperature of 0°C . What is practically done is a melting bath of ice and water. The main problem developing this method is that these conditions must be maintained constant, making this procedure not practical (Figure A-3).

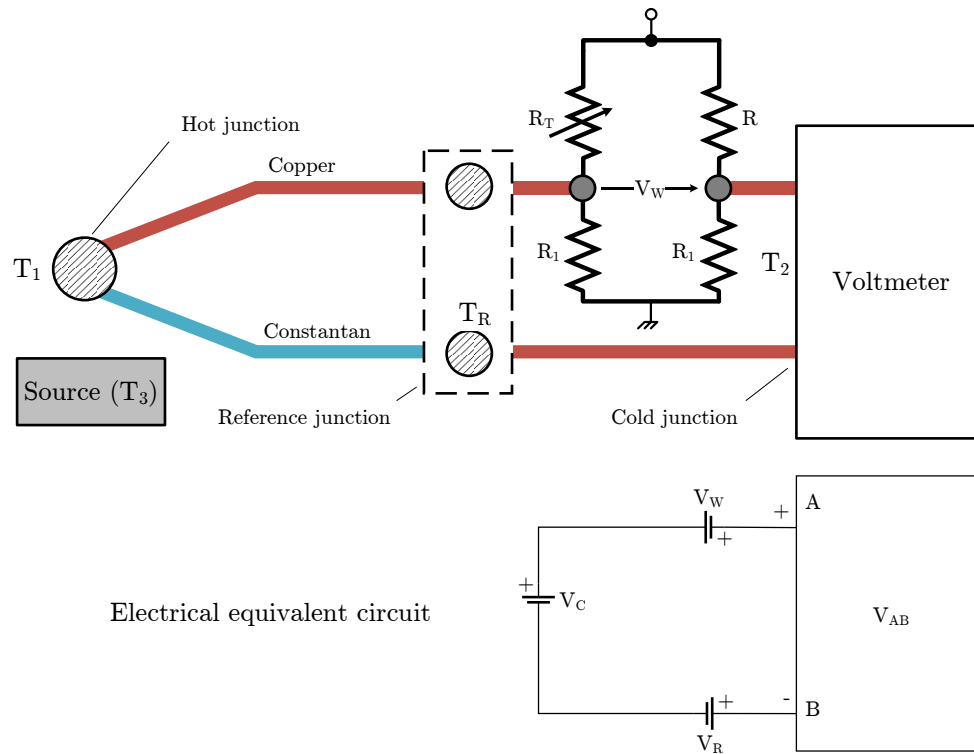


Figure A-4. Isothermal block circuit

- 3) If the cold junction is not at the reference temperature, the electromotive force registered at the voltmeter connections is given by:

$$E_\sigma = E_\sigma(T_1) - E_\sigma(T_2)$$

Where:

E_σ is the measured voltage;

$E_\sigma(T_2)$ is the voltage generated by the hot end;

$E_\sigma(T_1)$ is the voltage generated by the reference (or cold) junction.

This method has been chosen to collect temperature values in the analysed prototype.

To evaluate the actual voltage generated by the hot junction $E_\sigma(T_1)$ we need to know the voltage created by the cold junction. A way to find this value is to implement a secondary measurement to evaluate the cold junction temperature. Such measurement is usually performed using a separate sensor, like a thermoresistance (PT100 has been used in the prototype). In our case, the PT100 sensor directly tells us the temperature of the cold junction. However, what we need is a voltage value. Then, it is important to convert the measured temperature value using the tables or polynomial expressions provided by the manufacturer. For a K type thermocouple operating in a range of temperature from 0°C to 1372°C , $E_\sigma(T)$ is given by:

$$E_{\sigma}(T) = b_0 + \sum_{i=1}^n b_i(T)^i + c_0 e^{[c_1(T-126.9686)^2]} [\mu V]$$

Where:

$$\begin{aligned} b_0 &= -1.7600413686 \cdot 10^1 \\ b_1 &= +3.8921204975 \cdot 10^1 \\ b_2 &= +1.8558770032 \cdot 10^{-2} \\ b_3 &= -9.9457592874 \cdot 10^{-5} \\ b_4 &= +3.1840945719 \cdot 10^{-7} \\ b_5 &= -5.6075059059 \cdot 10^{-10} \\ b_6 &= +5.6075059059 \cdot 10^{-13} \\ b_7 &= -3.2020720003 \cdot 10^{-16} \\ b_8 &= +9.7151147152 \cdot 10^{-20} \\ b_9 &= -1.2104721275 \cdot 10^{-23} \\ c_0 &= +1.185976 \cdot 10^2 \\ c_1 &= +1.183432 \cdot 10^{-4} \end{aligned}$$

Thanks to this relation, $E_{\sigma}(T_2)$ has been computed and subsequently the $E_{\sigma}(T_1)$ voltage is calculated by the sum of the reference junction voltage with the measured one:

$$E_{\sigma}(T_1) = E_{\sigma} + E_{\sigma}(T_2)$$

The next step is to convert the voltage into a temperature value. To this end, the polynomial expression provided by the tables above is no longer adopted. Instead, to have a more accurate evaluation, each thermocouple used during the data collection has been calibrated before using a dedicated device (Figure A-5). A cylindrical metal rod is placed in an isolated water bath heated at a constant temperature. A certain number of thermocouples are then placed inside the metal rod, in dedicated holes. Moreover, a thermoresistance (PT100) measures the actual bath temperature. By considering average values of $E_{\sigma}(T_1)$ at different reference temperatures, forcing the hot junction temperature to reach several known values of temperatures in the water bath, a set of pair of points is collected. This allows to trace the behaviour of the temperature as a function of the voltage E_{σ} .

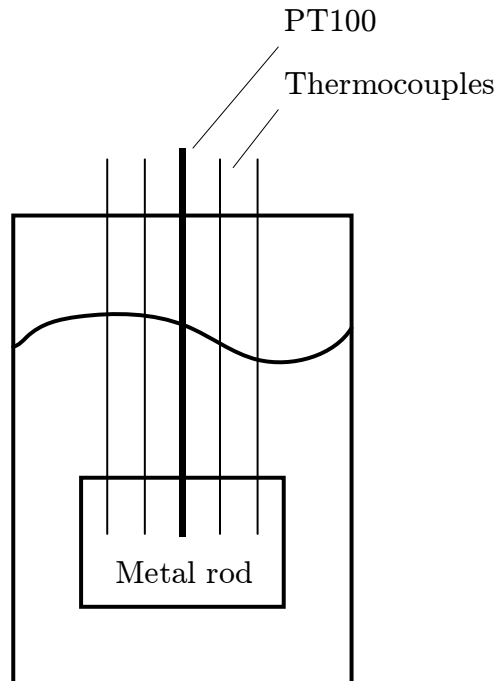


Figure A-5. Calibration system - scheme

This procedure is then repeated for each thermocouple, describing its specific behaviour. From the points collected, an analytical law is derived as a second-grade polynomial curve, in the form of:

$$T_1 = f(E_\sigma) = a * E^2 + b * E + c$$

Where:

- T_1 is the hot junction temperature;
- E is the voltage measured by the voltmeter.

Once the a, b and c coefficients are known, is easy to move from the collected voltage data E to the hot junction temperature T_1 . Thus, for the experiments carried out on the prototype, the voltage E has been obtained as the sum discussed before and then processed with the polynomial equation to give the real temperature as an output.

This approach has been used for each thermocouple installed in the test bench (about 25) and for each water flowrate configuration.